APPLICATIONS OF TEXTURED SURFACES FOR LIGHT HARVESTING

by

Byron Cocilovo

———————————————

A Dissertation Submitted to the Faculty of the

COLLEGE OF OPTICAL SCIENCES

In Partial Fulfillment of the Requirements

For the Degree of

DOCTOR OF PHILOSOPHY

WITH A MAJOR IN OPTICAL SCIENCES

In the Graduate College

THE UNIVERSITY OF ARIZONA

2016

THE UNIVERSITY OF ARIZONA

GRADUATE COLLEGE

As members of the Dissertation Committee, we certify that we have read the dissertation prepared by Byron Cocilovo, titled Applications of Textured Surfaces for Light Harvesting and recommend that it be accepted as fulfilling the dissertation requirement for the Degree of Doctor of Philosophy.

_____ Date: April 15th, 2016
Thomas Milster

_____ Date: April 15th, 2016
Khanh Kieu

Final approval and acceptance of this dissertation is contingent upon the candidate's submission of the final copies of the dissertation to the Graduate College.

I hereby certify that I have read this dissertation prepared under my direction and recommend that it be accepted as fulfilling the dissertation requirement.

_____ Date: April 15th, 2016
Dissertation Director: Robert A. Norwood

STATEMENT BY AUTHOR

This dissertation has been submitted in partial fulfillment of the requirements for an advanced degree at the University of Arizona and is deposited in the University Library to be made available to borrowers under rules of the Library.

Brief quotations from this dissertation are allowable without special permission, provided that an accurate acknowledgement of the source is made. Requests for permission for extended quotation from or reproduction of this manuscript in whole or in part may be granted by the head of the major department or the Dean of the Graduate College when in his or her judgment the proposed use of the material is in the interests of scholarship. In all other instances, however, permission must be obtained from the author.

SIGNED: *Byron Cocilovo*

Acknowledgements

This thesis is dedicated to Obi-Wan Kenobi, Leto Atreides II, Tyrion Lannister, my loving wife Rachelle, and Gandalf.

TABLE OF CONTENTS

LIST OF FIGURES

LIST OF TABLES

ABSTRACT

Surface textures add another dimension to optical design. They can be used to redirect light, isolate spectral bands, and enhance optical fields. They effectively take up no space, so can be applied to any optical surface – from intermediary elements to substrates. Here I present three applications of textured surfaces for light harvesting. The first project places scattering textures inside a film that can be applied to windows to scatter infrared light towards solar cells at the edges. The collected energy is then used to power tinting films. The second project uses modular diffractive structures to increase the absorption in solar cells. Lastly, structured silver surfaces are used to enhance plasmonics fields and increase two-photon excitation fluorescence.

INTRODUCTION

Light is one of the most important phenomenon known to humankind. It is the primary way in which we observe our surroundings: from examining the structures of microorganisms, to discovering distant galaxies. Being pure energy, it can travel faster than anything else over endless distances, making it the ideal carrier of both information and energy. All the energy used to build cities, run air conditioners, drive cars, take photos, stream movies, grow forests, and feed all terrestrial life, all originated as light from the sun.

Plants are the primary converters of light into storable chemical energy. Cells in plants convert water and carbon dioxide into sugars. Humans rely on these sugars produced by plants not only to stay alive, but also to power vehicles and generate electricity. Most of the energy used in the world comes from burning energy stored by plants. This includes coal, petroleum, ethanol, and wood. However, photosynthesis is an inefficient process, and converting the resulting chemical energy into kinetic and electrical energy results in the release of large amounts of CO_2, which has led to global warming. A more direct way to produce electricity is with photovoltaics, which directly convert incident photons into free electrons. Despite their limitless reserve of energy (the sun) and low environmental impact, photovoltaics have struggled to replace other energy sources. This is largely because they are more expensive. In order to decrease the cost/watt, a great deal of effort has been devoted to increasing the amount of light collected, and thus energy produced, by the solar cell materials.

The simple idea that it is better to collect more light extends over all fields. In energy production, absorbing more light in the solar panels results in more power output. In data transfer, absorbing more light in the receiver allows for signals to be transferred more densely and over longer distances. In imaging, absorbing more light in the pixel array yields sharper images and higher resolution. And in metrology, absorbing more light in the detector allows smaller details to be distinguished in shorter periods of time. Optical systems

are always designed to utilize as much of the available light as possible and scientists and engineers are always looking for new ways to capture more light.

Texturing optical surfaces allows more light to be collected in a variety of optical systems. Surface textures provide the very basic, and very useful ability to redirect light at an interface. When light is incident on a surface it refracts or reflects in a fixed direction. Texturing allows the light to be redirected or concentrated. The scale and shape of the surface can vary depending on the application. Textures larger than the wavelengths of incident light will scatter light according to ray optics, textures on the scale of a wavelength will diffract light, and metallic textures smaller than a wavelength can confine light. We present three systems where texturing was used as an effective way to enhance the amount of collected light.

The first project is the design of an energy generating window film. Films with imbedded textures on the scale of millimeters were designed to be placed over window panes in order to power electrochromic layers. Embedded textures in the films scatter infrared light to the edges of the window, while remaining transparent to onlookers. Solar cells at the edges of the window collect the scattered light from the sun and use the energy to power the electrochromic layers, thus eliminating the need for external wiring.

The second project uses modular diffraction gratings to increase the angles of light inside solar cell layers. The diffracted light has an increased path length and thus increased absorption in the solar cell. Greater absorption in solar cells leads to greater energy generation or thinner solar cell layers.

The third project uses textured metal films to enhance the light collected from two-photon excitation microscopy. Two-photon excitation microscopy provides imagery of microscopic subjects with excellent contrast, but suffers from poor signal due to it relying on a nonlinear process. Surface texturing increase the signal by enhancing local electric fields with plasmonic modes. These enhanced fields then lead to more generated photons and better image quality.

Chapter 1

Highly Transparent Light-Harvesting Window Film

1.1 Introduction

A tremendous amount of energy is used to cool buildings. A total of 350 billion kilowatt-hours of electricity are used in the U.S. each year for space cooling, which represents 13% of the total residential and 12% of the total commercial electricity usage [1]–[3]. Energy-efficient "smart windows" are an excellent solution to the continual energy consumption from space cooling [4]. Applying voltages to smart films dynamically changes the transparency or shading of the window, which limits the amount of light and heat entering the building. Currently, all of the smart window technologies require an electrical power source to activate the tinting features of the windows. These features require extra electrical wiring and labor for installation, thereby increasing the overall installed-system cost of the smart window.

We propose adding energy-generating films to smart windows that can be retrofitted or applied during fabrication that power the electrochromic materials and quell the need for external wiring and power. The films we have designed send primarily infrared light to solar cells located at the edges of the window while remaining highly transparent when viewed at angles less than 50°. The current cost breakdown of photovoltaics (PVs) shows that nearly half of the system cost is due to balance of system/installation [5], [6]. Installing the energy-generating films jointly with smart windows amortizes the system-installation cost.

Creating self-powering smart windows necessitates that the collection components not interfere with the visual properties of the window. Any noticeable reduction in window quality will render the windows undesirable to the consumer. In addition, smart windows have a maximum transmittance of

only 60% [7]. This forces the transparency of the collection components to be greater than 80% so as to not make the windows too dark in their clear state.

Three groups of light-harvesting window film designs have been previously explored. The first group uses scattering particles or fluorescent dyes (luminescent solar collectors) to randomize the direction of incident light and guide it via total internal reflection (TIR) toward solar cells at the edges of the window [8]–[11]. Scattering and fluorescent solar collectors suffer from haze and coloring created by the absorption or emission bands of the fluorescent dyes. The second group of designs uses semitransparent thin-film solar cell layers that cover the entire window [12]–[20]. This approach suffers from reduced transmittance, requires more manufacturing steps, and has a demonstrated tendency to electrically short. The final design group uses textures near or inside the window to guide light toward arrays of solar cells located throughout the pane or at the edges [21]–[24]. These designs obstruct and distort visibility and can require many solar cells to be placed inside or across the window pane, which can be costly and difficult to fabricate. While the methods just mentioned can be effective for collecting solar energy, they degrade the window clarity or reduce the transparency by too much to effectively be used in conjunction with smart windows.

We set out to design a passive energy-generating window film capable of powering electrochromic and other types of active windows without impairing visible transmittance or quality. The films must easily laminate onto electrochromic window faces during or after fabrication. Embedded textures in the films scatter incident sunlight toward the edges of the window, where the radiant energy is collected and converted to electricity by photovoltaic strips hidden beneath the window frame, as shown in **Fig. 1**. Hiding the solar cells behind the window frame allows the windows to collect light without any loss of viewing area. The films primarily scatter and collect near-infrared light while transmitting visible light, allowing the window to appear transparent
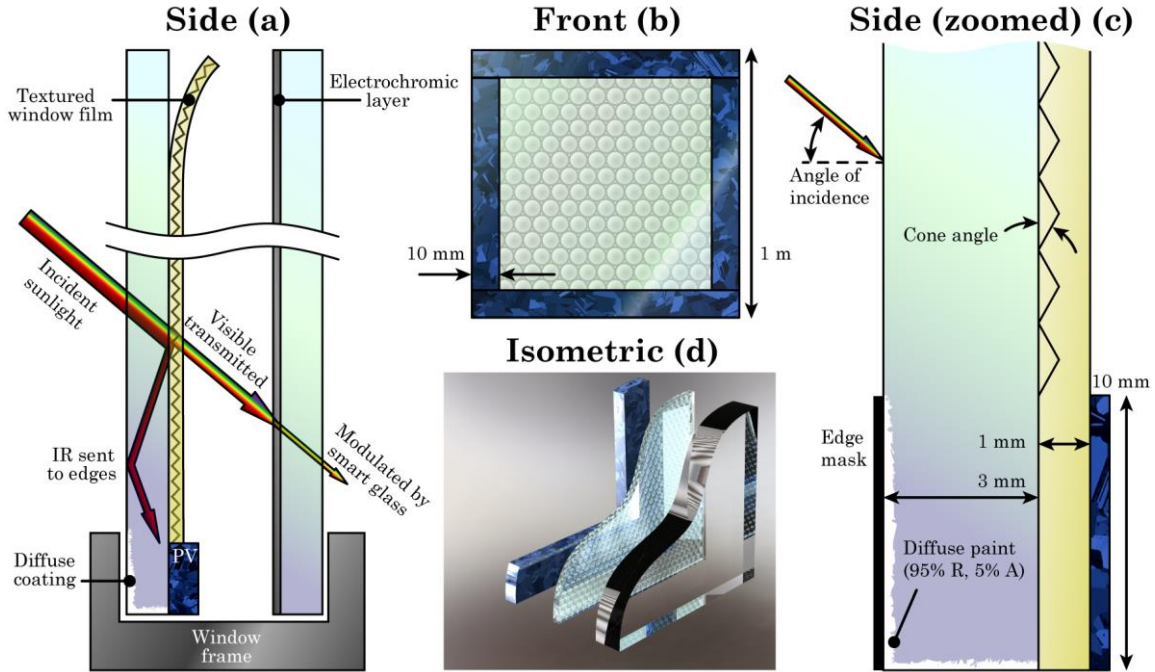
Fig. 1. Window film diagram. (a) Side view of the window film. (b) Front view with model dimensions. (c) Zoomed side view with model dimensions. (d) Isometric view (distributed outer pane only). The film is placed on the inner side of the exterior pane of a double-pane window. Visible light transmits through the film and infrared light scatters toward solar cells located at the edge of the window hidden beneath the window frame. Power from the solar cells can then be used to power electrochromic films on the interior window pane. Not to scale. The textures have been expanded and their reflectance increased to make them visible.

and free of haze. Placement of the film is important. The textured film needs to be placed closer to the exterior than the electrochromic layer; otherwise, infrared light will be absorbed by the electrochromic layer before reaching the solar cells. If double-pane windows are used, the textured film can be placed on the outer pane and the electrochromic layer can be placed on the inner pane. Alternatively, the electrochromic layer can be placed adjacent to the textured layer. This alternative approach can be used if scattered infrared light is not able to pass through the embedded texture. If the light is able to pass through the texture, such as with the air gap design discussed in the next section, the power output will be reduced due to light being absorbed in the electrochromic layer.

1.2 Methodology

The energy-generating window film has two critical features suited for optimization: the texture morphology and coating spectral transmittance/reflectance. Our goal was to maximize the amount of infrared light scattered toward the edges of the windows, while maintaining high visual clarity.

1.2.1 Model

Device modeling and simulation were completed using LightTools, a nonsequential ray-tracing program. **Fig. 1**(b) and (c) show the layout and dimensions of the window model. The basic model that was iterated upon was a 1 m × 1 m × 3 mm glass window coated with a 1 mm index-matched film with an embedded structure. Both the window and film were given the refractive and absorptive properties of Schott N-BK7. Then, 1 cm × 1 m solar cells were added to the edges of the rear surface of the window. Si_3N_4 antireflection coatings were added to the solar cells. A diffuse coating (white paint) with 95% reflectance was added to the edges of the window to redirect rays toward the solar cells. The dependence of transmission and reflection on angle was recorded for all interfaces and coatings used in the model. Only rays entering the solar cells were used when calculating the collected energy. Planar receivers were added where necessary to measure various parameters such as total incident radiation, transmitted visible radiation, and haze.

1.2.2 Light Sources

The illumination conditions have a major effect on the collection efficiency of the window film. In order to generate an accurate assessment of the window film, the geometry, magnitude, and spectrum of insolation must be incorporated. Sunlight was modeled by breaking it up into direct and diffuse components. Direct light refers to rays that come directly from the sun. On clear days, most of the radiation is direct. Direct rays are incident within a 0.27° cone, representing the angular subtense of the sun. Diffuse light
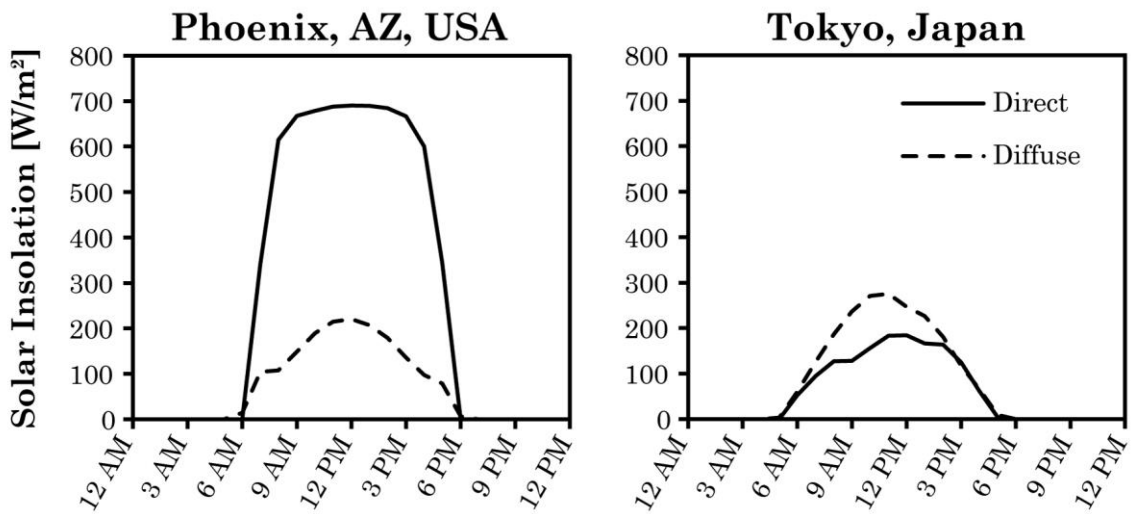
Fig. 2. Solar insolation on September 18th, 2005 in Phoenix (left) and Tokyo (right).

represents rays coming from the sky and clouds. This light has been scattered from particles in the atmosphere and is incident at all angles over a hemisphere. On cloudy days, most of the radiation is diffuse. Diffuse light is modeled as a Lambertian hemispherical source that surrounds the simulation region. Hourly insolation data for the direct and diffuse components was provided by Meteonorm, an extensive weather database with historic weather data from thousands of locations around the world [25]–[27]. **Fig. 2** shows the intensity of direct and diffuse light throughout the day on September 18th, 2005 in Phoenix, USA and Tokyo, Japan. Tokyo has more haze and clouds than Phoenix, so the diffuse component is greater than the direct component. Using the measured insolation data and knowledge of the position of the sun, direct and diffuse sources can be modeled for any day of the year in numerous cities throughout the world.

Our model was examined with four sources: a spectrally flat 1 W/m² collimated source at various angles (spectrally flat), a source representing the direct and diffuse rays at 1 PM in Phoenix, Arizona on September 18th, 2005 (1 PM-Phoenix), an annualized source that sampled rays every hour over a year in Phoenix (annualized), and a 1 kW/m² collimated source at an angle of 60° (1 kW/m², 60°). The spectrally flat source was used to measure the visual

properties of the window film: haze and visible transparency (VT). The spectrally flat source was collimated and extended over the visible part of the spectrum (400–700 nm).

The 1 PM-Phoenix source was used to gauge the performance of the film under realistic lighting conditions. September 18th was chosen because it was a representative day halfway between the summer and winter solstices. The time of 1 PM was chosen to yield the peak daily performance. The solar angle at 1 PM in Phoenix is 58°. Direct and diffuse sources for arbitrary times were created using the LightTools Solar Source Utility. This utility generated the direct source by creating an 18.6 m diameter disk at a distance of 2000 m, resulting in an angular distribution identical to that of the sun. The position of the diffuse source was then adjusted to match the solar conditions at a desired time and date. The diffuse source (sky) was created by surrounding the model with a sphere with Lambertian distribution. The irradiance magnitude of the direct and diffuse sources was adjusted according to Meteonorm data.

The annualized source gives an excellent representation of the total yearly insolation. It was created using the Solar Source Utility, which sampled the angle, position, and magnitude of direct and diffuse rays in Phoenix from every daylight hour over the 2005 calendar year. The rays were then compiled into a single source. This was the primary source used when optimizing the film parameters.

The 1 kW/m², 60° source was included to facilitate comparisons with other works, as 1 kW/m² is the standard solar flux used in the northern hemisphere. The 60° incident angle was chosen to roughly match the 1 PM-Phoenix source angle.

The 1 kW/m², 60° source uses the air mass 1.5 (AM1.5) spectral distribution. The 1 PM-Phoenix and annualized sources utilized versions of the AM1.5 spectrum that were scaled to match their respective direct and diffuse

solar fluxes. The AM1.5 spectrum was developed to represent a typical spectrum from the sun in the continental U.S.
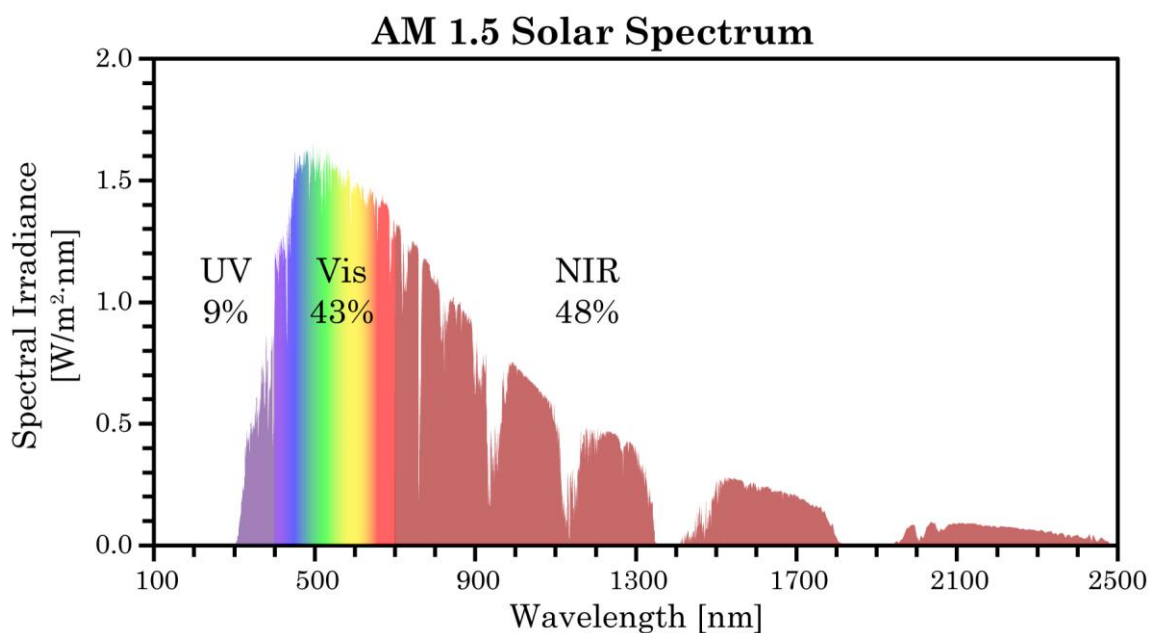
Fig. 3. AM 1.5 Solar Spectrum showing the fraction of sunlight in the UV, visible, and IR.

Specifically, the AM1.5 spectrum represents the spectral irradiance from the sun with a 48.2° angle from zenith. The integrated spectrum has an irradiance of 1 kW/m². As shown in **Fig. 3**, 9% of the solar irradiance is in the ultraviolet, 43% is in the visible, and 48% is in the near-infrared (NIR). The spectral band from 700–1050 nm, where light can be harvested by silicon cells but is invisible to the human eye, contains 30% of the total solar energy and 33% of the photons. In terms of both energy and photon flux, there is a substantial amount of energy to collect without reducing the visibility of the window.

South-facing windows were used for the majority of our simulations. In the northern hemisphere, the greatest amount of light enters buildings from the south, making them the most suitable for both smart glass and energy-generating window films. South-facing windows also receive sunlight at large angles, which is more easily directed toward the edges. East- and west-facing windows are only illuminated for half of the day, and at smaller angles of

incidence on average. North-facing windows are almost never under direct solar illumination in the northern hemisphere.

1.2.3 Design Metrics

There are four main design metrics we used for the energy-generating window film: haze, VT, edge collection efficiency (ECE), and electrical power output (EPO). Targets for haze, VT, and EPO were provided by SAGE Electrochromics, a major developer of electrochromic windows. To ensure that the films do not significantly impact window quality, the internal VT needs to be greater than 80%, haze needs to be less than 1% up to a 60° angle of incidence (AOI), and the films need to generate at least 0.4 W/m² to power the electrochromic windows in their darkened state [7], [28].

Haze is meant to represent how foggy the window appears to observers. We define haze as the ratio of diffuse transmitted light to total transmitted light, which can be written as

$$\text{haze} = \frac{T_{\text{scattered}}(400 - 700 \text{ nm})}{T_{\text{total}}(400 - 700 \text{ nm})}, \quad\quad (1)$$

where $T_{\text{scattered}}$ is the scattered transmitted visible light and T_{total} is the scattered and specular transmitted visible light. Haze should be as low as possible to ensure clarity. The spectrally flat source was used when calculating haze and VT.

VT is the fraction of incident visible light that passes through the glass without scattering, and can be written as

$$\text{VT} = \frac{T_{\text{scattered}}(400 - 700 \text{ nm})}{I_{specular}(400 - 700 \text{ nm})}, \qu\quad (2)$$

where I_{specular} is the incident irradiance on the window and T_{specular} is the irradiance transmitted through the window within ±0.5° of the incident angle. The spectral band from 400–700 nm encompasses the photopic response of the human. eye, which is approximately normally distributed with a peak near 550 nm [29]. VT of the films should be as high as possible to ensure that the system transmittance does not drop too low, as electrochromic windows have

maximum transmittances of only 55%–65% [7]. In order for the energy-generating films to be used in conjunction with smart glass, the internal VT of the films must be greater than 80%. The internal VT is calculated by dividing the total VT of the film by the total VT of planar glass. This eliminates Fresnel reflections at the glass–air interfaces that are present in all windows.

Edge collection efficiency is the third metric used and is a measure of the fraction of the full solar spectrum incident on the window that reaches the edges. ECE is written as

$$\text{ECE} = \frac{I_{\text{collected}}(280 - 2500 \text{ nm})}{I_{\text{total}}(280 - 2500 \text{ nm})}, \tag{3}$$

where I_{total} is the direct and diffuse solar irradiance incident on the window, and $I_{\text{collected}}$ is the irradiance reaching the edges of the window. ECE is intended to give us an idea of how well the structures scatter light irrespective of the solar cell absorption band. The spectral band from 280–2500 nm was used to fully encompass the solar spectrum. Both ECE and EPO were calculated separately for the 1 PM-Phoenix source; the 1 kW/m², 60° source; and the annualized source.

The last metric is electrical power output, which tells us how much power is produced by the window film at a given time. It is calculated by integrating the solar cell responsivity over the spectrum incident on the cells and can be written as

$$\text{EPO} = V_{\text{OC}} \cdot \text{FF} \cdot \frac{e}{hc} \cdot \int S(\lambda) \cdot \text{IQE}(\lambda) \cdot \lambda \cdot d\lambda, \tag{4}$$

where V_{OC} is the open circuit voltage of the cell, FF is the fill factor, e is the elementary charge, h is Planck's constant, c is the speed of light, λ is the wavelength, $S(\lambda)$ is the spectral power distribution of the light entering the solar cells, and $\text{IQE}(\lambda)$ is the internal quantum efficiency of silicon. The internal quantum efficiency of silicon was taken from [30], and extends from 350 to 1050 nm. We assumed that the solar cells were made from silicon with an open circuit voltage of 0.7 V, a fill factor of 0.75, and an absorptance of 100%.

These conditions yield a power-conversion efficiency of 19%–20% depending on the spectrum reaching the cells. Silicon cells do not collect light past 1050 nm, which leaves a large portion of the solar spectrum unutilized. Other solar cell materials with smaller bandgaps such as InGaAs or Ge may be used to better utilize NIR radiation, but would be much more expensive. This work is primarily focused on scattering NIR light toward the edges of the window, regardless of the collection medium. As we will later discuss, the texture coating may be used to tune the spectral reflectance band of the scattering layer to optimize the solar cell EPO.

Haze and VT are in competition with EPO. Greater EPO requires lower VT and increased haze. The most difficult of these parameters to optimize is EPO. The reason for this is that sunlight enters the film from a wide range of incident angles throughout the day. The angles of the rays inside the window are further randomized after reflecting off of the textures. As a result, most of the light reflects back out of the window before reaching the edges. This makes it challenging to design a structure that collects a significant portion of sunlight. A structure that works well at 9 AM may be ineffective at 11 AM.

ECE and EPO were optimized by varying the structure forms (cones, hemispheres, pyramids, etc.), pitch, and coating spectral reflectance. We discovered quickly that the best texture shape was conical. Cones enable us to vary the reflected ray direction by changing their base angle, and their rotational symmetry provides consistent performance as the solar angle fluctuates. Conical holes are also compatible with a variety of large-scale casting or embossing techniques. The cones were arranged on a hexagonal grid to maximize the amount of textured surface area. Haze and VT were adjusted by altering the spectral properties of the texture coatings.

Haze is caused by two main factors. The first is an index difference between the top and bottom plastic layers. If the top and bottom layers are not index-matched, the cones act like lenses and scatter light. While this effect does not

(a) $n_1 = n_2$ **(b)** $n_1 > n_2$ **(c) Simulation geometry**

(d) $\Delta n = 0.0001$ **(e)** $\Delta n = 0.001$ **(f)** $\Delta n = 0.01$
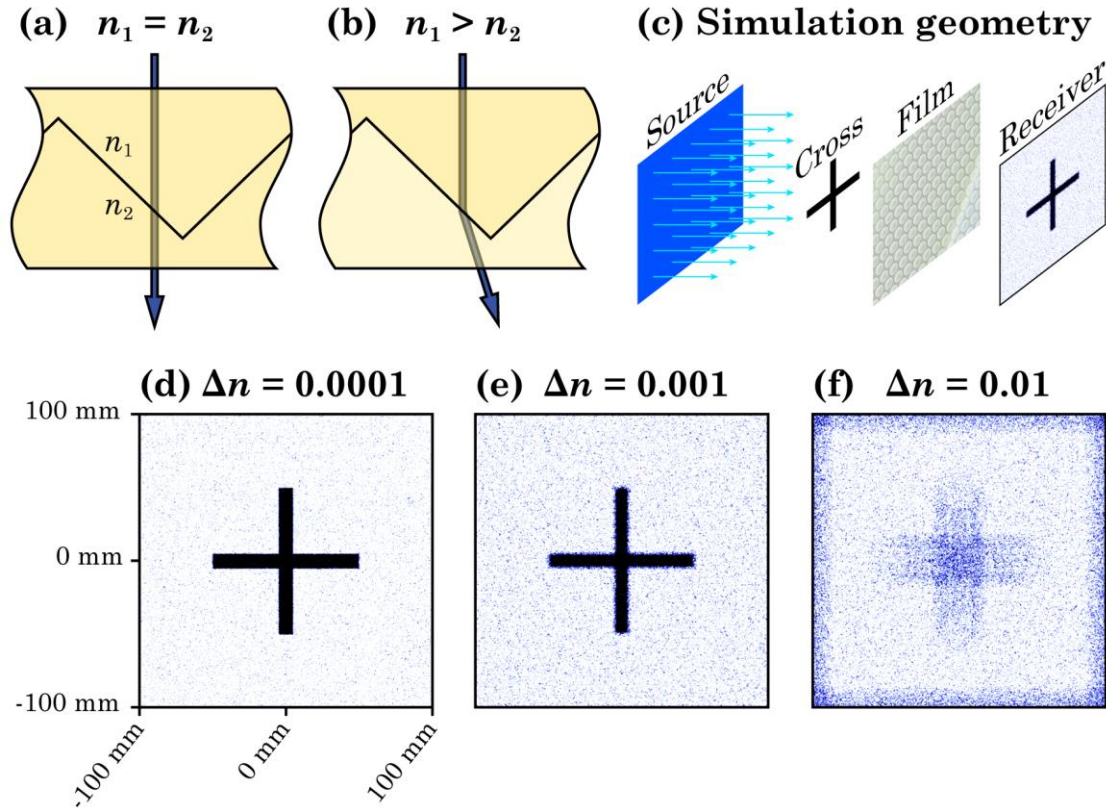
Fig. 4.   Ray deviation from refraction (a) without and (b) with an index difference between top and bottom film layers. (c) Simulation geometry used to generate the plots. The irradiance on the receiver plane is shown for index differences of (d) 0.0001, (e) 0.001, and (f) 0.01.

influence simulations, it will be present when the films are fabricated and should not be neglected. **Fig. 4** shows how index variations between the layers affect haze. The plots were generated in LightTools by directing collimated light toward a 50 mm cross followed by a textured film with 35° cones. The plastic layer on one side of the texture was given an index of 1.5, and the plastic layer on the other side was given an index of $1.5 + \Delta n$. The receiver plane was placed two meters away from the 200 mm × 200 mm window, representing a common observer distance. As the index difference between the film layers increases, so does the haze. This is indicated by the increasing blur near the edges of the shadow of the cross. The refractive index difference between the layers must be less than 0.001 to mitigate haze.

The second factor affecting haze is the thickness of the texture coating. To reduce haze, the coating needs to be as thin as possible, ideally subwavelength.

If the scattering layer is optically thick (> 1 µm), light rays displace as they pass through the texture layer, causing them to see a different surface slope as they enter the second plastic layer and resulting in a net angular deviation. Ray deviation is only present for rays striking the window at non-normal incidence. To visualize this effect, rays were sent at a 60° angle through a window with a textured film. **Fig. 5** illustrates ray deviation and shows the angular distribution of rays passing through a thick (10 µm) air gap and a thin (10 nm) Ag coating. Rays passing through the air gap are significantly deviated whereas rays passing through the optically thin Ag film are not.

1.2.4 Texture Coatings

Three texture coatings were considered: a 10 µm air gap, a 10 nm Ag layer, and a five-layer SiO_2–Ag stack consisting of 150 nm SiO_2, 4 nm Ag, 130 nm SiO_2, 4 nm Ag, and 150 nm SiO_2. The air gap layers utilize TIR at the film–air interface to reflect the light toward the edges of the window. Rays incident on the window at small angles transmit through the film, and rays incident at large angles undergo TIR and propagate toward the edges. Manufacturing textured films with air gaps is impractical. However, the air gap can be replaced with other low-index materials such as aerogel, which have similar optical properties and can be deposited in thin layers [31], [32].

The 10 nm Ag layer and SiO_2–Ag stack utilize optical thin films rather than TIR to reflect light. This makes their reflectance much less sensitive to incident angle. Ray deviation is also avoided with these coatings because they are subwavelength. The thin films described here were designed to act like low-pass filters that transmit visible light and reflect infrared light. The 10 nm Ag layer was considered because of its simplicity and decent performance. Silver acts as a natural bandpass filter and is transparent if made thin enough. However, it suffers from reduced transmission and coloring: windows appear blue in transmission and red in reflection.
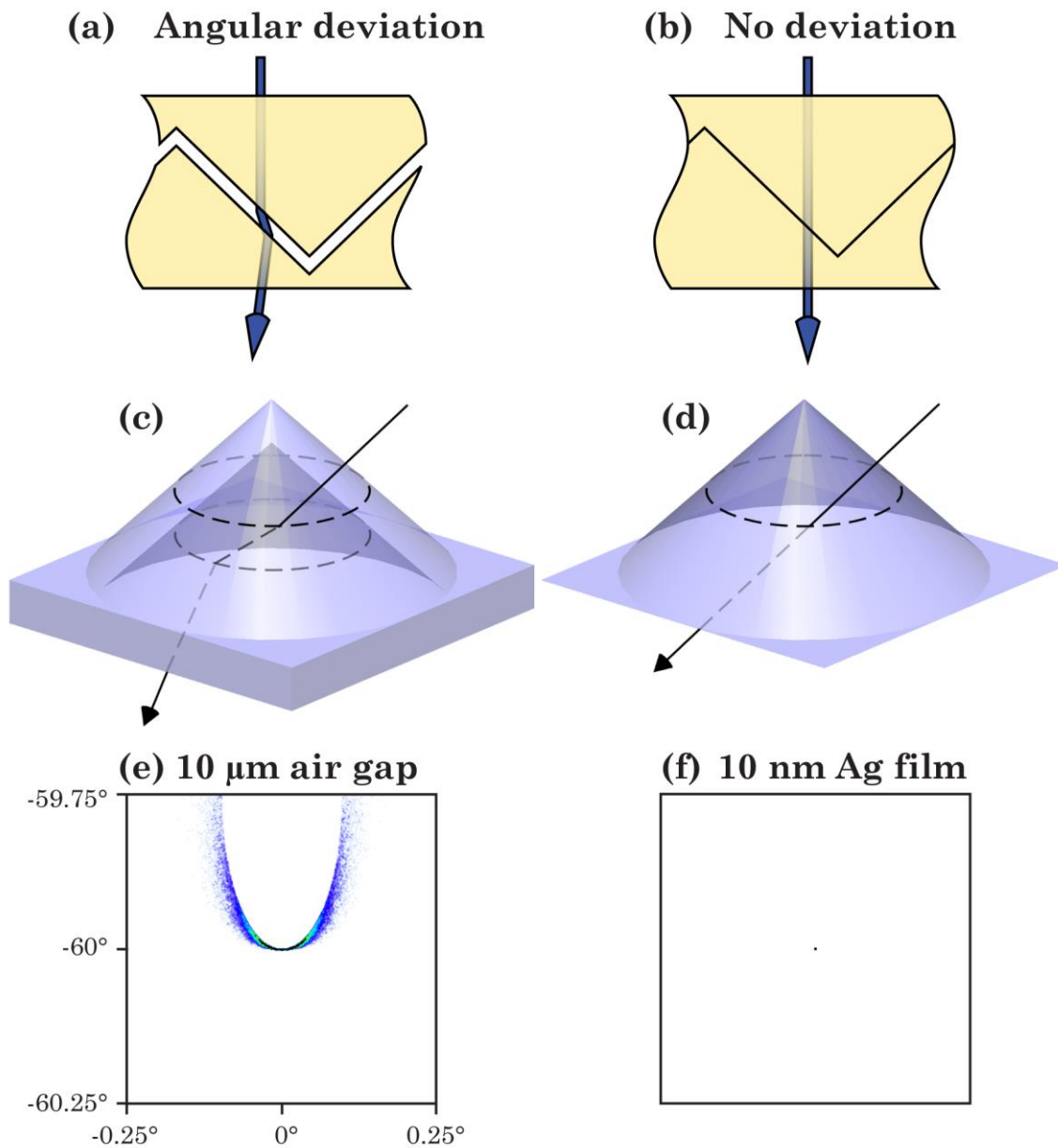
Fig. 5. Ray deviation from film thickness for (a) thick and (b) thin scattering textures (the rays are angled out of the page). A ray trace of a thick air gap cone and a thin film are shown in (c) and (d), respectively. The cone parameters were adjusted in LightTools to make the deviation more pronounced. The blue cones are air and the surrounding medium has an index of 1.5. The dashed rings show where the rays intersect the outer and inner cone interfaces. The thick air gap leaves a residual deviation in the ray, while the thin film transmits the ray without deviation. The angular distribution of the transmitted rays is shown for a textured film with a 10 μm air gap with (e) 10° cones and (f) 10 nm Ag film with 10° cones. Light was incident at a vertical angle of –60°, so the plots are centered on (0°, –60°). There was no angular deviation from the 10 nm Ag thin film, so all the light is represented by the dot in the center of (d).
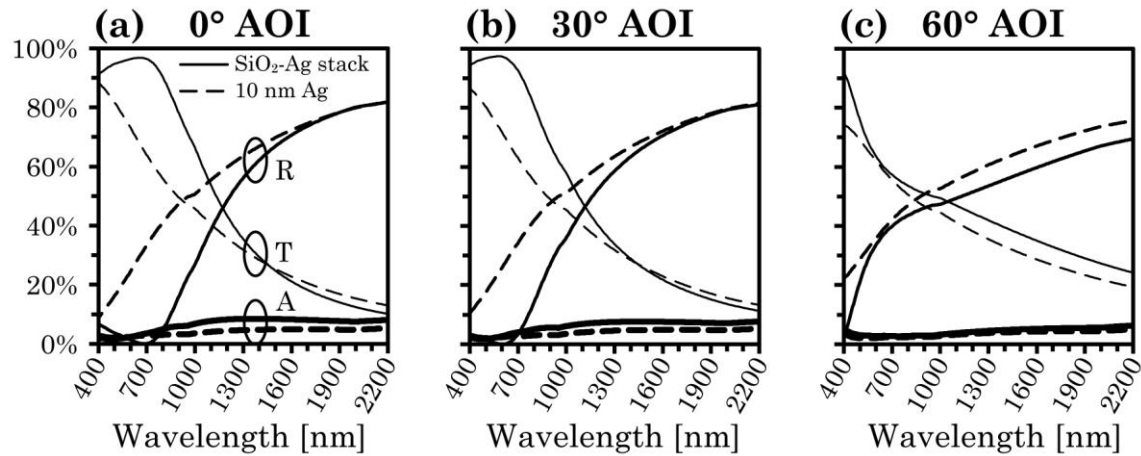
Fig. 6. *R*, *T*, and *A* of the thin films at (a) 0°, (b) 30°, and (c) 60° AOI. The 10 μm air gap is not shown, but has a constant Fresnel reflectance of approximately 8% at 0° and 30° AOI, and 18% at 60° AOI.

The five-layer SiO_2–Ag stack modifies the reflectance and transmittance of silver by dividing it between silica layers. It requires more deposition steps, but has greater visible transmittance and is spectrally flat in the visible. The 150 nm outer layers of SiO_2 also protect the silver from oxidizing or being damaged during fabrication. **Fig. 6** shows the reflectance, transmittance, and absorptance of the two thin films at 0°, 30°, and 60° angles of incidence. The SiO_2–Ag stack has significantly higher transmittance in the visible and is spectrally flat. The reflectance in the infrared is also high, which will help houses and buildings stay cool during summer and warm them during winter. Visible transparency and haze worsen for both films at larger angles of incidence, but this is acceptable because, when peering through windows, people tend to focus on the objects ahead of them rather than on the sides.

1.3 Results

A sweep of the cone angles was performed for each of the three texture coatings (10 μm air gap, 10 nm Ag, SiO_2–Ag stack). The corresponding ECE at each angle was calculated using the annualized source. **Fig. 7** shows the results of the cone angle optimization. The size of the cones was found to have minimal impact on light collection. For simplicity and to minimize simulation time, the
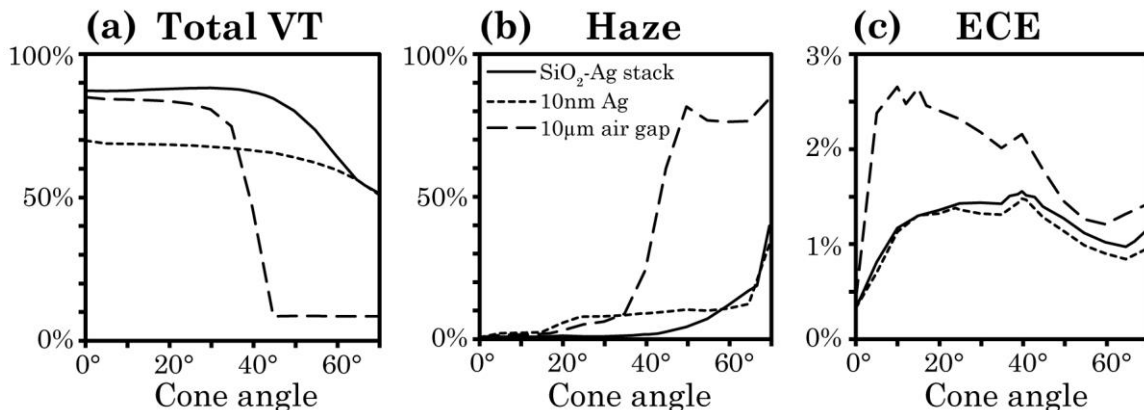
Fig. 7. Film performance vs cone angle. (a) Total VT, (b) haze, and (c) ECE for the SiO$_2$–Ag stack, 10 nm Ag, and 10 μm air gap coatings.

diameters were set to 1 mm. However, the final window film should use smaller cones to make the textures appear uniform rather than like discrete circles. The cone angles have a significant impact on light collection, and the optimum angles vary with coating type.

The maximum average annual ECE for each of the three coatings coincides fortuitously with cone angles that produce excellent VT and haze. The cone angles that produced the greatest ECE were 10° for the air gap, 40° for the 10 nm Ag layer, and 40° for the SiO$_2$–Ag stack. Although 40° cones begat the greatest ECE for the SiO$_2$–Ag stack, they also produce a haze that is slightly above the target of 1%. Instead, cone angles of 35° were used for further calculations as they yield a haze that is only 0.5% while maintaining a high ECE and EPO. VT remains constant for cone angles less than 35° for all three coatings. Past 40° haze and VT of the air gap coating rapidly worsen due to TIR at the texture surfaces. Cone angles greater than 50° cause the NIR reflectance band edge of the SiO$_2$–Ag stack and 10 nm Ag film to blueshift into the visible, degrading VT and haze. The 10 nm Ag coating is least sensitive to cone angle.

The visual qualities of the coatings were analyzed using their respective optimum cone angles: 35°, 40°, and 10° for the SiO$_2$–Ag stack, 10 nm Ag film, and 10 μm air gap, respectively. The VT and haze of the three films on glass
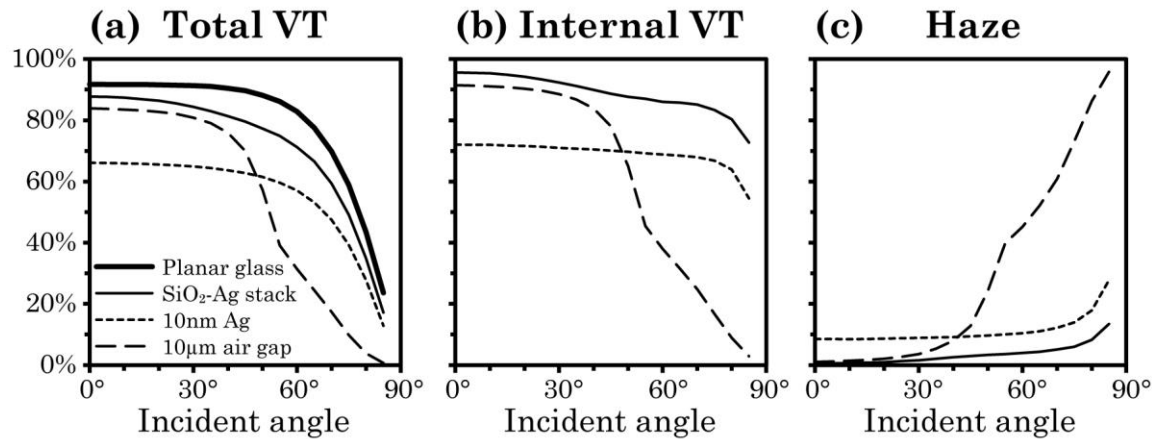
Fig. 8. Film performance vs AOI. (a) Total VT, (b) internal VT, and (c) haze for the SiO2–Ag stack with 35° cones, 10 nm Ag film with 40° cones, and 10 μm air gap with 10° cones.

windows were measured versus incident angle, as shown in **Fig. 8**. The VT and haze of the SiO$_2$–Ag stack and 10 nm Ag film are nearly invariant with angle. The haze of the SiO$_2$–Ag stack is less than 1% for viewing angles up to 20°, and increases to 3.9% at 60°. The haze of the 10 nm Ag film is approximately 10% at viewing angles greater than 20°, which would give an appearance similar to a dusty window. The air gap has high VT and low haze at viewing angles less than 45°, but unacceptably low VT and high haze at viewing angles greater than 45°.

Fig. 9 shows the spectra of collected light for each of the three films when illuminated with the 1 PM-Phoenix source. The AM1.5 spectrum is also included for comparison. The spectra generally follow the AM1.5 spectrum, indicating that all three films act like broadband reflectors at large angles of incidence. A redshift is present in the spectrum of the SiO$_2$–Ag stack and, to a lesser degree, the 10 nm Ag film. The 10 μm air gap does not exhibit color shifting. These results are consistent with the spectral reflectance curves presented in **Fig. 6**. These results also emphasize that the spectrally selective properties of the thin films are primarily important for maintaining high VT and low haze for observers looking through the windows at shallower angles of incidence.
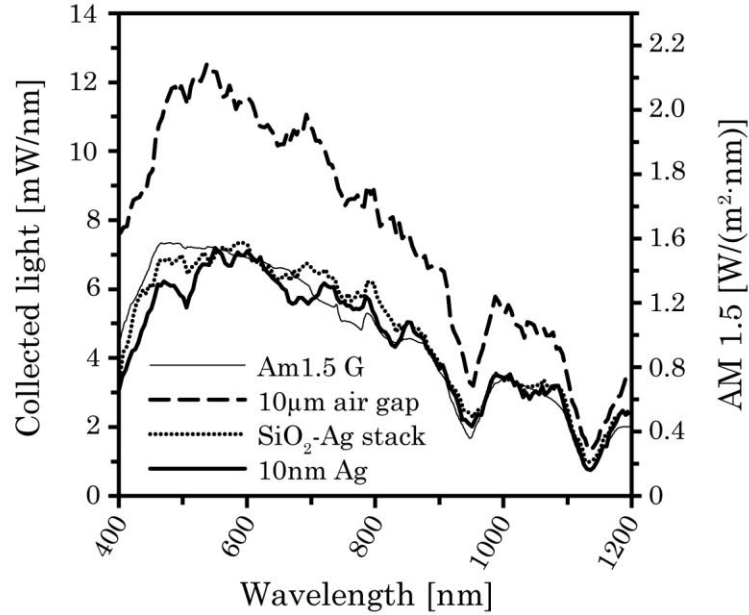
Fig. 9. Spectra collected by the window films when illuminated with the 1 PM-Phoenix source.

Table 1 summarizes the visual performance of the films as well as the ECE and EPO when illuminated with the 1 kW/m², 60° source; 1 PM-Phoenix source; and annualized source. Values in bold indicate that they have exceeded the target. All three films are able to produce enough energy to power smart windows (at least 0.4 W/m²). When illuminated with the 1 PM-Phoenix source, the air gap produced the greatest output power (1.41 W), followed by the SiO_2–Ag stack (0.89 W) and the 10 nm Ag layer (0.84 W).

Table 1. Energy Generating Window Film Results

	Source	SiO_2–Ag Stack 35° Cones	10 nm Ag 40° Cones	10 µm Air Gap 10° Cones	Target
Haze (0° AOI)	Spectrally flat	**0.6%**	8.5%	1.1%	<1%
Haze (60° AOI)		3.9%	10.4%	45.2%	<1%
Internal VT (0° AOI)		**95.6%**	72.0%	**91.5%**	>80%
Internal VT (60° AOI)		**86.0%**	68.9%	37.9%	>80%
ECE	1 kW/m², 60°	**1.44%**	**1.35%**	**3.68%**	
EPO [W]		**1.05**	**1.00**	**1.75**	>0.4
ECE	1 PM-Phoenix	**1.41%**	**1.34%**	**3.29%**	
EPO [W]		**0.89**	**0.84**	**1.41**	>0.4
ECE	Annualized	**1.42%**	**1.47%**	**2.65%**	
EPO [W]		**0.49**	**0.52**	**0.67**	>0.4

20
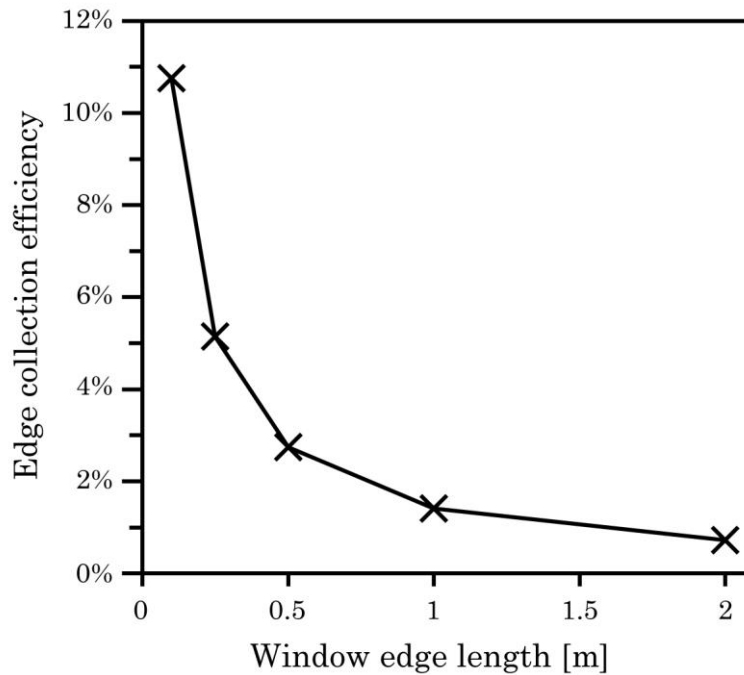
Fig. 10. ECE versus the edge length of a square window for a SiO_2–Ag stack window with the 1 PM-Phoenix source.

The window film is only able to capture a fraction of the incident radiation. In part, this is because much of the design was dedicated to making the window visibly transparent. Nevertheless, using completely reflective 35° cones with the 1 PM-Phoenix source only increases the ECE from 1.4% to 1.9%. The main factor contributing to the minimal ECE is leakage through the front and back surfaces of the window. Each reflection the light rays undergo increases the likelihood that they will scatter out through the surface. Most of the light that is collected is incident on regions of the window near the outer edges. Using smaller windows decreases the EPO, but increases the ECE and makes energy-generating window films a more viable solution for powering electrochromic windows or other electronic devices with transparent screens. **Fig. 10** shows how the ECE is greater with smaller windows.

Absorption in the window glass and film also limits the amount of light harvested. The previous results were gathered using Schott N-BK7 as the window and film material. Schott N-BK7 has very little absorption in the

Table 2. Power Output for Various Glasses

Window Material	EPO [W]
Ideal glass (no absorption)	0.90
Schott N-BK7 (used for simulations)	0.89
Schott B270	0.87
Low-iron glass	0.67
Soda lime glass	0.38

visible and near infrared, but is also costly. The effects of absorption were explored with a variety of affordable glasses that are frequently used in windows: soda lime glass, low-iron glass, Schott B270, Schott N-BK7, and an ideal glass with no absorption. Soda lime glass is the cheapest glass used in windows, but suffers from elevated absorption and "greening" caused by its high iron content. Low-iron glass significantly decreases the glass absorptance by reducing the iron content. The optical constants of soda lime glass and low-iron glass were taken from [33]. Schott B270 and Schott N-BK7 both have negligible absorption. The optical constants for Schott N-BK7 were taken from [34]. The transmittance of Schott B270 was taken from [35] for wavelengths spanning 300–2000 nm, and measured using a Cary 5000 UV–Vis–NIR spectrophotometer from 2000 to 2500 nm. Lastly, a fictitious glass free of absorption was used as an ideal reference, where light is only lost by scattering.

   Table 2 shows the power output of the window film of various materials, and **Fig. 11** shows the glass absorption coefficients. For each simulation, both the window and film were modeled with the same refractive and absorptive properties. All the absorption simulations used embedded structures with 35° cones coated with the SiO_2–Ag stack and 1 PM-Phoenix illumination. Schott N-BK7 and B270 do not absorb a significant amount of light, with EPOs of 0.89 W and 0.87 W, corresponding to decreases relative to the absorption-free glass of only 2% and 3%, respectively. Low-iron windows are more absorbing but provide sufficient power (0.67 W) for electrochromic films, which only require 0.4 W. Soda lime glass absorbs a significant amount of light and reduces the
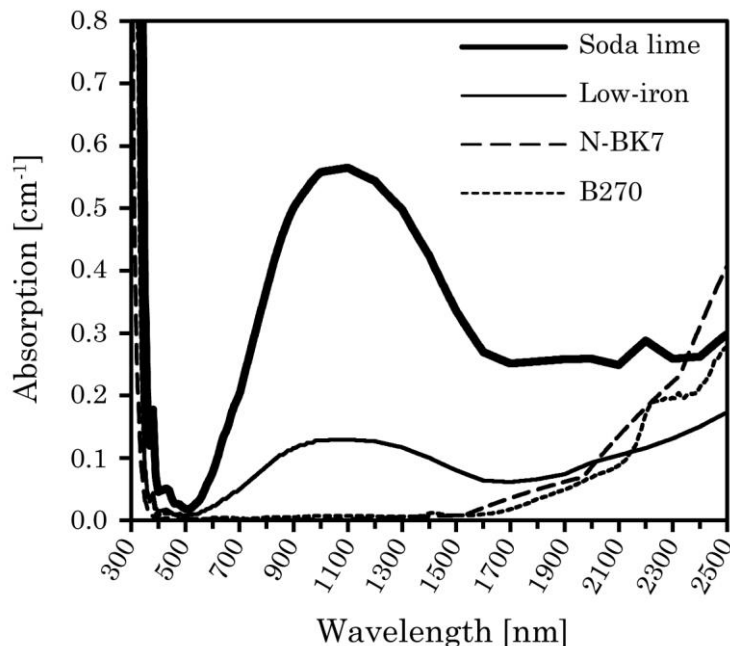
Fig. 11. Absorption coefficients for various glasses.

EPO to 0.38 W. On sunny days, windows made from soda lime glass would be able to generate just enough energy to power the electrochromic films though, during less ideal solar conditions, the window film will be unable to power the electrochromic layer. While soda lime glass may provide adequate transparency on sunny days, the ideal configuration would have windows made from low-iron glass or B270.

1.4 Manufacturing Methods

The window films presented here are compatible with existing large-scale manufacturing techniques. A potential fabrication process would first consist of UV-microimprinting the desired textures into an UV-curable polymer [36]. The aspect ratios of the cylinders presented here range between 0.01 and 0.42. These are well within the limits of most casting and embossing processes, which are capable of patterning structures with aspect ratios as high as 2 and dimensions less than microns [37]–[39]. After casting or embossing, the textures would be coated with the desired reflective layers via sputtering [40], [41]. The thin-film designs are simple and the exact positions of their

corresponding band edges are not critical, so thickness variations during deposition within 5% will not significantly alter the system performance.

Lastly, the UV-curable polymer would be poured over the bottom textures and cured. In this way, the bottom textured layer works like a mold for the top layer, ensuring that ray deviation due to texture mismatch is prevented. It is essential that the top and bottom texture layers be made from the same material to prevent ray deviation from index mismatch (**Fig. 4**). Matching the top and bottom texture layers ensures that the structures will be fairly insensitive to deformations or blemishes obtained during the initial patterning step. The random nature of the scattering process that directs light to the edges of the window allows for a large variance in the structure geometry without significantly compromising the window clarity or collection efficiency.

1.5 Conclusions

We have successfully designed and modeled transparent textured films capable of powering smart windows. When sunlight is incident on a coated window, the films can automatically start generating power to tint the windows without any user input. This may be particularly useful for cooling houses or offices that are unoccupied during parts of the day. In addition to powering smart windows, the films also reflect infrared light. This makes them suitable for passively keeping buildings cool in the summer by reflecting much of the NIR radiation and warm in the winter by trapping the thermal infrared inside.

Of the three coatings considered, the SiO_2–Ag stack showed the greatest potential for commercial use due to its high VT and negligible haze at normal incidence. The SiO_2–Ag stack exceeds the performance targets for VT and EPO at all viewing angles. Haze at viewing angles less than 20° is below the target of 1%, and remains low at viewing angles greater than 20°. The SiO_2–Ag stack is able to provide moderate collection efficiency while maintaining high VT and

low haze because of the high coating transmittance in the visible and high reflectance in the infrared.

The 10 µm air gap collects the most light, but appears frosted at viewing angles greater than 45°, making it unsuitable for use with conventional windows. However, textured low-index gaps may be useful for creating transparent-diffusing windows. Standard windows provide excellent visibility but do not diffuse direct sunlight, while window blinds and shades diffuse incident sunlight but are opaque. Textured low-index layers can combine the best aspects of windows and blinds by diffusing incident sunlight, which is always incident at large angles on south-facing windows, and maintaining visual clarity within a 45° cone.

There are many other film parameters that can be enhanced in future studies: nonabsorbing dielectrics can be used instead of silver, the number of layers can be increased to tune and sharpen the transmission band, hexagonal cone bases can be used instead of circular ones to completely cover the film, and the structures can be individually varied based on their position in the window. Smaller windows also yield higher efficiencies, which may be useful for tablets or e-readers that are used outside. Regardless of the device that these films are applied to, they present a viable methodology for energy conservation and collection via surface texturing.

Chapter 2

MODULAR DIFFRACTION GRATINGS FOR SOLAR CELL ABSORPTION ENHANCEMENT

2.1 Introduction

All solar cells can benefit from enhanced light collection, as greater light collection can increase the electrical output or reduce the required cell thickness. In particular, bulk heterojunction (BHJ) organic solar cells (OSCs) are promising photovoltaic candidates that can benefit from increased light collection. They are flexible, lightweight, low cost, and can be produced in large volumes using simple processing techniques [42]. However, the efficiency of OSCs needs to be enhanced for them to become a competitive energy source for most applications [42]–[44]. Efficiencies between 1% and 10% have been demonstrated for various OSC designs, but improvement is still needed [45]–[51].

Radiant energy passes through several stages in a solar cell before it is converted to electrical energy. First, a fraction of the incident light, η_A (absorption efficiency), is absorbed in the active layer and creates excitons. Some excitons recombine and are wasted, but a fraction, η_D (dissociation efficiency), dissociate into electrons and holes (often at a material interface) that can then travel towards their respective electrodes. A fraction of these electrons and holes, η_C (collection efficiency), are then collected by the corresponding cathode or anode. The product of these efficiencies is the power conversion efficiency (hereby referred to as *efficiency*), which describes the fraction of radiant energy that is converted into electrical energy as indicated in **(5)**

$$\text{Efficiency} = \eta = \eta_A \cdot \eta_D \cdot \eta_C \tag{ 5 }$$

The charge dissociation efficiency, η_D, is related to the exciton diffusion length and the average distance to donor-acceptor interfaces. The Frenkel excitons in organic solar cells have diffusion lengths of only $5 - 10$ nm, making it difficult for them to reach a boundary before recombination occurs [48]. This has driven makers of organic solar cells to use BHJs with nanoscale morphology instead of conventional planar heterojunctions.

The absorption efficiency, η_A, and charge collection efficiency, η_C, can be manipulated by adjusting the active layer thickness. η_A is enhanced with thicker layers, and η_C is enhanced with thinner layers, leading to an optimal layer thickness that produces the greatest efficiency. This optimal thickness is from 100 nm to 250 nm for conventional cells using a blend of poly(3-hexyl)thiophene and [6,6]-phenyl-C61-butyric acid methyl ester (P3HT:PCBM) [52].

To simultaneously increase η_A and η_C it has been proposed to add diffraction gratings to solar cell substrates [53]–[57]. Diffraction gratings enhance the path length of light in the cell thereby increasing η_A and the efficiency. Alternatively, η_A can be maintained and the active layer can be made thinner to increase η_C and the efficiency.

Textured surfaces have been applied to silicon solar cells to a great degree, and to OSCs to a lesser degree. The driving factor behind texturing inorganic cells is to lower the cost of the device by reducing the amount of silicon needed to absorb an equivalent amount of light as planar cells. OSCs, on the other hand, have found minimal use for gratings because of their low cost and high absorptance. Over 90% of green light is absorbed in 100 nm of OSC active layers, compared to only 18% in crystalline silicon [58]–[60]. The primary benefit of using diffraction gratings on OSCs comes from the increase of charge collection efficiency achieved through reduction of the required active layer thickness.

Another factor restricting the use of textured surfaces on OSCs is their thinness. The well-known $4n^2$ optical enhancement limit, discussed below,

assumes the active layer is much thicker than a wavelength so many photon modes may be confined. This holds true for silicon solar cells, where the wafers are tens to hundreds of microns thick. In contrast, OSCs have active layer thicknesses of only one or two hundred nanometers – significantly less than the wavelengths of interest. Thin layers such as these are unable to confine light, making it difficult to approach the $4n^2$ limit. Instead, the light must be confined in the glass or plastic substrate and absorbed only when it extends into the active layers. An upside to the breakdown of the $4n^2$ limit when thin layers are used is that the limit may be surpassed when gratings are used under the right conditions [61].

Previous studies on the effects of applying gratings to OSCs have used textured active materials and electrodes, making it difficult to discern what factors contribute to changes in absorptance or efficiency. The intended purpose of diffraction gratings is to enhance the path length of light in the active layer, but many other variables are also changed when active layers are patterned that may have advantageous or adverse effects. Charges in textured active layers have varying distances to travel depending on their proximity to a peak or trough, possibly leading to a change in η_C. The surface area of textured electrodes is also increased, causing an increase in electrode resistance and a reduction in the efficiency. Textured electrodes and active layers can also suffer from resonance anomalies, where light is coupled into surface plasmons at structured dielectric-metallic interfaces [62]. Texturing also adds complexity to the fabrication process that can lead to shorting and nonuniform film layers. OSCs are a developing technology, and more research is needed to fully understand their operation. In short, patterning the OSC active layers can introduce a number of correlated effects, making it difficult to clearly identify their impacts on the absorptance and efficiency.
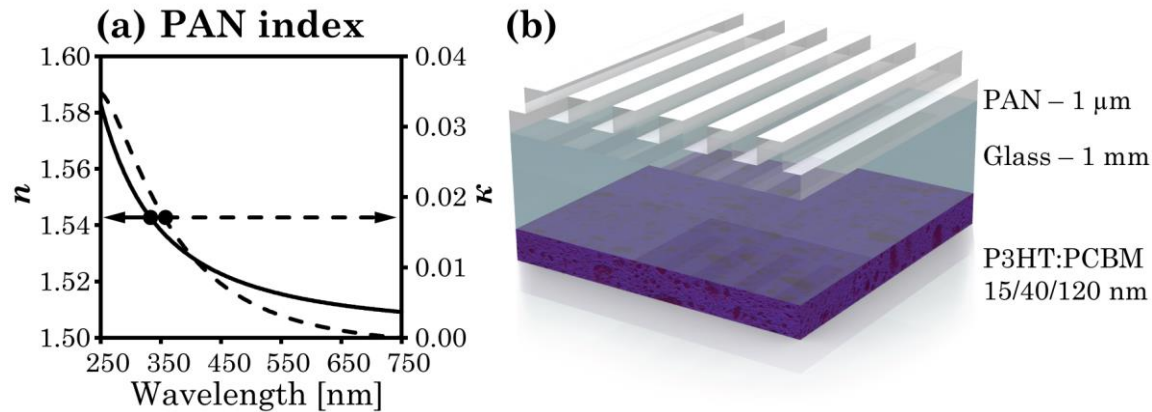
Fig. 12. PAN index and structure model. (a) Refractive index of PAN measured using an ellipsometer. (b) Diagram of the structure used to measure absorption enhancement. The top of the glass substrate is coated with a PAN grating, and the bottom is coated with P3HT:PCBM.

2.2 Description of work

We have applied diffraction gratings to solar cells to study their effects on the optical and electrical properties of the cells. The grating and OSC layers are patterned on opposite sides of the glass substrate. In this configuration we can do a rigorous analysis of diffraction enhancement while ignoring surface texturing effects, interfacial interactions, and resonance anomalies.

Isolation of the gratings from the active layers also enables them to be completely modular. The patterning and analysis of the gratings are independent of the methods and materials used to create the solar cells. Both the physical gratings and their theoretical descriptions outlined here are not limited to OSCs, or even solar cells in general, but may be applied to any device that would benefit from the use of scattered light.

To observe and understand the absorption enhancement in OSC active layers, we prepared textured and planar samples with various P3HT:PCBM thicknesses; numerous gratings were also examined. The gratings were made from polyacrylonitrile (PAN), a dielectric polymer with an index of refraction similar to that of glass ($n = 1.52$). The index of PAN was measured using an ellipsometer and is shown in **Fig. 12**(a). **Fig. 12**(b) shows a diagram of the

samples used. In tandem with sample fabrication we used a combination of analytical and numerical models to understand and design our samples. A setup utilizing an integrating sphere capable of quantifying the absorption, reflection, and transmission of diffracting devices was necessary, as standard UV-Vis spectrophotometers have limited capability for measuring diffracted and scattered light.

To measure the electrical properties, we created working OSCs on one side of a glass substrate with the desired PAN structured the other. Under illumination from a standard source we measured the current generated by the cells as the voltage was varied. From these measurements we determined the cell efficiency, fill factor, short-circuit current, open-circuit voltage, shunt resistance, and series resistance.

2.3 Concept Reviews

There are many concepts that permeate this work, both in device design as well as characterization. Before continuing with the details and results of our research, we present brief summaries of a number of the basic principles of optics tied to diffraction, solar cells, and metrology.

2.3.1 Diffraction and Scattering

Textured surfaces and their ability to increase the optical density in solar cells have been extensively studied [53]–[57], [63]. The enhancement factor, equal to the ratio of the optical intensity in a textured sample to that of a planar sample, is a standard metric for quantifying light harvesting. In 1982 Yablonovitch explored the maximum enhancement factor from using textured surfaces. The aptly named Yablonovitch limit, equal to $4n^2$, is the theoretical maximum enhancement factor achievable by the use of textured surfaces. The limit is found by calculating the number of photon states in a material in thermal equilibrium, and is only dependent on the refractive index, n [63]. The Yablonovitch limit assumes the active layer is much thicker than a wavelength, and the material is weakly absorbing, where the average path

length of light due to absorption is much longer than the cell thickness. To achieve the $4n^2$ limit, the textured surfaces must be Lambertian, where the intensity leaving the surface varies with the cosine of the angle from normal. All non-Lambertian surfaces, such as gratings and mirrors, have lower enhancement factors.

The absorption enhancement from weak absorbers is directly related to the enhancement factor. Rays propagating in a sample at an angle θ from the normal have larger path lengths and provide greater optical densities than normally propagating rays. In addition, reflectance generally increases with larger angles, further increasing the optical density.

The percent of light absorbed in a material with a complex refractive index, $N = n + i\kappa$, at a given wavelength, λ, is related to the optical path length according to the Beer-Lambert law:

$$A = 1 - e^{-\alpha l} , \qquad\qquad (6)$$

where A is the absorptance, l is the path length, and α is the absorption coefficient, which is equal to $4\pi\kappa/\lambda$ [46]. For weak absorbers, (6) can be simplified using the first two terms of a Taylor expansion, yielding

$$A = \alpha l \qquad\qquad (7)$$

In the weak absorber approximation l is the average path length of light over all angles and reflectances. We can easily see from (6) and (7) that increasing either the layer thickness or the propagation angles increases the amount of absorbed light. Although Lambertian scattering surfaces provide the greatest average path length enhancement, in practice, they are difficult to produce and are often approximated using diffraction gratings or etched pyramids [54], [61].

Diffraction gratings provide a precise way to manipulate light. The optical path difference between the periodic peaks and valleys of gratings forces incident light to interfere with itself. After passing through gratings and

reaching the far field, incident plane waves evolve into multiple plane waves propagating at fixed angles. Each propagation angle corresponds to a separate diffraction order according to

$$n_{\text{sub}}\sin(\theta_m) = n_{\text{i}}\sin(\theta_{\text{i}}) + \frac{m\lambda}{p},\qquad(8)$$

where n_{i} and n_{sub} are the refractive indices of the incident and substrate material, respectively, m is the order number, θ_m is the mth diffraction angle, θ_{i} is the incident angle, λ is the wavelength, and p is the period [46]. Propagation angles increase with wavelength and order number, and decrease with grating period.

The percent of light diffracted into each order can be derived for an arbitrary grating using scalar diffraction analysis by propagating the incident light to the far field. The diffraction efficiency for a plane wave incident on an arbitrary grating is

$$E_{m,n} = \left| \frac{1}{p_x p_y} \mathcal{F}_{\hat{x}} \mathcal{F}_{\hat{y}} \left\{ f_{p_x,p_y}(x,y) \cdot \text{rect}\left(\frac{x}{p_x}, \frac{y}{p_y} \right) \right\} \right|^2,\qquad(9)$$

where x and y are the spatial coordinates at the grating, p_x and p_y are the respective periods, $\mathcal{F}_{\hat{x}} \mathcal{F}_{\hat{y}}\{\ \}$ denotes the Fourier transform with variables $\hat{x} = m/p_x$ and $\hat{y} = n/p_y$, $f_{px,py}(x, y)$ is the functional form of the grating over one period, and rect(x/p_x, y/p_y) is the rectangle function (1 for $|x, y| \le p_x, p_y$; 0 otherwise) [64]. The diffraction efficiency, $E_{m,n}$, is only dependent on the wavelength, grating refractive index, and grating shape. Although it is included in (9), the grating period only serves to normalize the function and has no effect on $E_{m,n}$. In general, the majority of incident light is diffracted into the first few orders. The above equations predict that over 80% of the light is distributed among the 0 and ±1 orders for gratings with 700 nm periods and 350 nm depths as shown in **Fig. 13**(a).
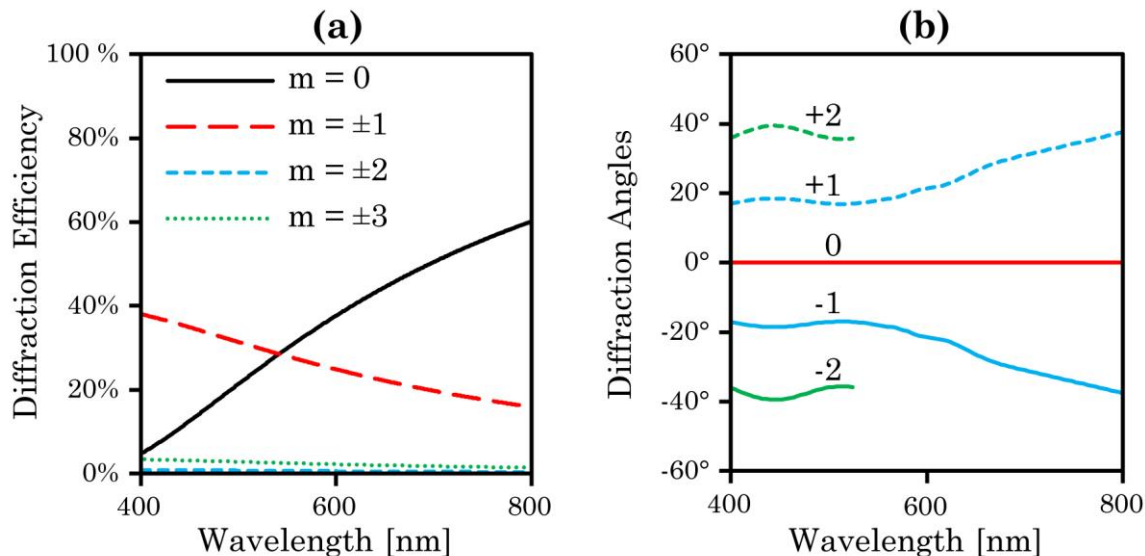
Fig. 13. Diffractive properties of linear square wave gratings with 700 nm periods, 350 nm depths, and 45% duty cycles calculated using scalar diffraction theory. (a) Diffraction efficiencies for the first four orders calculated using **(9)**. Over 80% of the light is in the 0 and ±1 orders. (b) Diffraction angles for the first three orders in a P3HT:PCBM layer calculated using **(8)**. The ±2 orders become evanescent at 525 nm.

Together, the above diffraction equations enable us to predict the average path length of light in any layer: the path length of each order is found from **(8)**, and the percent of light in each order is found using **(9)**. Although **(8)** and **(9)** predict an infinite number of orders, only a few of them propagate. As the wavelength increases relative to the grating period, so too does the propagation angle of a given order, until it reaches 90°, at which point the light becomes evanescent and is redistributed among the propagating orders [62]. The amount of light redistributed this way is generally low for wavelengths with the same magnitude as the grating period. **Fig. 13**(b) shows the diffraction angles of the first three orders in a P3HT:PCBM layer calculated using **(8)**. The ±2 orders stop propagating at 525 nm because they become evanescent. **(8)** and **(9)** can effectively predict the angles and distribution of diffracted light, but do not incorporate polarization effects.

In addition to being dependent on wavelength and grating shape, diffraction is also dependent on polarization. For linear gratings the components parallel (p) and perpendicular (s) to the plane of incidence have different reflectance, R, and transmittance, T, where we define the plane of incidence to be perpendicular to the wavevector defining the grating periodicity [56], [57], [65]. The role of polarization can easily be seen by viewing the total light passing through a grating. Diffracted light at longer wavelengths, and hence larger angles, becomes trapped in the sample due to total internal reflection (TIR) until it is diffracted back through the grating, resulting in a significant increase in reflectance, R and decrease in transmittance, T. To observe the differences between the s- and p-polarizations, we fabricated grating samples and measured the transmittance and reflectance of both components. The grating samples were also modeled using finite-difference time-domain (FDTD) analysis and the respective R and T were simulated. Glass and PAN were modeled with a refractive index of 1.5. Both modeled and measured R and T show that s-polarized light has a stronger interaction with the grating than p-polarized light, as seen in **Fig. 14**. Light trapping caused by TIR is desirable as it can dramatically increase the path length as seen in **Fig. 14**(d). The measured reflection curves in **Fig. 14**(b) also show that for light below 650 nm the average reflectance of p-polarized light for grating and planar samples was the same (8.5%), and the average reflectance of s-polarized light for textured samples was slightly higher (12%). From 650 – 800 nm the average reflectance increased to 20% for s-polarized light. High reflectance is undesirable but the increase in path length can make up for it.
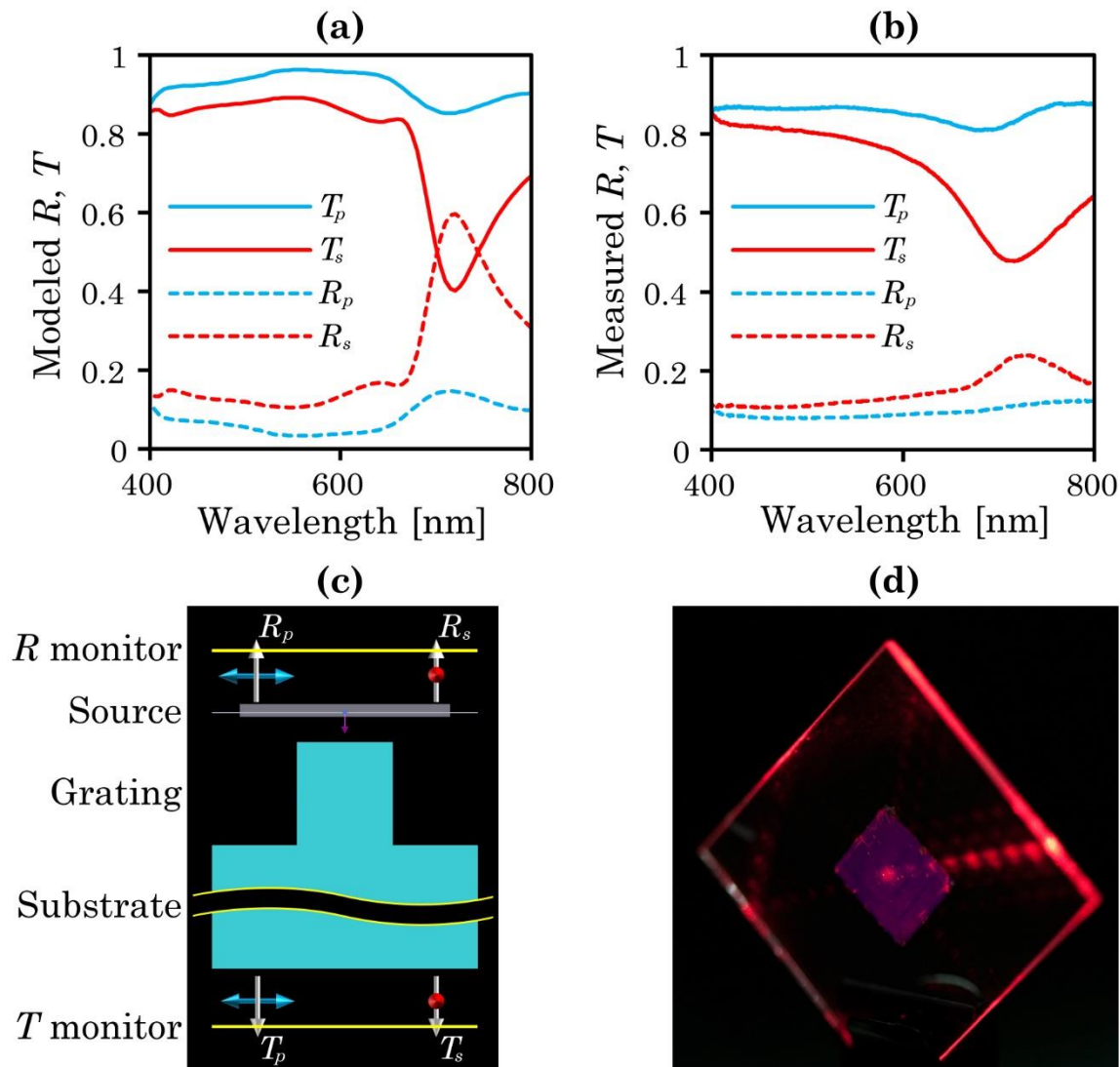
Fig. 14. Linear grating R and T of p- and s-polarized light on a glass substrate modeled using FDTD analysis (a) and measured using an integrating sphere (b). (c) shows the modeling approach used in the FDTD simulation. For both the modeled and measured gratings the s-polarized light had a much stronger interaction with the grating. The large feature starting at 700 nm was caused by total internal reflection: the ±1 transmitted orders would have an imaginary propagation angle, so their energy is instead redistributed among the reflected orders, resulting in increased reflection and decreased transmission. The magnitude of the feature is reduced in the measured case compared to the modeled case because of imperfections in the grating and the differences between the finite size of the measured grating and infinite size of the modeled grating. (d) shows an image of light trapped inside a glass substrate after striking a diffraction grating.

2.3.2 Total Internal Reflection

Total internal reflection occurs when oblique light incident on an interface completely reflects. This phenomenon can be predicted using Snell's law, which relates the propagation angles of waves incident on interfaces according to

$$n_1 \sin \theta_1 = n_2 \sin \theta_2 \,, \tag{10}$$

where n_1 and n_2 are the refractive indices and θ_1 and θ_2 are the propagation angles of the incident and substrate media, respectively. Oblique light bends towards the normal when passing from low to high index material, and bends away from the normal when passing from high to low index material. As the incident angle in high index material increases, the refracted angle in low index material increases at a faster rate until it reaches 90°. The incident angle in this case is called the critical angle. Light incident beyond the critical angle totally internally reflects back into the incident material. TIR is extremely useful for trapping light in a material as it results in lossless reflection. Light in a high index material beyond the critical angle continues to TIR until it is absorbed or scattered out. It is useful to note that the diffraction equation, **(8)** reduces to Snell's law, **(10)**, when m = 0. **(8)** and **(10)** can be combined to determine the wavelength, λ, where TIR will start to occur for a given period, p, and diffraction order, m. For normally incident light in air (n = 1), light diffracted into the ±1 order will begin to TIR when the wavelength is equal to the period, independent of the substrate index: $\lambda = p$. This simple relationship is useful for quickly determining what wavelengths will TIR, or which gratings should be selected to confine certain wavelengths.

We can take advantage of TIR by using gratings to diffract light beyond the critical angle inside solar cells. Once trapped, the light remains in the cell until it is absorbed or diffracted out. When trapped light beyond the critical angle reaches a diffraction grating, the majority reflects with the remainder being diffracted out of the cell. For textured samples, quantifying the amount of absorbed, diffracted, reflected, and transmitted light cannot be done using a

standard UV-Vis spectrophotometer, as the scattered components do not reach the detector. Instead, an integrating sphere is needed to capture the diffracted and scattered light.

2.3.3 Integrating Spheres

Integrating spheres provide an effective way to measure scattered light in reflection and transmission across a broad range of wavelengths. Their design is simple: they are hollow spheres coated with highly reflective, diffuse, and spectrally flat material. Light entering the sphere is uniformly reflected across the interior, where it continues to diffuse. Due to the highly reflective interior coating, light may reverberate hundreds of times before reaching the exit port of the sphere, where it is homogeneous and diffuse and can easily be measured with a variety of detectors.

The intensity of the light at the exit port can be derived by assuming the inner surface of the sphere is Lambertian. As mentioned above, light reflecting from Lambertian surfaces has an angular intensity profile proportional to the cosine of the angle from normal. A convenient consequence of this with regards to integrating spheres is that light incident from any angle on the interior of the sphere is evenly distributed across the surface of the sphere, greatly simplifying the formula for the exit port surface radiance. The wavelength dependent radiance at the exit port, after correcting for ports and non-ideal surface reflectance, is

$$L(\lambda) = \frac{R_{\text{inc}}(\lambda) \cdot \Phi(\lambda)}{\pi A_{\text{sph}}\left[1 - R_{\text{sph}}(\lambda) \cdot (1 - \Gamma)\right]} \left[\frac{\text{W}}{\text{m}^2 \cdot \text{nm} \cdot \text{sr}}\right], \qquad (11)$$

where $\Phi(\lambda)$ is the incident power entering the sphere, A_{sph} is the area of the sphere, $R_{\text{sph}}(\lambda)$ is the reflectance of the sphere wall, Γ is the fraction of total port area to sphere area, and $R_{\text{inc}}(\lambda)$ is the initial reflectance of the light incident on the sphere [66]. For reflectance measurements, $R_{\text{inc}}(\lambda)$ is the reflectance of the sample. In all other configurations $R_{\text{inc}}(\lambda)$ is equal to $R_{\text{sph}}(\lambda)$.
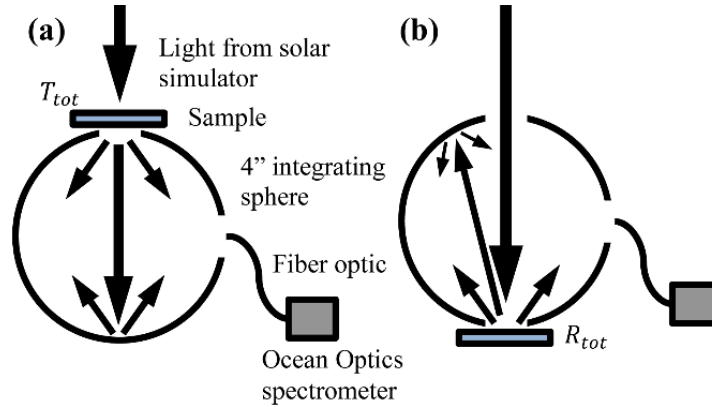
Fig. 15. Integrating sphere setup to measure (a) total transmission and (b) total reflection of scattering or diffracting samples. These results may be combined to determine the absorptance of the sample.

Rays reflect an average of $1/\Gamma$ times before escaping through one of the ports [67]. For most spheres the average number of reflections is between 50 and 1000, but can be even higher for large spheres with small ports and/or large volumes. Due to the large number of reflections, it is imperative that the reflectance be near unity and spectrally flat, as small amounts of absorption quickly compound. The sphere radius should be as large as possible relative to the ports to increase the radiant signal and reduce the amount of stray light entering and exiting the sphere. Lastly, the coating should be near Lambertian to ensure a uniform distribution at the exit port, where the light can then be measured. The total transmittance, T_{tot}, and reflectance, R_{tot}, can be rapidly measured by placing the sample at the entrance or exit ports of the sphere, respectively, as shown in **Fig. 15**.

Measurements obtained using an integrating sphere can be used to find various properties of samples. Light will either be specularly reflected, R_{spec}, diffusely reflected, R_{diff}, specularly transmitted, T_{spec}, diffusely transmitted, T_{diff}, or absorbed, A according to

$$1 = R_{\text{spec}} + R_{\text{diff}} + T_{\text{spec}} + T_{\text{diff}} + A \qquad (\ 12\ )$$

Integrating spheres measure the total reflectance, $R_{\text{tot}} = R_{\text{spec}} + R_{\text{diff}}$, and the total transmittance, $T_{\text{tot}} = T_{\text{spec}} + T_{\text{diff}}$, of a sample. The absorption of the sample is easily calculated using only an integrating sphere together with (12). UV-Vis spectrophotometers measure only the specular components, R_{spec} and T_{spec}, which are insufficient to determine the absorptance of a scattering sample. However, UV-Vis measurements can be combined with integrating sphere measurements to isolate the scattered or diffracted components according to

$$R_{\text{diff}} = R_{\text{tot}} - R_{\text{spec}} \qquad\qquad (13)$$

$$T_{\text{diff}} = T_{\text{tot}} - T_{\text{spec}} \qquad\qquad (14)$$

Integrating spheres allow for a vast variety of samples to be measured. **Fig. 16** shows the results from measuring a transparent honeycomb Au lattice, a nanoparticle composite used in all-optical magnetometers [68], a leaf, and the photonic structures on a moth wing, which all require an integrating sphere to be correctly characterized.

(a) Au Lattice

(b) MO Nanocomposite

(c) Leaf

(d) Moth Wing
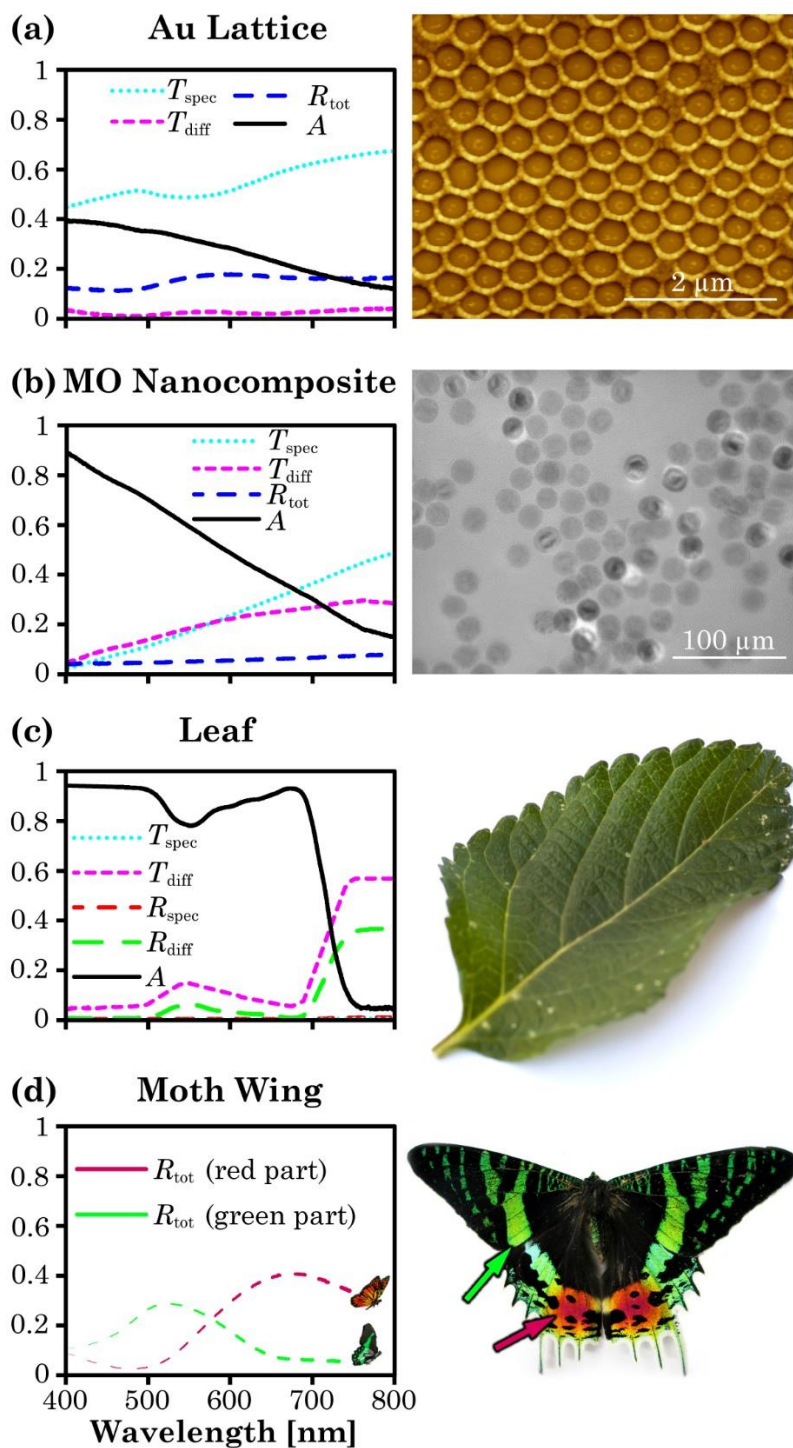
Fig. 16. Spectra of various samples demonstrating the importance of using both an integrating sphere and a UV-Vis spectrophotometer to measure scattered transmittance, scattered reflectance, and absorptance. (a) Transparent Au honeycomb lattice. (b) TEM image of cobalt ferrite nanoparticles used in magneto-optic (MO) nanocomposite based magnetometers (right). Plot of cobalt ferrite based polymer nanocomposite film optical properties (left). (c) One of nature's solar cells: a leaf. (d) Photonic structures on a moth wing.

2.3.4 Solar Cell Electrical Properties

There are several significant solar cell parameters that can be determined by measuring the current produced while sweeping voltage under illumination. These are illustrated in **Fig. 17**. During each measurement the cells are illuminated with a solar simulator, a source that simulates the spectrum and intensity of the sun. When illuminated the cells produce current, which varies with the applied voltage. The current produced when no voltage is applied is called the short-circuit current (I_{SC}). The voltage across the cell when no current is flowing is called the open-circuit voltage (V_{OC}). V_{OC} is largely determined by the materials making up the solar cells and their respective energy levels, whereas I_{SC} is related to the total amount of current produced by the solar cell and increases with the solar cell area and illumination

Sample Organic Solar Cell I-V curve
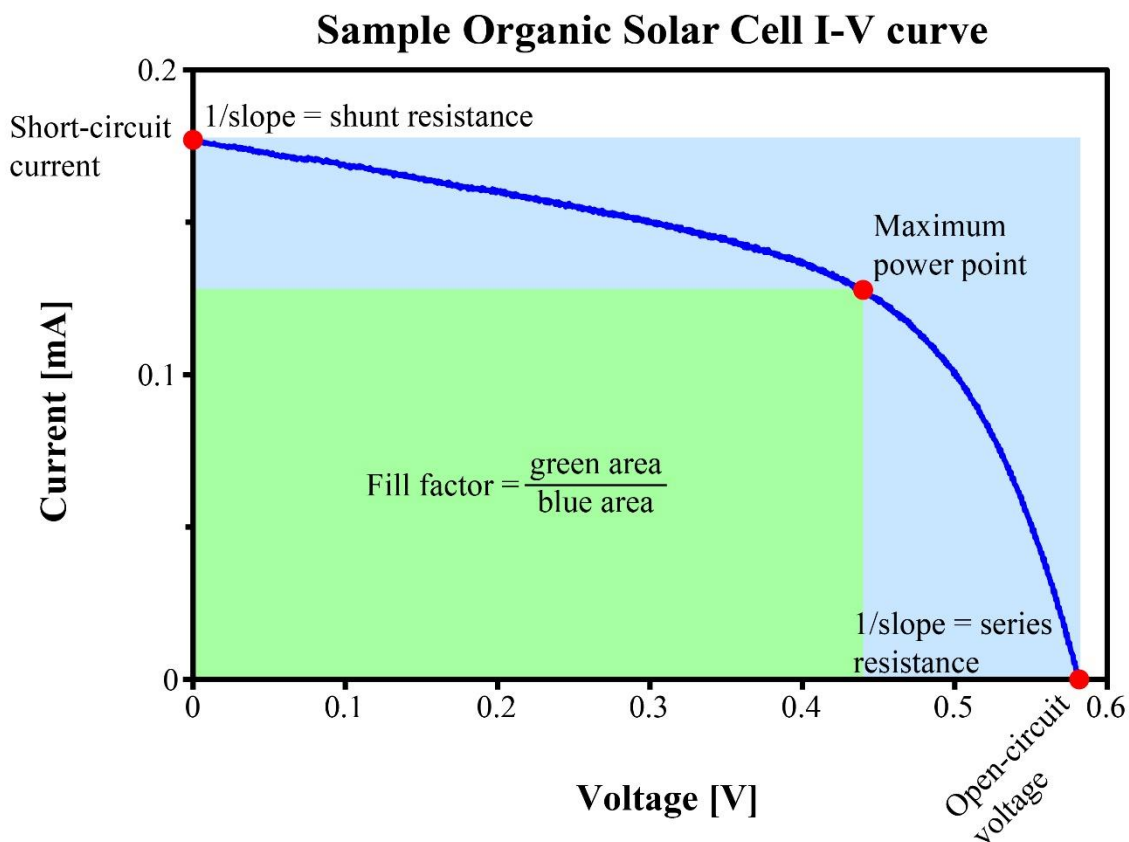
Fig. 17.   Sample IV curve illustrating the various electrical parameters.

intensity. The electrical power produced by the cell is equal to the product of the voltage and current, as shown in (15):

$$P_{\text{out}} = I \cdot V \qquad (\text{ 15 })$$

There will be a point along the IV curve where the power is maximized, P_{max}: this is called the maximum power point. The inverse of the slope of the IV curve when the voltage is zero is the shunt resistance, R_{SH}. The shunt resistance indicates how much current takes an alternate path through the circuit (i.e. via small shorts in the solar cell layers). Ideally R_{SH} should be infinite. The inverse slope of the IV curve when the current is zero is the series resistance, R_{S}. R_{S} tells us how much resistance is present in the circuit. R_{S} should ideally be zero to reduce the amount of energy lost to resistive heating. The fill factor, *FF*, is the ratio of the maximum power output to the product of the short-circuit current and open-circuit voltage:

$$\text{FF} = \frac{P_{\text{max}}}{I_{\text{SC}} \cdot V_{\text{OC}}} \qquad (\text{ 16 })$$

FF gives an indication of the quality of the IV curve: for a given V_{OC} and I_{SC}, cells with higher FFs are more ideal with higher R_{SH}, lower R_{S}, and greater P_{max}. The last, and most significant, parameter is the efficiency, which is defined in (5), but can also be measured by taking the ratio of the output electrical power to the incident optical power:

$$\text{Efficiency} = \frac{P_{\text{max}}}{I_{\text{inc}} \cdot A_{\text{cell}}}, \qquad (\text{ 17 })$$

where I_{inc} is the incident irradiance and A_{cell} is the area of the cell.

2.4 Device Design

The goal of this work is to design a grating structure that diffracts light at large angles into the photoactive layer of the OSC. There are many trade-offs to consider when designing a grating. Shorter periods diffract light at larger angles, but may cause all the diffraction orders to become evanescent at longer wavelengths and have the light redistributed among lower orders. Taller structures increase the fraction of light in the first order, but are difficult to manufacture. Linear gratings have high diffraction efficiencies, but are only effective for one polarization of light.

Considering the above factors as well as commercial availability, a linear square wave silicon grating with 700 nm period, 350 nm depth, a 55% duty cycle, and an area of 8 mm × 8.3 mm was selected for use as a mold for forming gratings in polymers. Over the absorption range of P3HT:PCBM (from 400 nm to 650 nm), **(8)** and **(9)** predict that imprinted dielectric gratings (with $n =$ 1.5) diffract 23% of the AM1.5 spectrum into the 0th order and 62% into the +/-1 orders. The remaining 15% is in evanescent orders, and distributed between the 0th and +/-1 orders. Two separate two-dimensional gratings with posts on a square grid and hexagonal grid were also used to diffract both *s*- and *p*-polarizations. The 2-D silicon grating molds had posts with 350 nm diameters, spacings of 700 nm, heights of 350 nm, and spanned 8 mm × 8.3 mm. The molds were used to imprint PAN on glass substrates [69]. PAN was used due to its clarity, strength, and chemical stability.

To measure the absorption enhancement for various active layer thicknesses, 15 nm, 40 nm, and 120 nm layers of P3HT:PCBM were spin cast onto the opposite sides of the substrate from the PAN gratings as shown in **Fig. 12**(b). The active layer thicknesses that yielded the greatest enhancement (40 nm) were used to make working cells to test their electrical output enhancement.

As stated above, previous researchers have textured the absorbing and reflecting layers of OSCs. These methods have many issues. In addition to

introducing many unknown variables, patterning the active layers can cause problems in fabrication and increase production time and complexity. Texturing the active layer restricts the aspect ratio, as tall and narrow structures create shorts between the cell layers. In addition, textured electrodes generally have greater electrical resistance due to their increased surface area.

Applying gratings to the opposite side of the substrate from the organic layers avoids shorting and increasing the electrode resistance, and ensures a high index contrast at the grating interface, a necessity for high diffraction efficiency. The fabrication process is also unaffected by the addition of the gratings, as the chemical and structural stability of PAN allows the gratings to be patterned months, or even years, before the cells are made. PAN gratings are also strong enough to be placed in the vacuum seal of a spin coater without compromising their integrity, enabling the opposite surface to be coated with various materials.

2.5 Device Fabrication

2.5.1 Nanoimprinting PAN

A 15wt% solution of PAN in dimethylformamide (DMF) was first created. This required 7.11 g of PAN (powder) and 50 ml of DMF. An oil bath was placed on a hotplate and 3-headed flask attached to a Liebig condenser was half submerged in the bath so there was a 1 cm gap between the flask and the base of the bath. 50 ml of DMF was added to the flask. A magnet stirrer was placed in the DMF and a larger one was placed in the oil bath and set to spin at 300 RPM. The hot plate was set to 165 °C and the oil and DMF were heated for 60 minutes. Roughly half of the PAN (3.6 g) was then added to the DMF and submerged with a metal spatula. Every 15 ~ 30 minutes 0.5 g of PAN were added and submerged in the mixture until all the PAN was dissolved. As the PAN solution thickened the magnet stirrer speed was reduced as necessary to keep it spinning (generally ending near the minimum speed). Once the PAN

was dissolved the solution was removed from the heat and poured into a glass vial and sealed with Parafilm for later use. This produced enough solution to make 20 – 30 8 mm × 8.3 mm gratings on 1" × 1" substrates.

1" × 1" glass slides were used as substrates for the patterned PAN to be transferred to. The glass slide preparation is described below in section **2.5.2**. If the gratings were only going to be used for absorption measurements, then uncoated glass was used instead of glass coated with ITO. The desired 8 mm × 8.3 mm silicon mold was cleaned with acetone and isopropanol then placed in in a plasma etcher for 5 minutes to remove any organic residue. It was placed on a spin coater and a drop of the PAN solution was added to the surface. It was spin cast at 2500 RPM with an acceleration of 200 RPM/s for 1 minute. The mold was added to a hotplate that had previously been set to 150 °C for 1 minute in order to bake off the solvent and cross-link the PAN. While the mold was heating, a glass substrate was added to the spin coater and the surface was completely coated with a few drops of the PAN solution. The substrate was spun at 6000 RPM with an acceleration of 200 RPM/s for 1 minute. Applying a thin layer of PAN to the substrate ensured that the textured PAN film would firmly adhere to it. While the substrate was spinning the mold was removed from the hot plate. After spinning and baking the mold, there was usually a layer of PAN on the sides of the mold that needed to be removed. To remove the PAN, each side of the mold was pressed against double-sided tape that was attached to the work bench. The substrate was removed from the spin coater and placed on the workbench. Using tweezers, the patterned PAN layer was gently removed from the mold surface and rolled onto the substrate (to prevent bubbles) with the textured side facing up. Multiple gratings were made by repeating this process. For the absorption measurements a single grating was placed on each 1" × 1" glass substrate, and for the electrical measurements six gratings were placed on each ITO-coated substrate. Once the desired number of samples were made, they were allowed to dry for 24 hours. **Fig. 18** shows photos of linear PAN gratings as well as scanning electron microscope images
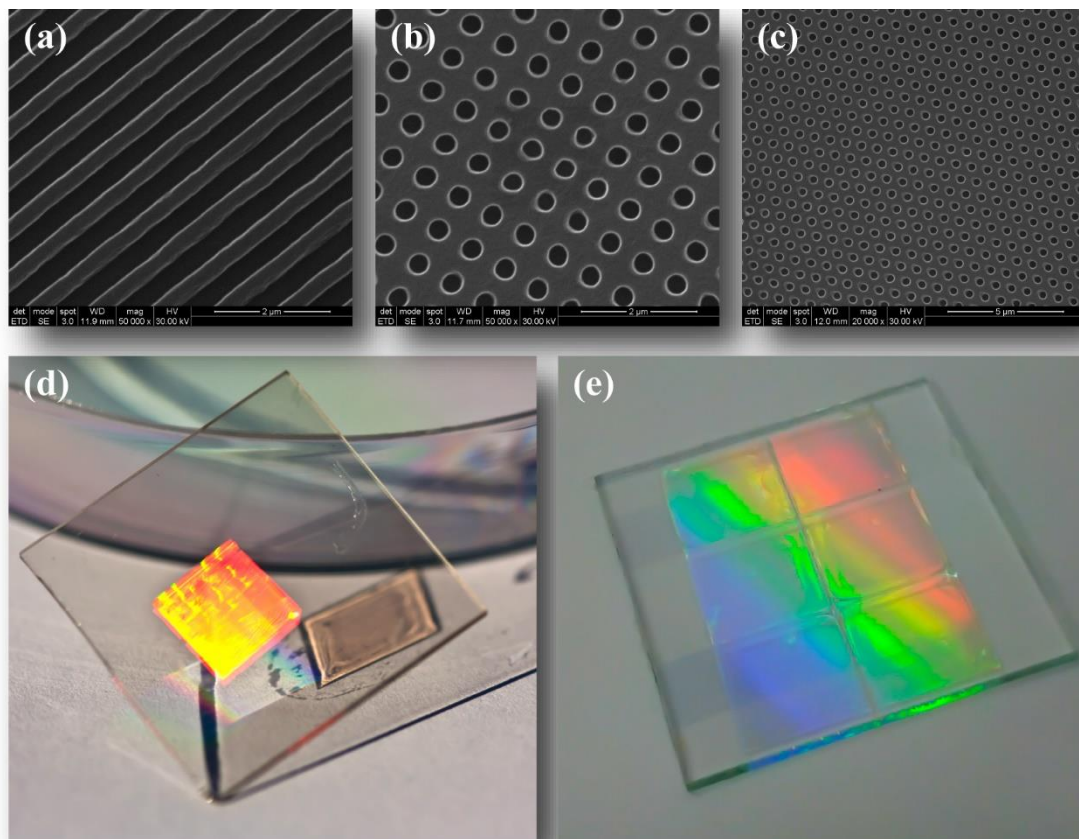
Fig. 18. SEM images of polyacrylonitrile gratings with 700 nm feature spacings and 350 nm depths: (a) linear grating; (b) rectangular grating; (c) hexagonal grating; (d) PAN linear grating on a glass substrate for absorption measurements; and (e) six PAN linear gratings for solar cell electrical measurements.

of linear, rectangular, and hexagonal gratings. The SEM images show that the silicon molds successfully imprint onto the PAN.

2.5.2 Solar Cell Fabrication

Creating working solar cells took at least two days to complete and involved dozens of steps. Using the procedure outlined below, we were able to create three substrates each with four working solar cells.

1" × 1" glass slides were used as the substrates. These were cut from glass sheets pre-coated with Colorado Concept ITO. To ensure alignment during deposition and etching, an asterisk was scribed into one of the corners of each slide. The slides were rinsed with DI water, then acetone, then isopropanol. A

solution of 50 ml DI water with 1 drop of Triton X-100 surfactant was made in a staining jar. A microfiber towel was dipped in the solution and used to wipe the surfaces of the slides before placing them in the staining jar. The slides in the surfactant solution were sonicated for 30 minutes. The slides were then thoroughly rinsed with DI water and placed in a new staining jar filled with DI water and sonicated for 15 minutes. The slides were rinsed with DI water again and the water in the staining jar was replaced with ethanol. They were sonicated for 15 minutes.

The ITO was etched into an "H" shape on each slide to allow for 4 separate cells to be connected with a single electrical contact. S1813 photoresist was spincast onto the ITO at 3000 RPM with an acceleration of 600 RPM/s. The slides were added to a 115 °C hotplate and baked for 60 seconds. A single slide was taped to the ITO mask with the ITO facing the mask, and the scratched corner pressed closest to the scratch on the mask (**Fig. 19**(a, c)). Each slide was always aligned to the same corner when placed in the ITO mask, aluminum mask, and measurement mount to reduce misalignment and ensure that the pins would always touch the aluminum contacts. The slide was exposed under a UV lamp for 60 seconds. While the mask was capable of holding up to four slides, we had better results when exposing only a single slide at a time. Relative to the orientation in **Fig. 19**(a), for every three slides, two were placed in the top left position and one was placed in the bottom left position to keep the correct orientation of the "H" when three slides were simultaneously mounted in the aluminum mold later on (**Fig. 19**(b, d)). After exposure each slide was agitated in a solution of 50 ml DI water and 10 ml 351 developer for 15 seconds then rinsed with DI water and wiped with a tissue to remove the developed resist. Each slide was then agitated in concentrated hydrochloric acid for 3 minutes to etch the ITO then rinsed with DI water. The etched portions of each slide were tested with a multimeter to ensure their conductivities were zero. If any of the etched portions were still conductive, the slides were etched in 30 second intervals until the conductivity reached zero.
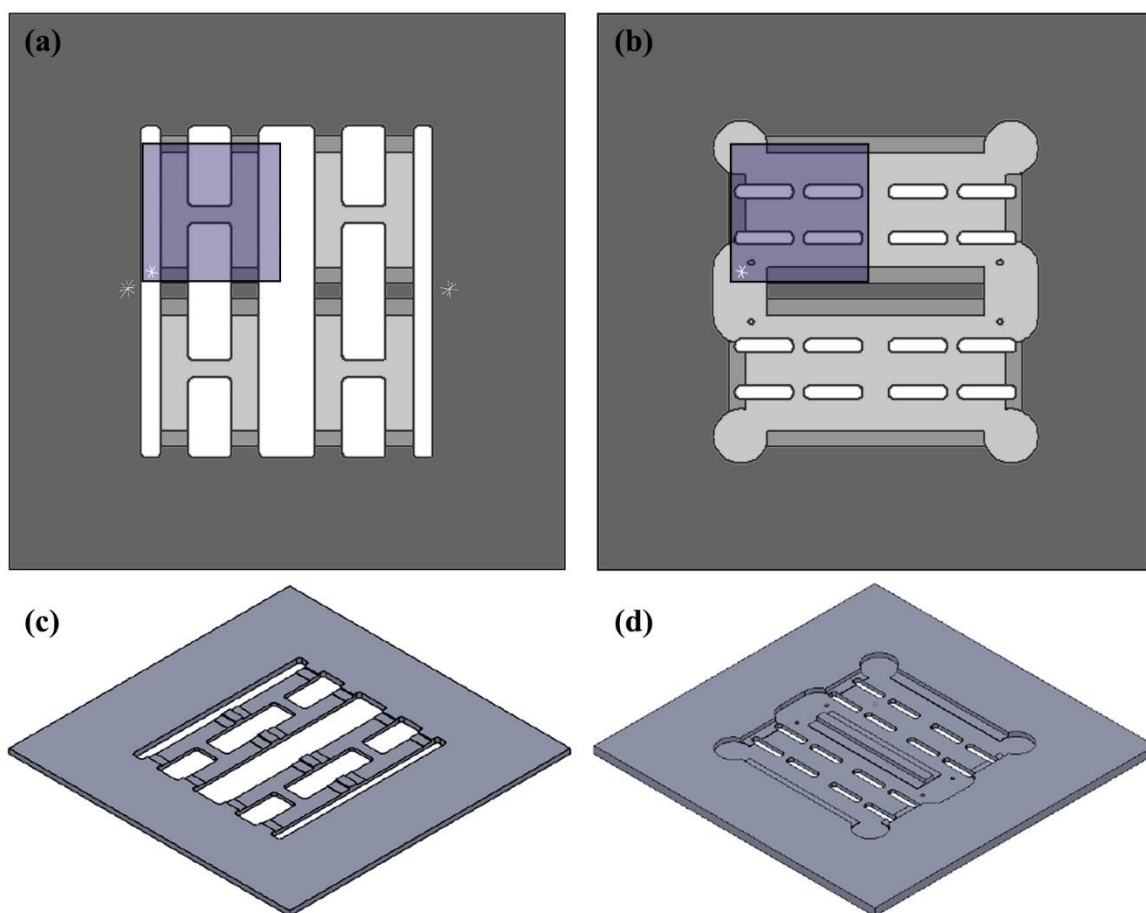
Fig. 19. Aluminum and ITO solar cell masks. (a) Top view of the ITO mask. (b) Top view of the Al mask. (c) Isotropic view of the ITO mask. (d) Isotropic view of the Al mask. Placement of the 1" × 1" substrates is shown in (a) and (b). Overlaying the four rounded rectangular aluminum contacts on the rectangular legs of the ITO "H" ensured that the cell area would always remain a constant 12.5 mm² even with misalignments during the deposition steps.

The resistance of the ITO from the center of the "H" to the corners was generally 50 ohms. At this point the "H" pattern of the ITO was inspected in reflection. Samples with the correct pattern were kept, and samples that were over-etched or had blurred edges were discarded. Batches of 10 − 25 etched ITO samples were made at once and stored for later use.

P3HT:PCBM preparation took about a day, but could be carried out in tandem with cleaning and etching the ITO slides, as many of the steps required long periods of sonication. The following procedure produced enough for 3 − 6 solar cells. 30 milligrams of dry P3HT was weighed and placed in a 4 ml amber

vial. 30 milligrams of dry PCBM was also weighed and placed in a second 4 ml amber vial. 1 ml of 1,2-dichlorobenzene was syringed into each of the vials. The vials were capped and wrapped with Parafilm. The amber vials were halfway submerged in water in a larger glass beaker (~ 100 ml), and the beaker was then halfway submerged in a sonicator for 5 hours until the P3HT and PCBM dissolved. The PCBM solution was syringed into the P3HT vial and capped and wrapped with Parafilm, after which the P3HT:PCBM solution was sonicated for 30 minutes. The solution could be stored for up to a week without degradation in performance.

With the above steps complete, three solar cells could be assembled in one batch. 2 ml of poly(3,4-ethylenedioxythiophene) polystyrene sulfonate (PEDOT:PSS) was drawn into a syringe. The needle was replaced with a 0.1 μm polyvinylidene difluoride filter. Before coating, substrate slides were plasma cleaned with the ITO side facing up for 2 minutes to help improve the adhesion of the PEDOT:PSS to the surface. The slide was immediately placed on the spin coater and coated with PEDOT:PSS, which was spun in two steps: 1800 RPM with a 200 RPM/s ramp, followed by 4000 RPM with a 200 RPM/s ramp. The cell was baked in a preheated oven at 140 °C for 10 minutes, which produced a 40 nm layer of PEDOT:PSS. This process was repeated to make a total of three coated slides.

P3HT:PCBM solution was drawn into a glass syringe and the needle was replaced with a 0.2 μm polytetrafluoroethylene filter. Enough P3HT:PCBM solution was deposited on the slide to completely cover it. Depending on the desired thickness of the active layer, the slides were spun at rates between 500 and 1800 RPM with a 200 RPM/s ramp for thicknesses between 120 and 40 nm, respectively. After coating, the three slides were baked together in an oven that was preheated to 100 °C for 10 minutes. During baking, the air in the oven was evacuated then replaced with N_2 to limit the amount of oxidative decay.

LiF buffer layers and Al contacts were vacuum evaporated onto the cells. The vacuum chamber (bell jar) and thermal sources were located within a

larger sealed glovebox that was always filled with N_2. The three slides were added to the aluminum mask so that the scribed corners were pressed towards the alignment holes in the center left or center right of the mask, and the ITO "H" was vertical relative to the orientation in **Fig. 19**(b). The slides were taped in place with Kapton tape and the mask was placed in the mask holder within the vacuum chamber. Due to limited space inside the vacuum chamber, the shutter in the "open" position would block a corner of the mask. This is why only three of the four mask substrate positions could be occupied at a time. Chilled water was continually run through piping that made contact with the mask to cool the substrates during deposition. Once the cells were mounted and lithium fluoride and aluminum were added to the chamber, low vacuum was created with a mechanical pump. High vacuum was then reached over a period of 4 hours using a diffusion pump. A crystal oscillator inside the chamber was used to monitor the deposition rates. Current was supplied to the LiF until the deposition rate was $0.5 - 1$ Å/minute, and the shutter was opened until 8 Å were deposited. Current was applied to the aluminum until the deposition rate reached $1.5 - 1.8$ Å/s. The shutter was opened until all the aluminum was deposited onto the cells ($80 - 100$ nm).

After thermal deposition, the cells could be measured immediately or left in the chamber overnight and measured the next day. The solar cell performance would drop off several hours after exposure to oxygen and moisture. **Fig. 20** shows how the cell efficiency drops off over time as well as an image of a fabricated solar cell with linear nanostructures on the backside.

2.6 Measurement Setup

The effect of adding diffraction gratings to organic solar cells was investigated in two ways: by measuring the absorption in organic solar cell layers, and by measuring the generated electrical power. The generated current is directly proportional to the amount of absorbed light in the active layers, so measuring the absorption is an effective method for determining how the device will
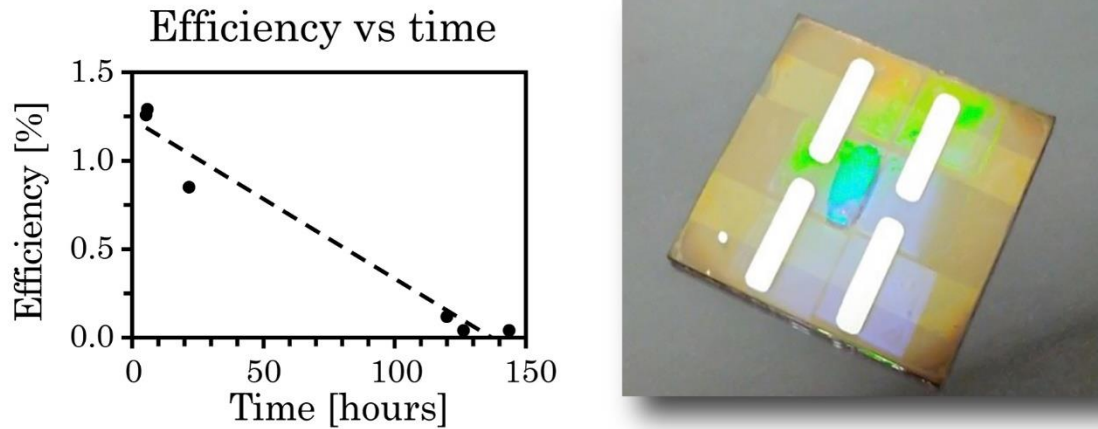
Fig. 20. Cell efficiency vs time (a), and diagram of four P3HT:PCBM solar cells with linear diffraction gratings (b).

respond when gratings are added. Absorption is also measured over a band of wavelengths, which provides insight into how the light behaves in the system. Additionally, only the active layer of the solar cells needs to be created to measure the absorption. This significantly reduces the time and supplies needed to make samples.

Once the appropriate active layer thicknesses have been determined, full devices can be fabricated and their current vs voltage (IV) curves and efficiencies can be measured. Device efficiencies are the main metric used to compare solar cells. Although efficiency measurements are more difficult to obtain and give less information about how light behaves inside the cells, they are crucial for evaluating device performance.

Our setup for measuring absorption consisted of an integrating sphere, source, and spectrometer. The integrating sphere was 4" in diameter and coated with Spectraflect, a highly reflective and spectrally flat scattering material. The entrance port, used for transmittance measurements, was 3 mm in diameter, and the reflectance port was 12.6 mm in diameter. A 1000 W/m² Oriel solar simulator (model # 91191) was used for all spectral measurements. Inside the simulator light from a xenon arc lamp is collected by an ellipsoidal
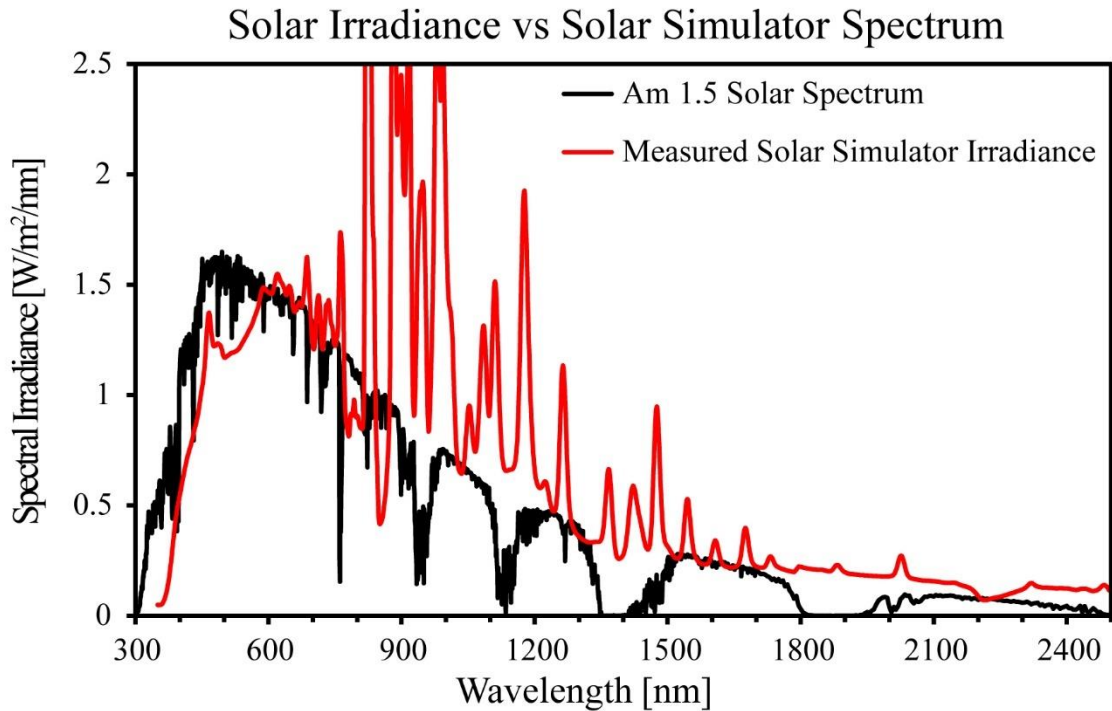
Fig. 21. Solar simulator spectrum and AM 1.5 solar spectrum . The solar simulator spectrum was found by illuminating a Spectralon panel (highly reflective and Lambertian) and measuring the reflected radiance with an ASD FieldSpec full-range spectroradiometer.

mirror before being sent through an optical integrator for spatial homogenization. The beam then passes through an AM 1.5 filter and a collimating lens. The output of the lamp is a semi-collimated 2" × 2" beam with uniform intensity matching that of the sun. **Fig. 21** shows that the spectrum of the simulator closely matches that of the sun, ensuring that spectral mismatch is minimized [70]–[72]. The large peaks in the NIR are xenon emission lines, and are outside the absorption band of silicon and organic solar cells so they do not influence the measured performance. The radiance inside the sphere was measured using a portable Ocean Optics USB4000 spectrometer and the data were recorded using SpectraSuite. The specular reflectance and transmittance were measured using a Cary 5000 UV-Vis-NIR spectrophotometer.
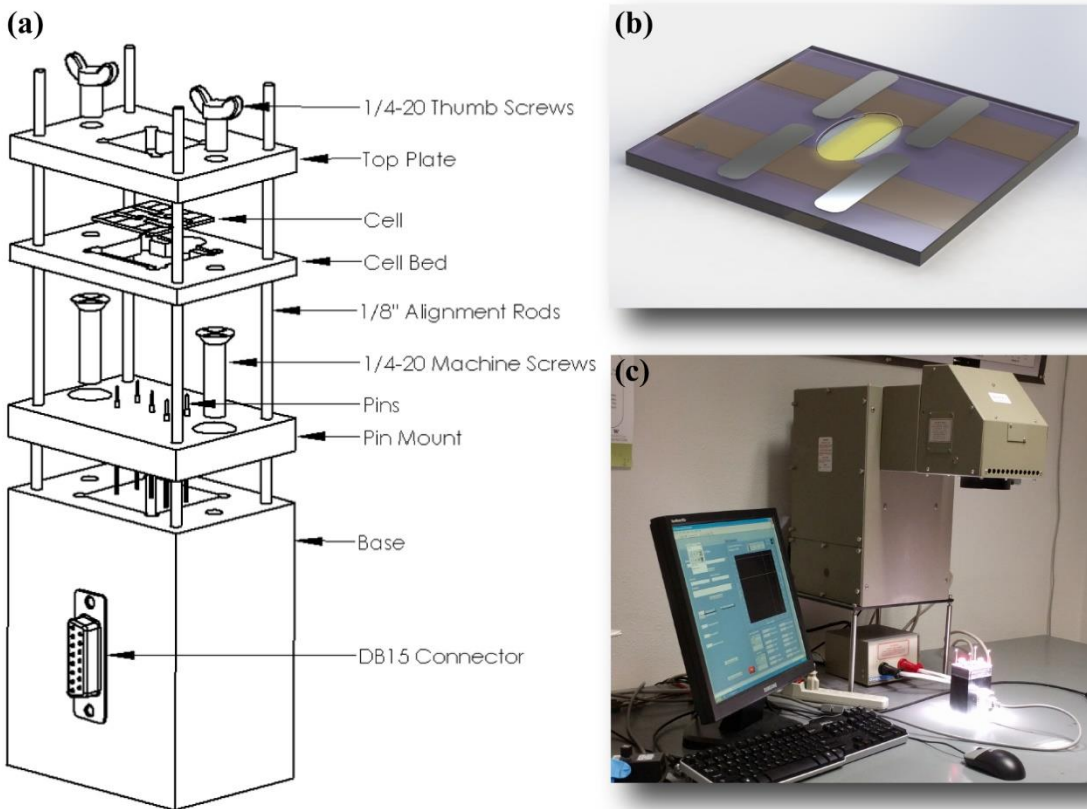
Fig. 22. Characterization components. (a) Exploded view of the solar cell mount. (b) Rendering of the solar cell geometry. The yellow/brown "H" is ITO and the metallic strips are aluminum. The active layer sits between the ITO and aluminum and completely coats the substrate. The metal dot in the corner of the cell was used to orient the cells. (c) Solar simulator illuminating a mounted solar cell with the measurement VI running on the PC.

To measure the electrical output, we used a mount for the cells, a Keithley SourceMeter, the same solar simulator as above, and a custom LabVIEW VI. The cell mount was a custom design that secured and made electrical contact with 1" × 1" glass substrates, each coated with four solar cells. Four pins touched the aluminum contacts of the cells, and a central pin touched the central common ITO contact. The P3HT:PCBM was removed in the center of the cell after deposition of the materials to allow for better contact with the ITO. **Fig. 22** shows the cell mount design, a rendering of a solar cell, and the solar simulator. Each cell had an area of 12.5 mm^2, which was determined by the overlapping region of the ITO and aluminum.

The solar simulator intensity had to be calibrated before making electrical measurements. The references for calibration were one of four Hamamatsu silicon solar cells. Silicon cells were used because their electrical properties are very stable over multiple years. The cells chosen were precoated with absorption filters that adjusted the responsivity of the cells to match those of typical organic solar cells (responsive from $350 - 650$ nm). Using reference cells with similar responsivities to organic cells was important to reduce spectral mismatch [70]–[72]. The IV curves and spectral responsivities of the reference cells were characterized by the National Renewable Energy Laboratory (NREL) using a standardized source. To calibrate the solar simulator, one of the four reference cells was illuminated and I_{SC} was continually monitored with the custom LabVIEW VI. The output of the solar simulator was then adjusted until the reading of I_{SC} matched the measured value from NREL. At this point the output of the solar simulator matched that of the AM 1.5 solar spectrum, and organic solar cells could be measured. Calibration was performed regularly.

2.7 Results and Discussion

2.7.1 Absorption Enhancement

The fraction of light diffracted from the linear, rectangular, and hexagonal gratings as a function of wavelength is shown in **Fig. 23**(a). The linear gratings diffract more *s*-polarized light than *p*-polarized light. Due to their symmetry, the rectangular and hexagonal gratings diffract *s*- and *p*-polarizations equally (at normal incidence). However, the total fraction diffracted is much less for the two-dimensional gratings than the linear gratings. Part of the reason for this is that the ratio of the area taken up by mesas and valleys is roughly 1:1 for the linear gratings, and only 1:4 and 1:3 for the rectangular and hexagonal gratings, respectively. Due to their greater diffraction efficiency, only the linear gratings were used to measure the absorption enhancement of P3HT:PCBM.
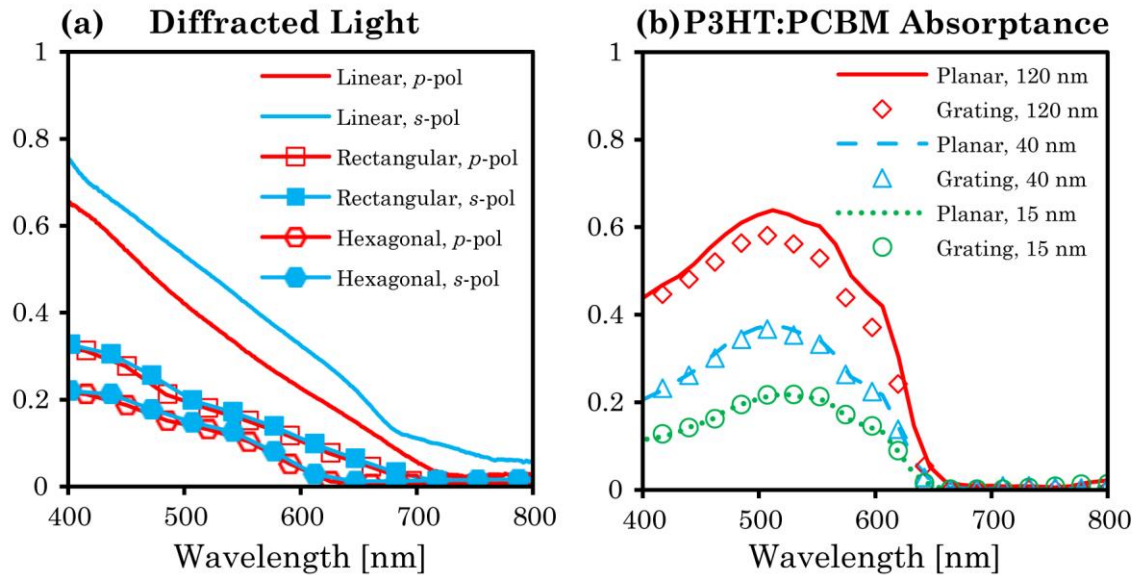
Fig. 23. Diffraction and absorption from gratings. (a) Fraction of diffracted light from linear, rectangular, and hexagonal gratings measured using an integrating sphere and UV-Vis spectrophotometer. (b) Absorptance of P3HT:PCBM layers of various thicknesses with and without gratings applied to the opposite side of the substrate. Absorptance was relative to the total light incident on the sample.

The absorptance of the various P3HT:PCBM layers with and without diffraction gratings from 400 nm to 800 nm was measured with an integrating sphere, and is shown in **Fig. 23**(b). The total fraction of absorbed light was calculated by integrating the product of the AM 1.5 spectrum and the measured absorptance. The 120 nm samples show a reduction in absorption when the grating is added, with 51.2 ± 1.6 % of the incident light absorbed without a grating, and 46.4 ± 1.7 % with a grating. The absorptances in the 40 nm samples are also reduced with the addition of a grating, but the reduction is less significant and within the uncertainty of the measurement, with 28.0 ± 1.4 % of the light being absorbed without a grating, and 27.2 ± 2.3 % with a grating. The 15 nm samples continue the trend of reducing the difference of the organic layer absorptance between the planar and grating samples to the extent that the respective absorptances are equal. The planar samples absorb 15.9 ± 0.1 % of the light and the grating samples absorb 16.0 ± 0.8 %, practically equivalent given the uncertainty in the measurement.

Fig. 24. Light confinement. (a) Light-confinement for the PAN gratings on glass substrates used in this study. Light at longer wavelengths TIRs and is confined in the device. A small fraction of the confined l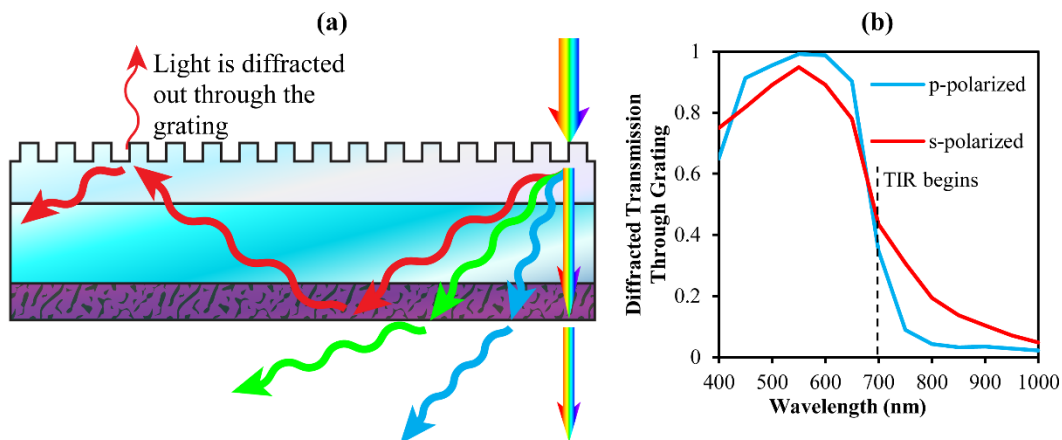ight diffracts out of the cell. (b) Fraction of light in the ±1 orders that exits the substrate through the grating. Wavelengths greater than 700 nm are confined in the sample, and have minimal leakage through the grating. The plot was calculated using FDTD analysis for a square wave grating with 700 nm period, 350 nm height, and index of 1.5. A separate simulation was run for each wavelength. The +1 order diffraction angle, θ_m, was calculated using **(8)**. A monochromatic plane wave source at angle θ_m was inserted in a glass medium with a diffraction grating at its surface. A transmission monitor was used to measure the light diffracted out through the grating.

There are four reasons for the reduction in measured absorption when gratings were used: increased reflectance, light-confinement, the small grating size, and saturation. The increase in the reflectance was previously discussed and is shown in **Fig. 14**. For the linear gratings used, the measured reflectance for *s*-polarized light (the polarization which receives a path length enhancement) over the absorption band of P3HT:PCBM (400 – 650 nm) is 12%. This includes the reflectance from the planar surface, which is 4%. The reflectance from only the grating is 8%, which is double that of a planar surface. This extra 4% is lost before any light enters the sample.

The second factor contributing to the reduced absorption is light-confinement, which refers to rays diffracted beyond the critical angle that propagate laterally through the cell and are unmeasured, as shown in **Fig. 24**(a). A portion of the light confined this way diffracts back out through

the grating but the majority remains trapped in the cell until it is absorbed or exits the edges of the substrate. **Fig. 24**(b) shows the fraction of light in the ±1 orders that exits the sample through the grating. Wavelengths less than 700 nm have high transmission through the planar and grating interfaces, and are poorly confined. Conversely, wavelengths greater than 700 nm are completely reflected at the planar interface, and mostly reflected at the grating interface, resulting in high confinement and greatly enhanced path lengths. Light at shorter wavelengths that diffracts into higher orders (and angles) also has high confinement.

The third factor contributing to the reduction in the measured absorptance is the small grating size, or small grating effect. Due to the limited size of the gratings in this study, only the absorption of rays diffracted at small angles was measured. Rays diffracted at sufficiently large angles travel laterally as they propagate through the 1 mm glass substrate and overshoot the measurement port of the integrating sphere, reducing the amount of measured light. **Fig. 25**(a) illustrates this effect. This reduction is merely an artifact caused by the limited size of the gratings used in this work. If larger gratings were used, the amount of light overshooting the measurement port would be equal to the amount of light entering the port from neighboring regions, thereby negating this effect and increasing the absorptance.

The small grating effect and light-confinement can easily be quantified by using an integrating sphere to measure $1 - R_{tot} - T_{tot}$ of a glass substrate with a PAN grating. Neither glass nor PAN is significantly absorbing from 400 nm − 800 nm, so the quantity $1 - T_{tot} - R_{tot}$ will only be nonzero when light is confined to the substrate and does not enter the integrating sphere. **Fig. 25**(b) shows $1 - R_{tot} - T_{tot}$ for planar and grating samples with and without 40 nm P3HT:PCBM layers. As expected, all the light leaving the uncoated glass substrate is accounted for, yielding $1 - R_{tot} - T_{tot}$ = 0. Yet when a PAN grating is added, roughly 8% of the light with wavelengths between 400 nm and 650 nm, and as much as 20% with wavelengths beyond 650 nm is unaccounted for
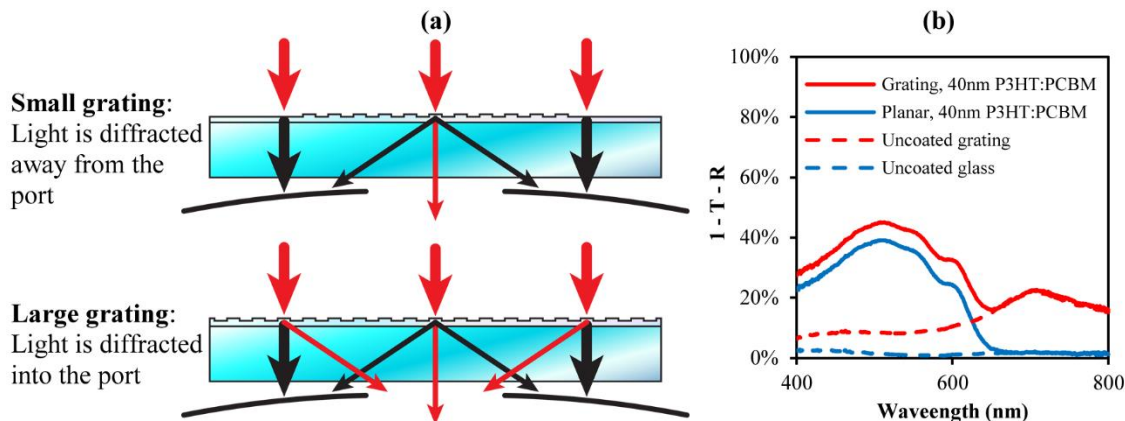
Fig. 25. Small grating effect. (a) Graphic of light passing through small and large gratings and entering the entrance port of an integrating sphere. Light is diffracted away from the entrance port, reducing the amount absorbed. Large gratings diffract light away from the port, but also diffract light into the port from neighboring sections. (b) The quantity $1 - R_{\text{tot}} - T_{\text{tot}}$ for glass substrates with and without PAN gratings and/or P3HT:PCBM layers measured using an integrating sphere.

due to a combination of the small grating effect and light-confinement. We refrain from referring to the quantity "$1 - R_{\text{tot}} - T_{\text{tot}}$" for the uncoated grating as absorptance because the light is merely unaccounted for, not absorbed. This effect can also be seen when an absorbing layer is added to the sample. **Fig. 25**(b) shows that the 40 nm P3HT:PCBM grating sample has the exact same feature at 700 nm as the uncoated grating sample. P3HT:PCBM is transparent beyond 650 nm, so the unmeasured light past 650 nm does not increase the actual absorptance of the sample. Although not shown, this feature was also present in the measurements of the 15 nm, 40 nm, and 120 nm P3HT:PCBM grating samples as well. To obtain accurate absorptances of the coated grating samples, measurements of the uncoated gratings were subtracted from those of the coated grating samples, yielding the absorptances shown in **Fig. 22**(b). This modification of the measured data effectively eliminates the feature starting at 700 nm, where P3HT:PCBM is transparent, and does not receive an absorption enhancement from the confined light. However, the 8% of confined and unmeasured light below 650 nm will be

partially, if not mostly, absorbed by the solar cell active layer. Therefore, subtracting the unmeasured light from the sample measurements in regions where P3HT:PCBM is absorbing causes the absorptance when gratings are used to be underestimated. This is the main reason why the absorptances presented in **Fig. 23**(b) are lower when gratings are added, despite the initial measurements of $1 - R_{\text{tot}} - T_{\text{tot}}$ being ~8 percentage points greater when gratings are used. Despite decreasing the adjusted absorptance, the presence of this light-confinement is beneficial because it shows that a significant amount of light is propagating along the cell, where it would eventually be absorbed given a large enough cell area.

The fourth factor contributing to the reduced active layer absorptance is saturation. Due to the thickness of the P3HT:PCBM layer, the absorption saturates. The majority of the light in the organic layer is absorbed without the addition of a grating, leaving minimal capacity for enhancement. In the case of the 120 nm planar sample, 75% of the light is either reflected or absorbed, allowing for a possible absorption enhancement of only 25% by the addition of a grating. The 120 nm samples do see a slight absorption enhancement when diffraction gratings are added, but it is less than the amount subtracted due to increased reflectance, the small grating effect and light-confinement, yielding a net decrease in measured active layer absorption. The 40 nm samples are less saturated than the 120 nm samples, so their potential for absorption enhancement is greater, and there is less disparity in absorptance between the grating and planar samples. The 15 nm layers are not impacted from saturation and show equal amounts of absorptance between the grating and planar samples. In thin layers such as these, the weak absorber approximation can be used, where the absorptance is proportional to the path length of the light as in **(7)**. For all thin layers, the ratio of path lengths, and hence absorptances, between planar and grating samples is constant. Light lost through the small grating effect and light confinement is

also constant, so further reducing the active layer thickness would not cause the grating sample to appear to absorb more than the planar sample.

2.7.2 Efficiency Enhancement

To directly gauge the effect of surface texturing, we fabricated organic solar cells and measured their performance with and without diffraction gratings. The absorption analysis showed that the largest enhancement occurs for thinner active layers, and the difference in absorption between the 15 nm and 40 nm P3HT:PCBM layers was minimal. 45 nm P3HT:PCBM layers were used to achieve greater current and efficiency. A challenge in determining the enhancement was the variation in efficiencies from one cell to the next. The efficiency of a given solar cell would remain constant when measured multiple times, but the efficiency from one cell to the next varied by ±30%, which was more than the enhancement we expected to see. To mitigate this variation, we measured cells with linear gratings attached, then removed the gratings with tape and measured them again. A mosaic of six 8 mm × 8.3 mm linear gratings were used as shown in **Fig. 18**(e) and **Fig. 20**(b). Six gratings were used to reduce the small grating effect described above. Three separate slides were measured, each with four cells. The IV curves on a single slide were always similar, so their values were averaged.

The individual IV curves for each of the 12 cells with and without gratings, as well as the averaged IV curves for each slide are shown in **Fig. 26**. The averaged parameters for each slide are given in **Table 3**. The IV curves for the cells on a given slide vary much less than the curves between slides. The fill factor, open-circuit voltage, and shunt resistance are fairly constant across all the cells. The parameters that show the greatest change are the efficiency, short-circuit current, and series resistance. These variations were typical for our cells, and were caused by many factors during fabrication including variations in the ITO conductivity, active layer thickness, and film uniformity.

Table 3. Measured Solar Cell Electrical Parameters

	Efficiency	FF	V_{OC} [V]	I_{SC} [mA]	R_S [Ω]	R_{SH} [Ω]
Planar 1	0.69 ± 0.011%	58.7%	0.584	0.250	319	11,400
Grating 1	0.71 ± 0.007%	59.7%	0.593	0.252	303	12,500
Planar 2	0.45 ± 0.031%	55.0%	0.582	0.177	611	11,800
Grating 2	0.46 ± 0.014%	56.5%	0.584	0.173	513	13,900
Planar 3	0.42 ± 0.004%	57.4%	0.576	0.158	497	15,000
Grating 3	0.43 ± 0.017%	57.7%	0.585	0.159	487	12,100

The gratings provide a subtle, but consistent, improvement in efficiency. The efficiencies were enhanced by 3.9%, 0.8%, and 2.7% for slides 1, 2, and 3, respectively. These results are similar to the enhancements seen in the absorption analysis. For both analyses the enhancement from the grating is offset by the increased reflectance. The small grating effect has some contribution to the reduced enhancement, but this was smaller for the electrical measurements as multiple gratings were used. While the increased reflection is a key factor that needs to be considered when designing gratings for this configuration, it is not a fundamental limitation. Other researchers have demonstrated grating designs that reduce the reflectance of light incident on silicon and glass [73]–[75]. Antireflection coatings can also be applied to the gratings to further reduce their reflectance.

In addition to reducing the reflectance, the grating geometry can be further optimized to increase the diffraction efficiency. While an effort was made in the current work to maximize the diffraction efficiency, we were ultimately limited by the selection of available nanostructured molds. We have demonstrated that using available molds the increased absorption compensates for the increased reflectance. Fabricating custom nanoimprinting molds would allow for increased diffraction efficiency and reduced reflectance, leading to much greater efficiency enhancement.
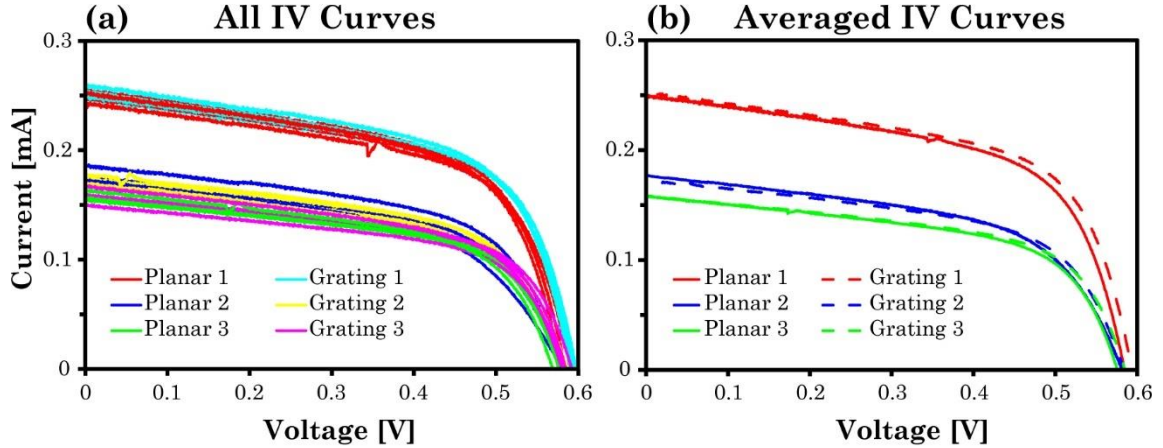
Fig. 26.   Solar cell IV curves. (a) IV curves for each of the 12 solar cells (four cells on each of three slides) with and without diffraction gratings. The cells on each slide are plotted in the same color. (b) Averaged IV curves for each slide with and without linear diffraction gratings.

2.8   Conclusions and Outlook

We have presented the tools and steps necessary for fabricating and characterizing a continuum of solar cell and diffraction grating geometries. Our PAN patterning procedure can be used to create arbitrary structures with features ranging from tens of nanometers to millimeters. As new optical materials and structures are explored, it is crucial that they be correctly characterized. Integrating spheres allow for the scattered and diffracted light leaving a sample to be directly measured. Such measurements can be combined with measurements from a standard UV-Vis spectrophotometer to isolate the diffuse and specular components. Integrating spheres also allow for accurate measurements of the absorptance of scattering samples.

We have modeled and fabricated modular diffraction gratings that may be applied to any system requiring light harvesting. By measuring the spectral absorption enhancement as well as solar cell electrical characteristics, we were able to identify the enhancement gained from increasing the optical path length as well as factors reducing the performance. While our devices were limited by the small grating sizes and reflectance of the gratings, this approach is still promising. The small grating effect will be mitigated when larger

textured panels are used. Further optimization of the grating geometry would yield enhanced diffraction efficiency and reduced reflectance, even below that of a planar surface. There are many grating parameters not considered here that can lead to further enhancement, such as grating blazing, shape, and material. Simple enhancement methods, such as the ones presented in this work, with optimal parameters may be the tool kit needed to construct the next generation of solar cells.

Chapter 3

SURFACE-ENHANCED TWO-PHOTON EXCITATION

3.1 Introduction

Cellular and sub-cellular microscopy are essential analysis methods for understanding how biological systems function and respond to external stimuli. Fluorescence microscopy is an especially effective analytical method for evaluating cellular structure and behavior [76], [77], gene expression [78], protein function [79], diseased cells [80], and drug and toxin distribution [81], [82]. For these applications the probing mechanism should ideally be nondestructive and have a large analytical penetration depth. Unfortunately, many fluorescence techniques suffer from high source powers, shallow depths of analyses, or low signal-to-noise ratios (SNR).

Fluorescence imaging of cells is conducted by labeling parts of cells with fluorescent proteins (FPs) or other fluorescent probes, followed by illuminating the cells and detecting the fluorescent signal. The use of fluorescent markers allows scattered and reflected light from the source (noise) to be eliminated with dichroic filters, thereby greatly enhancing the SNR [83]. There are a multitude of fluorophores with different absorption and emission spectra that are designed to stain parts of cells (e.g., dyes), or to be directly expressed by the cells under certain conditions (e.g., FPs) [84].

While fluorescence microscopy enables the detection of cells and even single molecules within cells, it is not without its limitations. Scattering, in both single-photon and multiphoton excitation fluorescence, significantly limits the SNR associated with imaging through tissue [85], [86]. Illuminating light that is scattered away from the fluorophores, and emitted light that is scattered away from the detector, reduce the signal on the detector. Furthermore, emitted light that is scattered towards neighboring detector pixels increases the noise. Scattering from small particles (Rayleigh

scattering), the intensity of which scales with λ^{-4}, is much more prevalent at shorter wavelengths [87]. In addition, index variations in cellular structures result in the refraction of transmitted light. Both scattering types lead to a large background signal and appreciable blurring of fluorescent images.

Confocal microscopy was developed to reduce the influences of such scattering [88]. In confocal microscopy, a point source of light and a detector are used in the same imaging system, ensuring that only light located at the focal point of the microscope is utilized in the image. A 2D or 3D image is then generated by scanning the focal point across the specimen [89], [90]. The illumination system produces a point source that is imaged through the microscope onto the object. An aperture at the detector blocks scattered excitation and fluorescent light, albeit at the cost of lower signal intensity. The reduction in signal from the reduced source size and detector aperture also make confocal microscopy more susceptible to absorption effects, which further reduce the signal intensity.

Absorption in hemoglobin and melanin is appreciable at wavelengths below 700 nm, and absorption in water is appreciable above 900 nm. Such absorption, along with reduced scattering at longer wavelengths, defines a near-infrared 'window' (between 700 and 900 nm) where light has a relatively deep penetration depth [86], [91]. Microscopy techniques that use visible FPs are only able to penetrate to depths of microns to millimeters, whereas techniques that utilize NIR FPs can achieve penetration depths on the order of centimeters [86], [92]. Numerous NIR FPs have been developed to take advantage of this spectral 'window.' However, scattering in the NIR, while less intense than in the visible, continues to significantly limit spatial resolution and penetration depth.

Two-photon excitation microscopy (2PEM) can allow for increased SNR and z-resolution by exploiting the nonlinear dependence of absorption on the applied electric field. In 2PEM, a focused NIR beam is used to excite a FP that then emits a blueshifted signal via two-photon excitation fluorescence (2PEF).

2PEF is a nonlinear process with a quadratic dependence on the excitation intensity. The intensity of unfocused light present in such analyses is insufficient to create a significant amount of fluorescence, which restricts the majority of the fluorescent signal to the focal region of the illuminating beam, resulting in a greater local emission and enhanced spatial resolution [85], [90], [93]. The two-photon absorption peak wavelength is generally twice that of the single-photon absorption peak wavelength, making it easier to filter out scattered light from the source, because the emitted light is generally hundreds of nanometers away from the source (compared to tens of nanometers for single-photon fluorescence) [84], [94], [95]. In addition, 2PEM systems are only minimally affected by scattering and autofluorescence of surrounding tissue, because only the fluorescent signal originating from the focal region of the incident beam is utilized in the image. It is assumed that all photons reaching the detector originate from the focal spot, regardless of whether they were scattered. This enables a large aperture and detection region to be used and reduces the power requirement of the source and the associated damage to tissue [90].

Another method for enhancing the fluorescent SNR is through the use of plasmonics. Photons can couple into the plasmonic modes of materials, which gives rise to enhanced electric fields at interfaces [96], [97]. FPs adjacent to such interfaces experience greater fields and exhibit increased fluorescence [98]. The plasmonic resonance of a given material can be enhanced and tuned to match the absorption bands of FPs by adjusting the surface morphology [99]–[102]. The surface plasmon resonance for most metals is located at wavelengths in the UV or visible range, but can be shifted by using particles or structures with sizes on the scale of the plasmon wavelength [102]–[104]. Additional control over the shape and peak wavelength of resonances can be achieved by creating periodic trenches that allow light to couple into associated cavity modes [101], [105], [106].

Plasmonics and 2PEM have an excellent synergy [107]–[109]. The field enhancement from plasmonic structures combines with the quadratic dependence of 2PEM to produce an even greater fluorescent signal. The ultrafast response of plasmonic excitations allows optical signals to be manipulated on femtosecond time scales. Moreover, localized surface enhancement of the *E*-field allows nonlinear effects to be utilized at reduced optical power, thereby lowering the potential for damage to samples.

While previous works have shown how plasmonics can be used to enhance 2PEF, often using 0.3–1 W Ti:Sapphire or Nd:YAG lasers, they have not taken advantage of the potential reduction in power afforded by the union of these techniques [110]. Furthermore, many of the previous studies utilize structures that are largely randomized, making them ineffective at tuning the plasmonic resonance over a wide range of wavelengths [100], [108], [109].

In this work, we demonstrate a low-power (30 mW) spectrally tuned plasmonic multiphoton (MP) fluorescence platform for rapid and accurate measurements of fluorescent probes. Our system uses a MP microscope to view 2PEF and three-photon excitation fluorescence (3PEF) from samples deposited on a plasmonically-enhanced substrate. The substrate surface structure was designed for localized surface enhancement tuned to the 1040 nm wavelength of the pulsed fiber laser present in our MP microscope. Such enhanced fields facilitate 2PEF of appreciably stronger intensity from dyes located on the plasmonic substrate. The plasmonic substrates are easily fabricated and can be tuned so their resonances match any laser source.

To demonstrate the versatility of the testbed, three fluorescent materials used in biological imaging were examined: rhodamine 6G (R6G), a green fluorescent protein (GFP, bfloGFPa1), and chlorophyll. R6G is a highly-fluorescent dye used to stain and image a wide variety of samples. R6G possesses absorption and emission peaks centered at 530 nm and 550 nm, respectively. GFP is a common protein used as a biological marker and the strain used in the present case has been reported to exhibit particularly

intense fluorescence at a wavelength of 516 nm upon stimulation at 500 nm [111]. The third fluorophore, chlorophyll, is present in nearly all plants and is responsible for absorbing sunlight. Chlorophyll has two absorption peaks, one located at 430 nm and another at 660 nm, and exhibits fluorescent emission at 685 nm. Although the absorption peaks of chlorophyll do not coincide with the source half-wavelength used in this work (520 nm), chlorophyll does exhibit intense fluorescence upon illumination at wavelengths below 685 nm. All three fluorophores exhibited 2PEF when illuminated with 1040 nm light from the laser source of the MP microscope.

3.2 Multiphoton Microscopy

Multiphoton microscopy (MPM) is a powerful technique that enables simultaneous observation of several different nonlinear optical responses, such as second harmonic generation (SHG), third harmonic generation (THG), and two- or three-photon excitation fluorescence due to MP absorption. The high resolution, deeper penetration, non-invasiveness, and fast acquisition time, together with simultaneous multichannel detection, make MPM a highly-attractive and robust tool for three-dimensional characterization of a wide variety of samples [112]–[114]. Furthermore, MPM allows for analyses of nano-scale features on large-scale (10 cm × 10 cm) samples. While other MP microscopes generally use high powered Ti:sapphire lasers, which are bulky and can be prohibitively expensive for a number of applications, our MPM system employs a much more compact and lower-cost pulsed fiber laser. So far, we have successfully coupled our MP microscope with a compact 1550 nm femtosecond fiber laser to generate high resolution 3D images of various biological samples [112], to study the optical properties of single and few-layer graphene [113], to measure the third order nonlinear response of TiO_2 with different thicknesses [115], and to estimate the Pockels coefficient (r_{33}) of electro-optic polymer films from the detected second-harmonic signal [114].
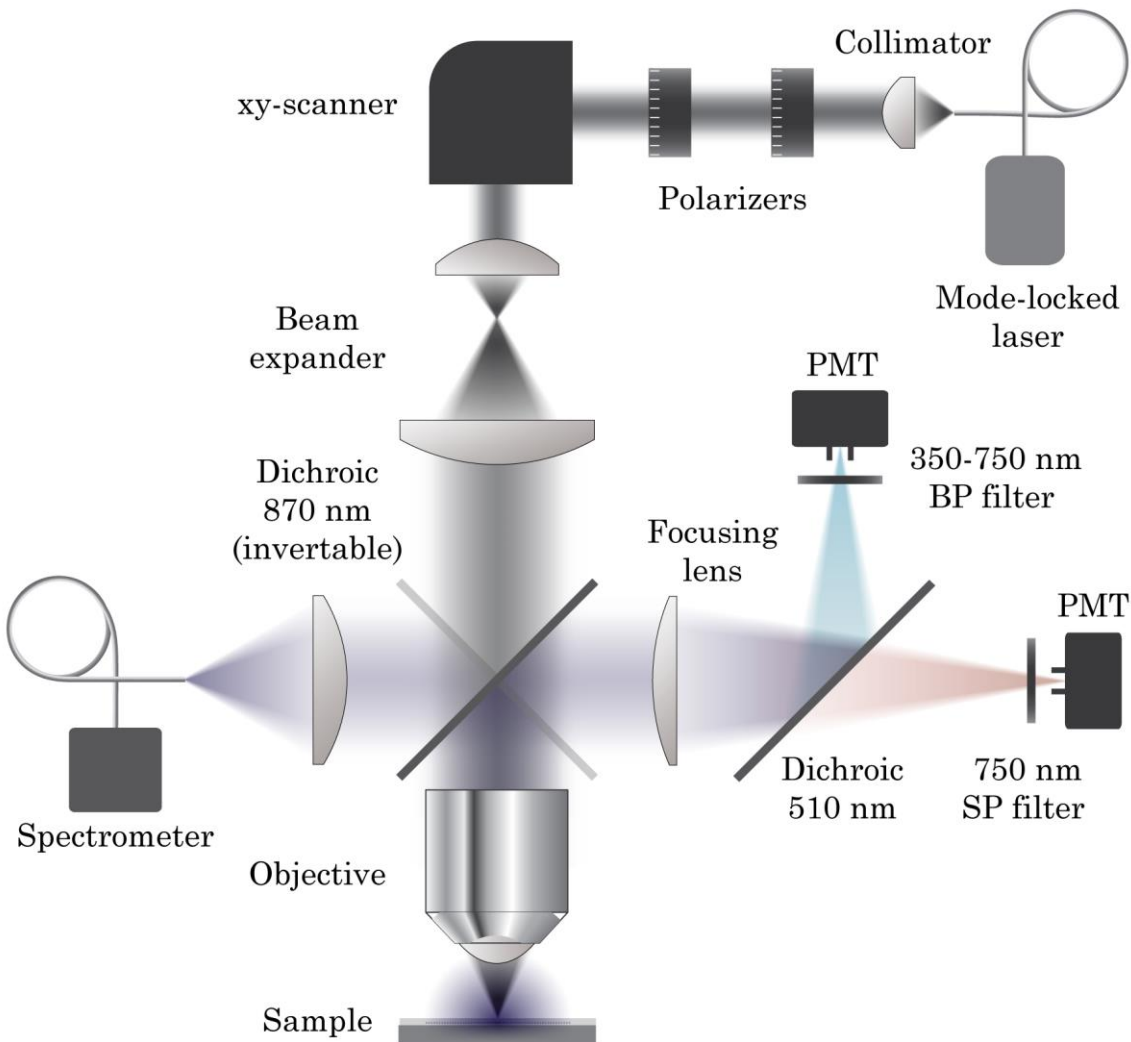
Fig. 27. Multiphoton microscope used for 2PEM. See text for description.

A schematic illustration of our custom-made MPM system is shown in **Fig. 27**. The excitation source was a compact femtosecond fiber laser mode-locked by a carbon-nanotube saturable absorber (K-Photonics, LLC) with an output wavelength of 1040 nm. The output had a repetition rate of 8 MHz with pulses of 150 fs full-width half-max (FWHM). The laser beam was first collimated and then raster-scanned using galvo mirrors. Two achromatic doublet lenses expanded the beam cross-sectional area by a factor of 4 in order to fill the back aperture of the objective lens. The beam passed through a dichroic mirror at 870 nm followed by a 20×, 0.5 numerical aperture, aspheric

lens and focused into a tight spot (1.4 µm diameter) on the sample, at which the average power was measured to be about 30 mW. Light from SHG (λ = 520 nm), THG (λ = 347 nm), 2PEF (λ > 520 nm), and 3PEF (λ > 347 nm), was collected and collimated by the objective. The MP beam was reflected off of the 870 nm dichroic and passed through a focusing lens. The converging beam was spectrally split by a dichroic mirror at 510 nm to isolate light from THG and some of the light from 3PEF. The light was filtered further after passing through a 350–750 nm bandpass filter in the reflection arm, and a 750 nm shortpass filter in the transmission arm, before focusing on one of two photomultiplier tubes in a non-descanned detection scheme. The field of view of the image was 250 µm × 250 µm, (512 × 512 pixels) captured at 0.5 frames/second. To measure the 2PEF spectrum, the 870 nm dichroic mirror was flipped to direct light towards an Ocean Optics QE65000 HighSensitivity spectrometer. All measurements except for power curves were obtained using unpolarized light.

To obtain a measurement of the 2PEF signal versus incident power, two rotatable linear polarizers were added before the *xy*-scanner. The power reaching the sample was then adjusted by rotating the up-stream polarizer. Because the structures were polarization sensitive (see below), the samples were oriented to yield the greatest signal.

Power curves are effective in determining whether the signal is created by single-photon, 2PEF, or 3PEF. This is especially useful for chlorophyll, where the absorption spectrum extends from blue light (3PEF) to green light (2PEF). Once the power curve is obtained, the polynomial relationship between input and output signals reveals itself as the slope, *q*, of the logarithm of the data as shown in **(18)**.

$$\log(\text{2PEF signal}) = q \cdot \log(\text{laser power}) \qquad \textbf{(18)}$$

3.3 Simulation and Design

We wished to develop simple substrates that would enhance the intensity of the electric field near the FP/substrate interface when illuminated by a laser source. The substrate needed to be robust and easy to fabricate with an ability to vary key structural parameters, which led us to consider a metallic grating. Metallic gratings can be easily created, via mask or interference-based lithography, and possess properties that can be readily modeled using FDTD analysis methods.

Plasmonic structures were simulated using Lumerical FDTD Solutions software. The structures examined were metallic linear gratings used in vacuum, with linear gratings chosen because of their ease of fabrication. Gratings with different cross-sectional shapes (e.g. triangles, sinusoids, and square waves) were initially examined, but it was soon discovered that the choice of such shapes had minimal impact on the resonance behavior. Square wave structures were then chosen because they could be reliably and simply fabricated using lithography. **Fig. 28** reveals the substrate structure and associated parameters. The textures were modeled using a 2D cross section comprising one period of the grating. The left and right boundaries were set as periodic to simulate a linear grating of infinite extent. The top and bottom boundaries were set as perfectly-matched layers absorbing all incident light. A plane wave of *p*-polarization originating above the substrate surface was applied downward onto the substrate. A wave with *s*-polarization was not considered, because such a wave would have little interaction with the linear gratings considered, and because the simulation was conducted with the primary aim of identifying and optimizing plasmonic modes. Furthermore, if the source used for measurements is polarized then the polarization may be rotated to the desired state. The plasmonic resonance of the substrate structures was measured using a reflectance monitor located above the source. Cavity modes cause the surface to become absorbing near resonance, so dips in
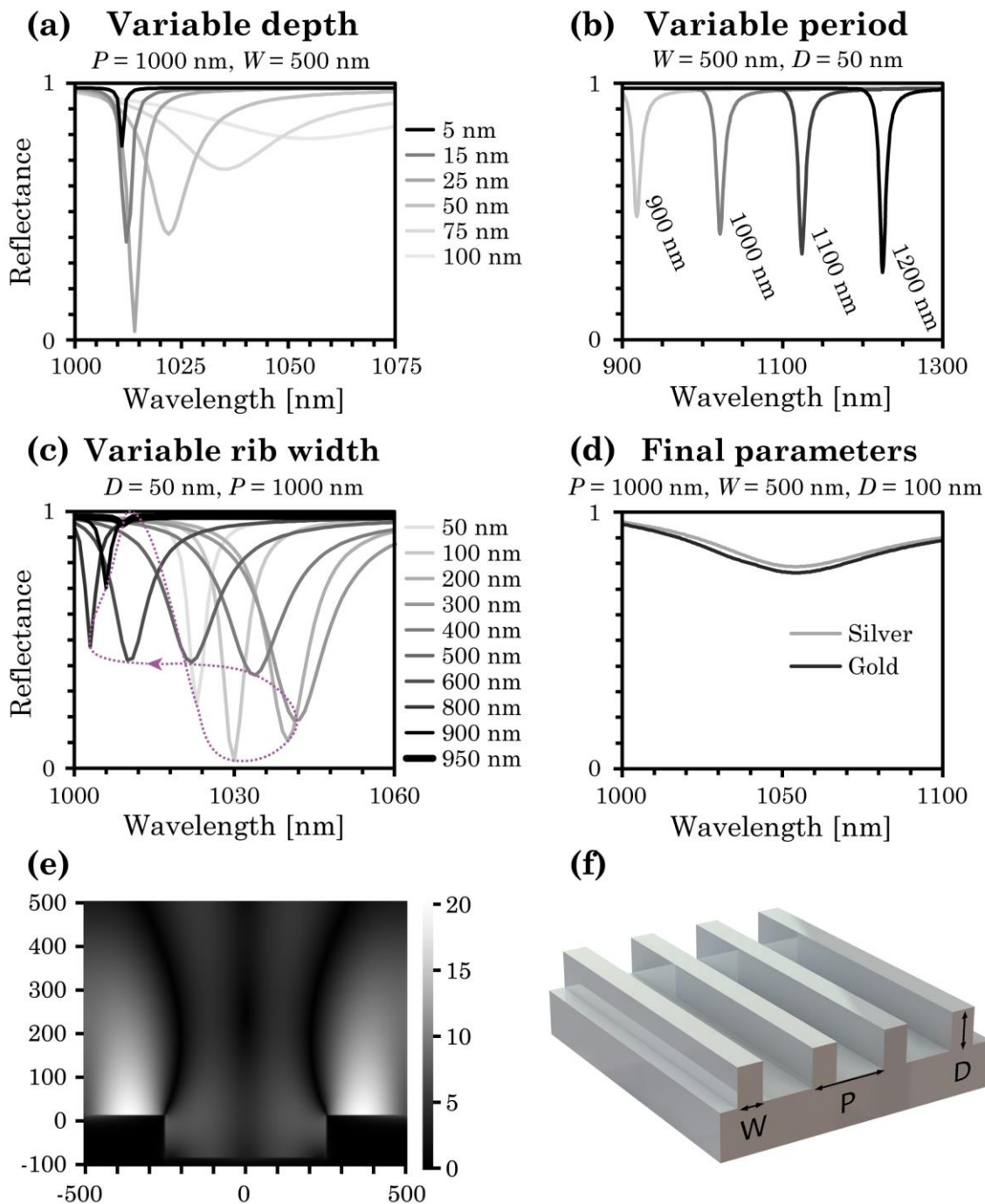
Fig. 28. Plasmonic response for with various structures. (a)–(c) Simulated reflectance spectra obtained from varying the structure depth, period, and rib width, respectively. The dotted line in (c) indicates the figure-eight pattern that the reflectance minimum traverses as the rib width is adjusted from 0 to P. (b) and (c) use a fixed depth of 50 nm, instead of the final depth of 100 nm, because the shallower depth yields narrower resonances that clearly depict the nature of the varying parameters. (d) Plot of reflectance with final structure parameters for silver and gold. (e) Intensity profile surrounding one period of the structure. The intensity values were scaled so that the maximum intensity from light incident on planar silver was 1. (f) Diagram of the structure with labeled optimization parameters.

the reflectance are good indications of the width and amplitude of such resonances. Structure parameters were adjusted to tune and optimize the plasmonic resonance.

Altering the period, depth, and width of the structures changed the wavelength, FWHM, and amplitude of the resonance peak in a similar manner as to that previously reported [101], [105], [106], [116], [117]. **Fig. 28**(a)–(c) reveal how the structural parameters affected the resonance. The center wavelength of the cavity mode was most effectively adjusted by altering the period, with the resonance peak roughly matching the period. For a given period, the depth could be adjusted to tune the amplitude and FWHM of the resonance and, to a lesser degree, the peak wavelength [105]. Adjusting the rib width from 0 to P caused the reflectance minimum to traverse a figure-eight pattern, as indicated by the dashed line in **Fig. 28**(c).

The texture parameters were iteratively adjusted to achieve a resonance at 1040 nm with a desired amplitude and FWHM. **Fig. 28**(d) and (e) show the performance of the structure with the final design parameters. There was a trade-off between the FWHM and the resonance amplitude; that is, a larger amplitude yielded a smaller FWHM value. This trade-off (low FWHM at high amplitude) was well-suited for these devices, which are intended to operate within a narrow bandwidth. The resonance peak wavelength is dependent on the refractive index of the surrounding medium. Our structures were designed with vacuum as the surrounding medium, as they were intended to be used in air with thin layers of fluorophores (<100 nm). (Note: structures that are intended to be used while covered with cells or submerged in water or other solutions should have the appropriate period, width, and depth.) The final grating parameters utilized were as follows: period = 1000 nm, depth = 100 nm, and rib width = 500 nm. These parameters produced a large E-field enhancement while maintaining a reasonable bandwidth that allowed for some accommodation of fabrication errors. The structures were modeled as being comprised of either silver or gold. Because both metals were found to exhibit

nearly identical performance, as shown in **Fig. 28**(d), silver was selected as the lower cost option. **Fig. 28**(e) reveals a cross section of the modeled E-field intensity surrounding these structures; the E-field intensity in the vicinity of the structured surfaces was a factor of 20 greater than for planar (non-structured) substrates. Because 2PEF is proportional to the square of the E-field intensity, an intensity enhancement of 20 corresponds to a 2PEF enhancement of 400 over that of planar substrates. To reduce computational time, the structures were modeled as bulk silver, whereas the fabricated structures described below were etched into silicon and coated with 100 nm of silver. However, simulation results from structures with bulk silver and silver-coated silicon exhibited negligible difference.

3.4 Fabrication

3.4.1 Green Fluorescent Protein bfloGFPal Preparation

A histidine-tagged construct, pET28a:bfloGFPa1-His, was provided as a gift by the Air Force Research Laboratory (Dr. Nancy Kelley-Loughnane). The construct was transformed into BL21(DE) pLysS-T1R competent *E. coli* cells (Sigma-Aldrich, St. Louis, MO, USA) by heat shock. The transformed cells were then incubated with LB medium and shaken at 225 rpm at 37 °C for 1 h. The cell suspension (100 µl) was deposited onto a LB agar plate containing 5 µg/ml chloramphenicol (Sigma-Aldrich, St. Louis, MO, USA) and 50 µg/ml kanamycin (Sigma-Aldrich, St. Louis, MO, USA). The plate was then incubated at 37 °C overnight.

Expression and isolation of bfloGFPa1 were performed following the general procedure described by Bomati, et al. [111] with a few modifications. Briefly, 10 well-isolated colonies were picked from the LB agar plate prepared above and cultured first in 5 ml LB medium for 16 h and then in 2 liter LB medium until OD600 reached 0.8. After adding 0.5 mM isopropylß-D-1-thiogalactopyranoside (Sigma-Aldrich, St. Louis, MO, USA) to the medium, the cells were grown for another 4 h. The cells were then harvested, lysed with

sonication in a lysis buffer (50 mM tris-HCl, at pH 8 containing 400 mM NaCl, 10 vol% glycerol, 10 mM β-mercaptoethanol, and 0.5 mg/ml lysozyme), and centrifuged at 4500 g for 5 min. The supernatant was subjected to Ni_2+-NTA agarose chromatography. The column was first washed with a wash buffer (50 mM Tris-HCl, pH 8, containing 400 mM NaCl, 10 mM β-mercaptoethanol, and 20 mM imidazole) followed by elution with 50 ml of a buffer (50 mM Tris-HCl, pH 8, containing 400 mM NaCl, 10 mM ß-mercaptoethanol, and 250 mM imidazole). The eluate, comprised of the bfloGFPa1 protein in elution buffer, was collected and enriched to a desired concentration with 20 ml of Spin-X UF concentrators (Corning, Inc., Corning, NY, USA).

3.4.2 Chlorophyll Preparation

Chlorophyll was extracted from spinach by soaking 8 g of spinach in 30 ml of isopropanol. The mixture was stirred every 10 minutes until the liquid appeared green from the dissolved chlorophyll (a total time of approximately 1 h). The leaves were removed and the liquid was poured through filter paper to yield a foggy green solution. The solution was then syringed through a 1 µm nylon filter, after which it appeared clear and emerald green in color.

3.4.3 Plasmonic Structures

Silicon wafers were used as the starting material for the grating substrates. After applying a Shipley S1805 photoresist by spin coating, the coated wafers were placed into a Lloyd's mirror interferometer setup as shown in **Fig. 29**(a). The setup was composed of a He-Cd laser of 442 nm wavelength that was spatially filtered and collimated onto the Lloyd's mirror. A shutter was used to control the exposure time. A grating period of 1000 nm was achieved by controlling the rotation stage angle. The photoresist was exposed with an interference pattern created by the collimated beam and the reflected beam. The exposed grating sample was then etched to a depth of 100 nm by reactive ion etching (RIE) using an Oxford Plasma 100 RIE system and an O2-CF4 gas mixture. After etching, the remaining photoresist was removed by dissolution
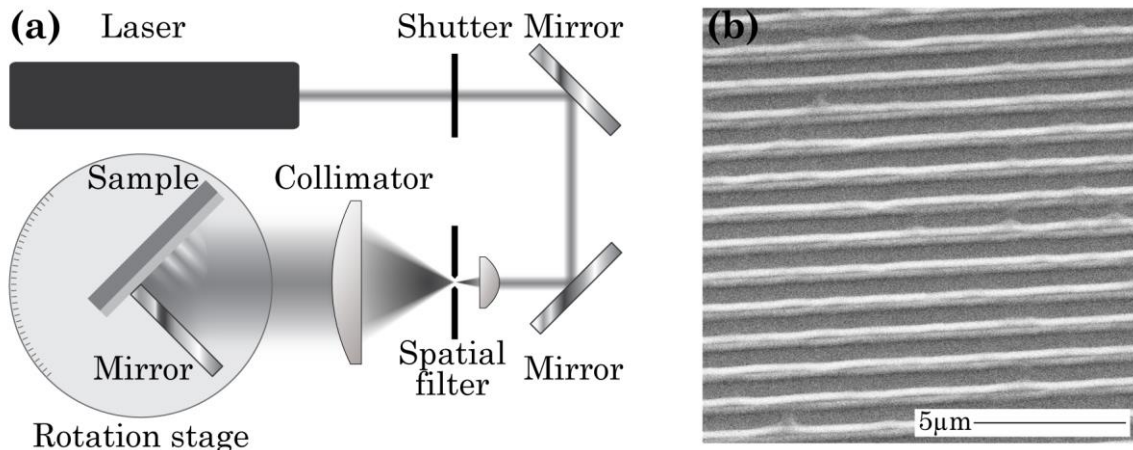
Fig. 29. Lloyd's Mirror interferometer setup used to expose the grating structure (a), and a SEM image of a grating fabricated on silicon (b).

in acetone and the substrate was cleaned with isopropyl alcohol. **Fig. 29**(b) shows a scanning electron microscope (SEM) image of the Si grating. The walls were straight and smooth. The average grating period associated with ten ribs was measured to be 1036 nm, which was an excellent agreement with the target of 1000 nm. Finally, 100 nm of silver was deposited by thermal evaporation onto the gratings.

3.4.4 Fluorophore Deposition on Plastic Substrates

R6G was suspended in a polymer film to prevent aggregation and quenching on the metallic surface. The R6G-doped polymer film was prepared by mixing a solution of 1 mM of R6G in ethanol with a solution of 2 wt% poly(methyl methacrylate) (PMMA, 950 k) in anisole. The doped solution was spincast onto the substrate and then baked to achieve a thickness of ~70 nm.

Chlorophyll was applied in a similar fashion as R6G. 0.5 ml of the chlorophyll in isopropanol solution was added to a 3 ml solution of 2 wt% PMMA in anisole, and spincast onto the substrate and then baked as mentioned above.

The GFP solution was simply spincast directly onto the plasmonic substrate at 3000 RPM without thermal treatment.
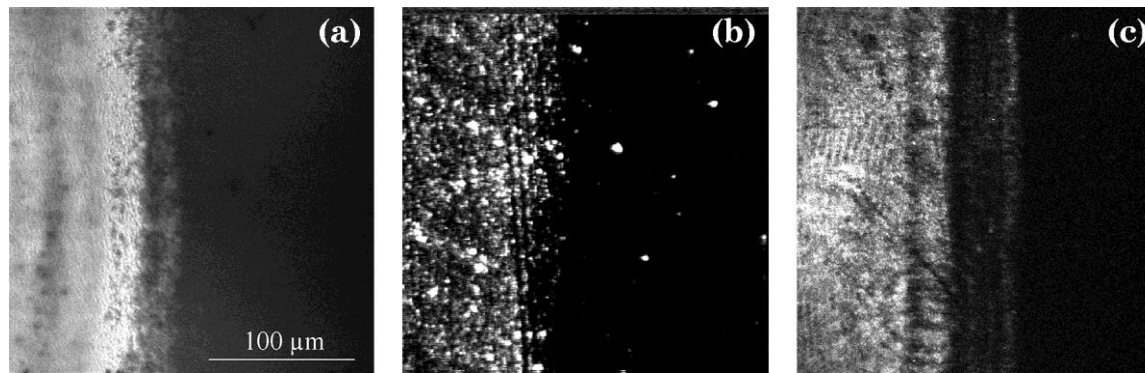
Fig. 30. MPM images of the boundaries between textured (left) and planar (right) substrates coated with R6G (a), green fluorescent protein (b), and chlorophyll (c).

3.5 Results and Discussion

Fig. 30 reveals images taken using the MP microscope. The images correspond to the z-position closest to the surface of the film, where the beam intensity and 2PEF signals were the greatest. Each image was taken at the boundary between the textured (left) and planar (right) regions to make the enhanced signal more visible and to mitigate errors caused by power fluctuations in the laser and spatial variations in the substrate texture and/or in the film composition. **Fig. 31** shows the fluorescence signal and the associated enhancement for each substrate texture, fluorophore, and z-position. The signal for each material was calculated at every z-position by averaging the values of all pixels located 20 µm to the left of the boundary and to the right of the boundary for the textured and planar regions, respectively. The enhancement at each z-position was then calculated by taking the ratio of the textured to planar signals.

The textured regions were clearly distinguishable from the planar regions due to the enhanced 2PEF associated with the former regions. GFP-bearing substrates exhibited the greatest enhancement (50×), followed by chlorophyll-bearing substrates (8×), and then R6G-bearing substrates (4×). The enhancement of all three samples dropped off as the beam defocused and the intensity reduced. Plasmonic enhancement in this case is a linear process (the field enhancement factor does not depend on the incident intensity) and

Fluorescence Signal [a. u.]

Enhancement

(a) GFP

(b) GFP

(c) Chlorophyll

(d) Chlorophyll

(e) R6G

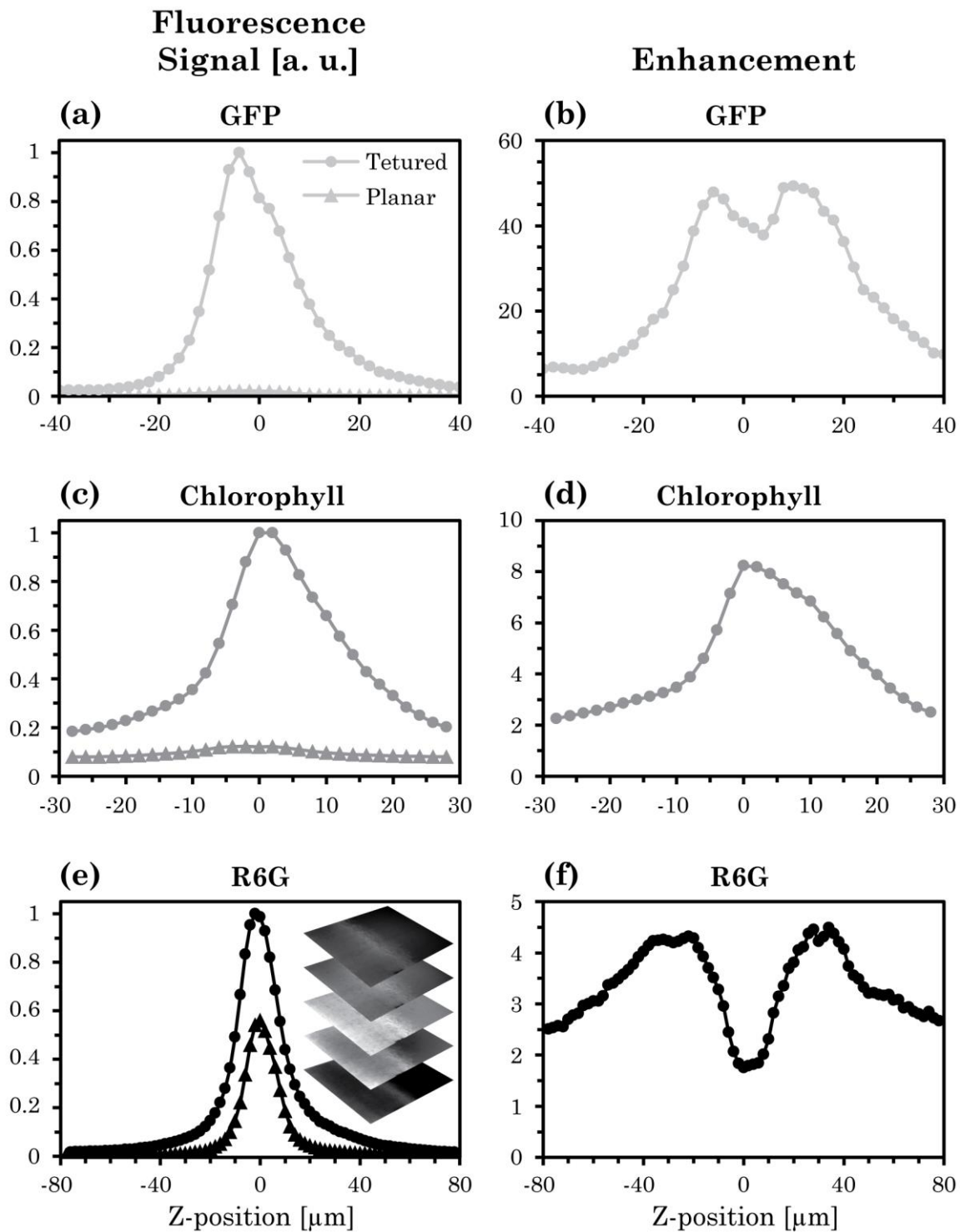**(f)** R6G

Z-position [μm]

Z-position [μm]

Fig. 31. Fluorescence signals (left column) and enhancements (right column) calculated from the MP microscope measurements. The inset shows five images of the R6G sample at different focus positions.

therefore should produce a constant 2PEF enhancement regardless of the input intensity. The enhancement reduction was caused by noise, which was proportionally more prominent at lower intensities. This caused the enhancement to approach unity as the incident intensity decreased.

The R6G-bearing substrates exhibited the greatest enhancement when the surface was 30 µm above or below the focus of the beam, and the laser intensity was reduced. When the surface was at the focus of the laser the enhancement reduced to (2×). We believe photobleaching was the cause of the reduced enhancement in the R6G-bearing substrates, and to a lesser degree, the GFP-bearing substrates. The rate at which photobleaching occurs increases with the intensity of the incident light [118]. Because the textured part of the sample produced an increased field, photobleaching reduced the signal of the textured part of the sample more rapidly than the planar part, thereby reducing the enhancement. Photobleaching was also observed while viewing the R6G samples: when the laser was focused on the surface, repeated scans of the same sample area gradually darkened.

To confirm that the fluorescent signals measured with the MPM were from 2PEF, as opposed to SHG, the spectrum of R6G on textured silver was measured. SHG, if present, would reveal itself as a narrow peak at half of the source wavelength (520 nm). **Fig. 32**(a) reveals that SHG was not present and the signal is entirely created by 2PEF, as was expected.

The excitation band for chlorophyll extends from blue to red wavelengths, making it possible for 3PEF to dominate instead of 2PEF. To understand the nature of the fluorescence, the signal was measured for various laser powers for R6G and chlorophyll on textured substrates and is shown in **Fig. 32**(b). 2PEF should have a quadratic form, and 3PEF should have a cubic form. The slope of the data after taking the logarithm of the input power and 2PEF signals was 1.97 ± 0.12 for R6G and 1.86 ± 0.14 for chlorophyll, which, given the error of the measurements, confirmed the presence of 2PEF and relative absence of 3PEF.
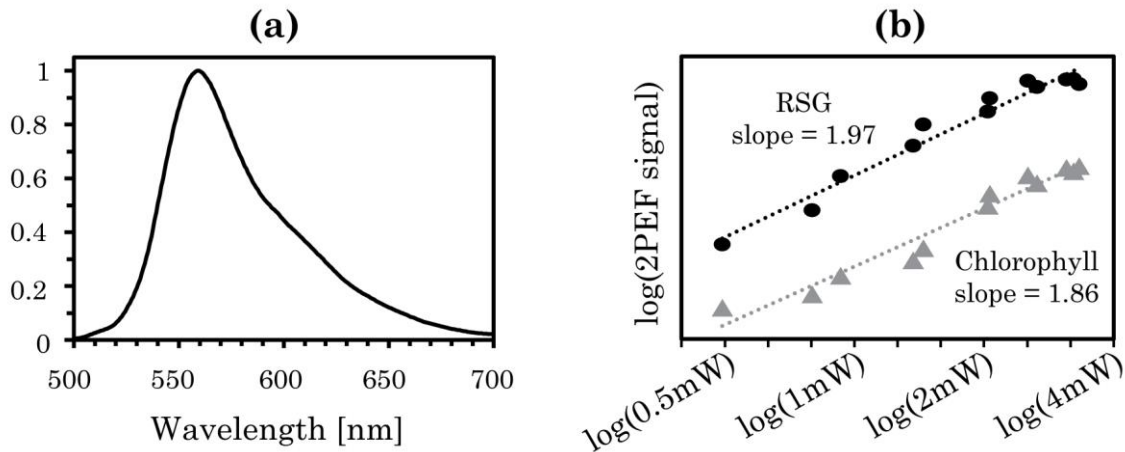
Fig. 32. 2PEF spectrum and power response. (a) 2PEF spectrum of R6G on a textured substrate. The spectrum closely matched a typical R6G emission spectrum. SHG at 520 nm was not present. (b) Logarithm of 2PEF signal versus incident laser power for R6G and chlorophyll on textured substrates. The slope of both datasets was close to 2, confirming that the signal observed was quadratic and due to 2PEF.

3.6 Conclusion

We have successfully demonstrated a platform for imaging and detection of biological samples labeled with fluorescent dyes. The plasmonic substrates that were designed for a narrow source bandwidth exhibited a stark 2PEF signal enhancement over planar substrates. This was the case for a green fluorescent protein, chlorophyll, and rhodamine 6G, all of which were chosen to illustrate the ability of our platform to image diverse samples with minimal incident radiation. Other dyes, quantum dots, or autofluorescent materials would likely be equally as effective [119]. While this approach is limited to imaging fluorophores within 0.5 µm of the plasmonic surface, it has potential for use with sub-micron microorganisms. Any sub-micron specimen that can be grown or placed near the plasmonic surface will receive a significant fluorescence enhancement. Further enhancement of the fluorescent signal may be achieved by designing structures that have narrower but greater enhancement peaks, which can be used in conjunction with sources within the resonance bandwidth.

CONCLUSION

Nearly all devices that utilize light would benefit from the ability to collect more of it, regardless of whether the photons are being used as transporters of energy or information. For solar panels, collecting more photons results in greater energy production. For imaging and data transfer, collecting more photons results in clearer information. In the event that there is a surplus of light, researchers are quick to find other uses for the excess; it can be used to reduce noise, perform spectral analyses, isolate polarization effects, increase scanning speeds, or illuminate larger areas.

We have demonstrated three ways in which surface texturing can be used to increase the amount of collected light: by using scattering structures to redirect light so that it propagates laterally through windows toward solar cells, by using diffraction gratings to increase the path length of light in solar cell layers, and by using plasmonic structures to enhance two-photon excitation fluorescence from biological markers. The first two examples use the collected light to generate electricity, which is always in demand. The third example, biological imaging, is one of the few examples where too much light is undesirable, as it can damage the structures being imaged. This sets a limit on the intensity of the incident light. Surface texturing addresses this by increasing the fluorescent signal without changing the intensity of the incident beam.

Regardless of the specific application they are tailored to, surface structures work in the same ways: they allow for control over the optical properties of interfaces. This adds a fourth dimension to optical design. Surface textures allow us to manipulate wavefronts without taking up additional space or requiring additional lenses or mirrors. They can be used to improve the simplest of optical systems, such as windows, or advanced systems, such as multiphoton microscopes. Surface structuring presents a variety of enhancements for all types of optical systems.

References

[1] M. E. R, "Monthly Energy Review - March 2015," 2015.

[2] "Commercial Buildings Energy Consumption Survey," 2003.

[3] "Residential Energy Consumption Survey," 2009.

[4] K. V Wong and R. Chan, "Smart Glass and Its Potential in Energy Savings," *J. Energy Resour. Technol.*, vol. 136, no. 1, p. 012002, 2013.

[5] V. Devabhaktuni, M. Alam, S. Shekara Sreenadh Reddy Depuru, R. C. Green, D. Nims, and C. Near, "Solar Energy: Trends and Enabling Technologies," *Renew. Sustain. Energy Rev.*, vol. 19, pp. 555–564, 2013.

[6] I. Cerón, E. Caamaño-Martín, and F. J. Neila, "'State-of-the-art' of building integrated photovoltaic products," *Renew. Energy*, vol. 58, no. 0, pp. 127–133, 2013.

[7] "Sage Glass," 2014. [Online]. Available: sageglass.com.

[8] J. L. H. Chau, R. T. Chen, G. L. Hwang, P. Y. Tsai, and C. C. Lin, "Transparent solar cell window module," *Sol. Energy Mater. Sol. Cells*, vol. 94, no. 3, pp. 588–591, Mar. 2010.

[9] Y. Zhao, G. A. Meek, B. G. Levine, and R. R. Lunt, "Near-infrared harvesting transparent luminescent solar concentrators," *Adv. Opt. Mater.*, vol. 2, no. 7, pp. 606–611, 2014.

[10] R. Alghamedi, M. Vasiliev, M. Nur-E-Alam, and K. Alameh, "Spectrally-selective all-inorganic scattering luminophores for solar energy-harvesting clear glass windows," *Sci. Rep.*, vol. 4, p. 6632, 2014.

[11] C. S. Erickson, L. R. Bradshaw, S. McDowall, J. D. Gilbertson, D. R. Gamelin, D. L. Patrick, S. and<p> G. McDowall John D., D. R. Gamelin, and D. L. Patrick, "Zero-Reabsorption Doped-Nanocrystal Luminescent Solar Concentrators," *ACS Nano*, vol. 8, no. 4, pp. 3461–3467, Apr. 2014.

[12] R. R. Lunt and V. Bulovic, "Transparent, near-infrared organic photovoltaic solar cells for window and energy-scavenging applications," *Appl. Phys. Lett.*, vol. 98, no. 11, pp. 3–5, 2011.

[13] C.-C. Chen, L. Dou, R. Zhu, C.-H. Chung, T.-B. Song, Y. B. Zheng, and C. E. T. Al, "Visibly Transparent Polymer Solar Cells Produced by Solution Processing," *ACS Nano*, vol. 6, no. Xx, p. 120712084458005, 2012.

[14] C. Bechinger, "Development of a new self-powered electrochromic device for light modulation without external power supply," *Sol. Energy Mater. Sol. Cells*, vol. 54, no. 1–4, pp. 405–410, 1998.

[15] A. Hauch, A. Georg, S. Baumgärtner, U. Opara Krašovec, and B. Orel, "New Photoelectrochromic Device," *Electrochim. Acta*, vol. 46, no. 13–14, pp. 2131–2136, 2001.

[16] W. Gao, S. . Lee, J. Bullock, Y. Xu, D. . Benson, S. Morrison, and H. . Branz, "First a-SiC:H photovoltaic-powered monolithic tandem electrochromic smart window device," *Sol. Energy Mater. Sol. Cells*, vol. 59, no. 3, pp. 243–254, 1999.

[17] C. G. Granqvist, E. Avendaño, and A. Azens, "Electrochromic coatings and devices: Survey of some recent advances," *Thin Solid Films*, vol. 442, no. 1–2, pp. 201–211, 2003.

[18] D. K. Benson and H. M. Branz, "Design goals and challenges for a photovoltaic-powered electrochromic window covering," *Sol. Energy Mater. Sol. Cells*, vol. 39, no. 2–4, pp. 203–211, 1995.

[19] J. Jensen, H. F. Dam, J. R. Reynolds, A. L. Dyer, and F. C. Krebs, "Manufacture and demonstration of organic photovoltaic-powered electrochromic displays using roll coating methods and printable electrolytes," *J. Polym. Sci. Part B Polym. Phys.*, vol. 50, no. 8, pp. 536–545, 2012.

[20] A. L. Dyer, R. H. Bulloch, Y. Zhou, B. Kippelen, J. R. Reynolds, and F. Zhang, "A Vertically Integrated Solar-Powered Electrochromic Window for Energy Efficient Buildings," *Adv. Mater.*, vol. 26, no. 28, pp. 4895–4900, 2014.

[21] C.-H. H. Yeh, F.-Y. Y. Chang, H.-T. T. Young, T.-Y. Y. Hsieh, and C.-H. H. Chang, "Transparent Solar Concentrator for Flat Panel Display," *Jpn.*

J. Appl. Phys., vol. 51, no. 6S, p. 5, 2012.

[22] E. D. Cole, "Reflective concentrating solar cell assembly," 6,008,449 A, 1999.

[23] J. P. Morgan, "Solar panel window," 20090255568, 2009.

[24] H. Davidsson, B. Perers, and B. Karlsson, "System analysis of a multifunctional PV/T hybrid solar window," *Sol. Energy*, vol. 86, no. 3, pp. 903–910, 2012.

[25] S. Pelland, J. Remund, J. Kleissl, T. Oozeki, and K. De Brabandere, "Photovoltaic and Solar Forecasting: State of the Art," 2013.

[26] J. Remund and S. C. Müller, "Solar Radiation and Uncertainty Information of Meteonorm 7," in *Pvsec 2011*, 2011, no. November 2011, pp. 2–4.

[27] "Meteonorm," 2014. [Online]. Available: meteonorm.com.

[28] Paladino and Company, "Performance Assessment of SageGlass Electrochromic Coatings and Control Scenarios," 2010.

[29] J. E. Kaufman, *IES Lighting Handbook*. New York, N.Y: Illuminating Engineering Society of North America, 1981.

[30] A. Trabelsi, "Internal quantum efficiency improvement of polysilicon solar cells with porous silicon emitter," *Renew. Energy*, vol. 50, pp. 441–448, 2013.

[31] T. Tsutsui, M. Yahiro, H. Yokogawa, K. Kawano, and M. Yokoyama, "Doubling coupling-out efficiency in organic light-emitting devices using a thin silica aerogel layer," *Adv. Mater.*, vol. 13, no. 15, pp. 1149–1152, 2001.

[32] E. Bardy, J. Mollendorf, and D. Pendergast, "Thermal conductivity and compressive strain of foam neoprene insulation under hydrostatic pressure," *J. Phys. D. Appl. Phys.*, vol. 38, no. 20, pp. 3832–3840, 2005.

[33] M. Rubin, "Optical Properties of Soda Lime Silica Glasses," *Sol. Energy Mater.*, vol. 12, pp. 275–288, 1985.

[34] "SCHOTT Glass." [Online]. Available: www.schott.com. [Accessed: 15-

Jan-2016].

[35] "Knight Optical." [Online]. Available: www.knightoptical.com.

[36] N. Kooy, K. Mohamed, L. Pin, and O. Guan, "A review of roll-to-roll nanoimprint lithography," *Nanoscale Res. Lett.*, vol. 9, no. 1, p. 320, 2014.

[37] H. Tan, A. Gilbertson, S. Y. Chou, B. Faircloth, H. Rohrs, R. Tiberio, R. Ruoff, and R. R. Krchnavek, "Roller nanoimprint lithography," *J. Vac. Sci. Technol. B Microelectron. Nanom. Struct.*, vol. 16, no. 4, p. 3926, 1998.

[38] J. John, Y. Tang, J. P. Rothstein, J. J. Watkins, and K. R. Carter, "Large-area, continuous roll-to-roll nanoimprinting with PFPE composite molds.," *Nanotechnology*, vol. 24, no. 50, p. 505307, 2013.

[39] P. Dannberg, L. Erdmann, R. Bierbaum, A. Krehl, A. Brauer, and E. B. Kley, "Micro-optical elements and their integration to glass and optoelectronic wafers," *Microsyst. Technol.*, vol. 6, no. 2, pp. 41–47, 1999.

[40] U. Schulz and N. Kaiser, "Vacuum coating of plastic optics," *Prog. Surf. Sci.*, vol. 81, no. 8–9, pp. 387–401, 2006.

[41] Y. M. Lu, W. S. Hwang, W. Y. Liu, and J. S. Yang, "Effect of RF power on optical and electrical properties of ZnO thin film by magnetron sputtering," *Mater. Chem. Phys.*, vol. 72, no. 2, pp. 269–272, 2001.

[42] J. Kalowekamo and E. Baker, "Estimating the manufacturing cost of purely organic solar cells," *Sol. Energy*, vol. 83, no. 8, pp. 1224–1231, 2009.

[43] A. L. Roes, E. A. Alsema, K. Blok, and M. K. Patel, "Ex-ante environmental and economic evaluation of polymer photovoltaics," *Prog. Photovoltaics Res. Appl.*, vol. 20, no. 1, pp. 6–11, 2012.

[44] F. He and L. Yu, "How far can polymer solar cells go? in need of a synergistic approach," *J. Phys. Chem. Lett.*, vol. 2, pp. 3102–3113, 2011.

[45] P. Peumans, A. Yakimov, and S. R. Forrest, "Small molecular weight organic thin-film photodetectors and solar cells," *J. Appl. Phys.*, vol. 104, no. 7, p. 3693, 2003.

[46] M. Born and E. Wolf, *Principles of Optics: Electromagnetic Theory of Propagation, Interference and Diffraction of Light*. Cambridge University Press, 1999.

[47] Y. Liang, Z. Xu, J. Xia, S. T. Tsai, Y. Wu, G. Li, C. Ray, and L. Yu, "For the bright future-bulk heterojunction polymer solar cells with power conversion efficiency of 7.4%," *Adv. Mater.*, vol. 22, no. 20, pp. 135–138, 2010.

[48] P. Kumar and S. Chand, "Recent progress and future aspects of organic solar cells," *Prog. Photovoltaics Res. Appl.*, vol. 20, no. 4, pp. 377–415, 2012.

[49] M. A. Green, K. Emery, Y. Hishikawa, W. Warta, and E. D. Dunlop, "Solar cell efficiency tables (version 46)," *Prog. Photovoltaics Res. Appl.*, vol. 23, pp. 805–812, 2015.

[50] C. J. Brabec, S. Gowrisanker, J. J. M. Halls, D. Laird, S. Jia, and S. P. Williams, "Polymer-Fullerene Bulk-Heterojunction Solar Cells," *Adv. Mater.*, vol. 22, no. 34, pp. 3839–3856, 2010.

[51] S. Shahin, P. Gangopadhyay, and R. A. Norwood, "Ultrathin organic bulk heterojunction solar cells: Plasmon enhanced performance using Au nanoparticles," *Appl. Phys. Lett.*, vol. 101, no. 5, p. 053109, 2012.

[52] A. J. Moulé, J. B. Bonekamp, and K. Meerholz, "The effect of active layer thickness and composition on the performance of bulk-heterojunction solar cells," *J. Appl. Phys.*, vol. 100, no. 9, p. 094503, 2006.

[53] S. I. Na, S. S. Kim, S. S. Kwon, J. Jo, J. Kim, T. Lee, and D. Y. Kim, "Surface relief gratings on poly(3-hexylthiophene) and fullerene blends for efficient organic solar cells," *Appl. Phys. Lett.*, vol. 91, no. 2007, pp. 1–3, 2007.

[54] P. Campbell and M. a. Green, "Light trapping properties of pyramidally textured surfaces," *J. Appl. Phys.*, vol. 62, no. 1, pp. 243–249, 1987.

[55] L. S. Roman, O. Inganäs, T. Granlund, T. Nyberg, M. Svensson, M. R. Andersson, and J. C. Hummelen, "Trapping light in polymer photodiodes

with soft embossed gratings," *Adv. Mater.*, vol. 12, pp. 189–195, 2000.

[56] F. Llopis and I. Tobías, "The role of rear surface in thin silicon solar cells," *Sol. Energy Mater. Sol. Cells*, vol. 87, no. 1–4, pp. 481–492, 2005.

[57] M. Niggemann, M. Glatthaar, a. Gombert, a. Hinsch, and V. Wittwer, "Diffraction gratings and buried nano-electrodes - Architectures for organic solar cells," *Thin Solid Films*, vol. 451–452, pp. 619–623, 2004.

[58] F. Monestier, J.-J. Simon, P. Torchio, L. Escoubas, F. Flory, S. Bailly, R. de Bettignies, S. Guillerez, and C. Defranoux, "Modeling the short-circuit current density of polymer solar cells based on P3HT:PCBM blend," *Sol. Energy Mater. Sol. Cells*, vol. 91, no. 5, pp. 405–410, 2007.

[59] E. D. Palik, *Handbook of Optical Constants of Solids*, vol. 1. Academic Press, 1985.

[60] J. S. K. Rajkanan, R. Singh, "Absorption-Coefficient of Silicon for Solar-Cell Calculations," *Solid. State. Electron.*, vol. 22, no. 9, pp. 793–795, 1979.

[61] Z. Yu, A. Raman, and S. Fan, "Fundamental limit of nanophotonic light trapping in solar cells," *Proc. Natl. Acad. Sci.*, vol. 107, no. 41, pp. 17491–17496, 2010.

[62] E. G. Loewen and E. Popov, *Diffraction Gratings and Applications*, 0 ed. CRC Press, 1997.

[63] E. Yablonovitch, "Statistical ray optics," *J. Opt. Soc. Am.*, vol. 72, no. 7, pp. 899–907, Jul. 1982.

[64] J. M. Bendickson, E. N. Glytsis, and T. K. Gaylord, "Scalar integral diffraction methods: unification, accuracy, and comparison with a rigorous boundary element method with application to diffractive cylindrical lenses," *J. Opt. Soc. Am. A*, vol. 15, no. 7, p. 1822, 1998.

[65] J. R. Tumbleston, D. H. Ko, E. T. Samulski, and R. Lopez, "Electrophotonic enhancement of bulk heterojunction organic solar cells through photonic crystal photoactive layer," *Appl. Phys. Lett.*, vol. 94, no. 4, pp. 18–20, 2009.

[66] J. M. Palmer and B. G. Grant, *The Art of Radiometry*, vol. PM184. 2009.

[67] J. Hodgkinson, D. Masiyano, and R. P. Tatam, "Using integrating spheres as absorption cells: path-length distribution and application of Beer's law," *Appl. Opt.*, vol. 48, no. 30, pp. 5748–5758, 2009.

[68] A. Lopez-Santiago, H. R. Grant, P. Gangopadhyay, R. Voorakaranam, R. A. Norwood, and N. Peyghambarian, "Cobalt ferrite nanoparticles polymer composites based all-optical magnetometer," *Opt. Mater. Express*, vol. 2, no. 7, p. 978, 2012.

[69] J. Thomas, P. Gangopadhyay, E. Araci, R. A. Norwood, and N. Peyghambarian, "Nanoimprinting by melt processing: An easy technique to fabricate versatile nanostructures," *Adv. Mater.*, vol. 23, pp. 4782–4787, 2011.

[70] V. Shrotriya, G. Li, Y. Yao, T. Moriarty, K. Emery, and Y. Yang, "Accurate Measurement and Characterization of Organic Solar Cells," *Adv. Funct. Mater.*, vol. 16, no. 15, pp. 2016–2023, 2006.

[71] K. Emery and T. Moriarty, "Accurate measurement of organic solar cell efficiency," *Spie*, vol. 7052, no. 1, p. 70520D–70520D–6, 2008.

[72] G. Li, V. Shrotriya, J. Huang, and Y. Yang, "Measurement issues of organic solar cell," *Proc. SPIE - Int. Soc. Opt. Eng.*, vol. 7052, p. 70520E–70520E–9, 2008.

[73] R. Y. Zhang, B. Shao, J. R. Dong, J. C. Zhang, and H. Yang, "Absorption enhancement analysis of crystalline Si thin film solar cells based on broadband antireflection nanocone grating," *J. Appl. Phys.*, vol. 110, no. 11, 2011.

[74] S. H. Zaidi, J. M. Gee, and D. S. Ruby, "Diffraction grating structures in solar cells," *Conf. Rec. IEEE Photovolt. Spec. Conf.*, vol. 2000-Janua, pp. 395–398, 2000.

[75] T. K. Gaylord, W. E. Baird, and M. G. Moharam, "Zero-reflectivity high spatial-frequency rectangular-groove dielectric surface-relief gratings," *Appl. Opt.*, vol. 25, no. 24, pp. 4562–4567, 1986.

[76] P. Spessotto, E. Giacomello, and R. Perri, "Improving fluorescence-based assays for the in vitro analysis of cell adhesion and migration," *Mol. Biotechnol.*, vol. 20, no. 3, pp. 285–304, Mar. 2002.

[77] S. Deshayes and G. Divita, "Fluorescence Technologies for Monitoring Interactions Between Biological Molecules In Vitro," in *Fluorescence-based biosensors: from concepts to applications*, vol. 113, M. Morris, Ed. Elsevier Inc., 2013, pp. 109–143.

[78] K. Aoki, Y. Kamioka, and M. Matsuda, "Fluorescence resonance energy transfer imaging of cell signaling from in vitro to in vivo: basis of biosensor construction, live imaging, and image processing," *Dev. Growth Differ.*, vol. 55, no. 4, pp. 515–22, May 2013.

[79] E. Sierecki and N. Giles, "A cell-free approach to accelerate the study of protein–protein interactions in vitro," *Interface …*, vol. 3, no. August, p. 20130018, Oct. 2013.

[80] R. Hoffman, "Green fluorescent protein imaging of tumour growth, metastasis, and angiogenesis in mouse models," *Lancet Oncol.*, vol. 3, no. 9, pp. 546–556, Sep. 2002.

[81] M. Fritzsche and C. F. Mandenius, "Fluorescent cell-based sensing approaches for toxicity testing," *Anal. Bioanal. Chem.*, vol. 398, no. 1, pp. 181–191, Sep. 2010.

[82] M. Hassan and B. a Klaunberg, "Biomedical applications of fluorescence imaging in vivo," *Comp. Med.*, vol. 54, no. 6, pp. 635–644, 2004.

[83] U. Kubitscheck, *Fluorescence Microscopy: From Principles to Biological Applications*. John Wiley & Sons, 2013.

[84] K. M. Dean and A. E. Palmer, "Advances in fluorescence labeling strategies for dynamic cellular imaging," *Nat. Chem. Biol.*, vol. 10, no. 7, pp. 512–523, Jul. 2014.

[85] F. Helmchen and W. Denk, "Deep tissue two-photon microscopy," *Nat. Methods*, vol. 2, no. 12, pp. 932–940, Dec. 2005.

[86] K. Licha, "Contrast Agents for Optical Imaging," in *Top.Curr.Chem.*, vol.

222, W. Krause, Ed. 2002, pp. 1–29.

[87] Lord Rayleigh, "XXXIV. On the transmission of light through an atmosphere containing small particles in suspension, and on the origin of the blue of the sky," *Philos. Mag. Ser. 5*, vol. 47, no. 287, pp. 375–384, 1899.

[88] D. M. Shotton, "Confocal scanning optical microscopy and its applications for biological specimens," *J. Cell Sci.*, vol. 94, no. 2, pp. 175–206, Oct. 1989.

[89] B. R. Pawley, JB and Masters, *Handbook of Biological Confocal Microscopy*, vol. 35, no. 9. New York, NY: Springer, 1996.

[90] a Periasamy, P. Skoglund, C. Noakes, and R. Keller, "An evaluation of two-photon excitation versus confocal and digital deconvolution fluorescence microscopy imaging in Xenopus morphogenesis.," *Microsc. Res. Tech.*, vol. 47, no. 3, pp. 172–81, Nov. 1999.

[91] B. J. Tromberg, N. Shah, R. Lanning, A. Cerussi, J. Espinoza, T. Pham, L. Svaasand, and J. Butler, "Non-invasive in iivo characterization of breast tumors using photon migration spectroscopy," *Neoplasia*, vol. 2, no. 1–2, pp. 26–40, 2000.

[92] D. Grosenick, H. Wabnitz, H. H. Rinneberg, K. T. Moesta, and P. M. Schlag, "Development of a time-domain optical mammograph and first in vivo applications," *Appl. Opt.*, vol. 38, no. 13, pp. 2927–43, May 1999.

[93] R. K. P. Benninger and D. W. Piston, "Two-Photon Excitation Microscopy for the Study of Living Cells and Tissues," in *Current Protocols in Cell Biology*, John Wiley & Sons, Inc., 2013.

[94] F. Bestvater, E. Spiess, G. Stobrawa, M. Hacker, T. Feurer, T. Porwol, U. Berchner-Pfannschmidt, C. Wotzlaw, and H. Acker, "Two-photon fluorescence absorption and emission spectra of dyes relevant for cell imaging," *J. Microsc.*, vol. 208, no. 2, pp. 108–115, 2002.

[95] M. Drobizhev, N. S. Makarov, S. E. Tillo, T. E. Hughes, and A. Rebane, "Two-photon absorption properties of fluorescent proteins," *Nat.*

Methods, vol. 8, no. 5, pp. 393–399, May 2011.

[96] L. Novotny and B. Hecht, *Principles of Nano-Optics*. Cambridge University Press, 2006.

[97] D. Sarid and W. Challener, *Modern Introduction to Surface Plasmons*. Cambridge University Press, 2010.

[98] Y. Fang, K. Blinn, X. Li, G. Weng, and M. Liu, "Strong coupling between Rhodamine 6G and localized surface plasmon resonance of immobile Ag nanoclusters fabricated by direct current sputtering," *Appl. Phys. Lett.*, vol. 102, no. 14, pp. 143112–143112–4, 2013.

[99] Y. K. Xu, S. Hwang, S. Kim, and J. Y. Chen, "Two orders of magnitude fluorescence enhancement of aluminum phthalocyanines by gold nanocubes: A remarkable improvement for cancer cell imaging and detection," *ACS Appl. Mater. Interfaces*, vol. 6, no. 8, pp. 5619–5628, Apr. 2014.

[100] C. D. Geddes, H. Cao, I. Gryczynski, Z. Gryczynski, J. Fang, and J. R. Lakowicz, "Metal-enhanced fluorescence (MEF) due to silver colloids on a planar surface: Potential applications of indocyanine green to in vivo imaging," *J. Phys. Chem. A*, vol. 107, no. 18, pp. 3443–3449, May 2003.

[101] S. Kim, Y. Xuan, V. P. Drachev, L. T. Varghese, L. Fan, M. Qi, and K. J. Webb, "Nanoimprinted plasmonic nanocavity arrays," *Opt. Express*, vol. 21, no. 13, p. 15081, Jul. 2013.

[102] H. R. Stuart and D. G. Hall, "Island size effects in nanoparticle-enhanced photodetectors," *Appl. Phys. Lett.*, vol. 73, no. 26, pp. 3815–3817, Dec. 1998.

[103] J. Ye, M. Shioi, K. Lodewijks, L. Lagae, T. Kawamura, and P. Van Dorpe, "Tuning plasmonic interaction between gold nanorings and a gold film for surface enhanced Raman scattering," *Appl. Phys. Lett.*, vol. 97, no. 16, pp. 22–25, Oct. 2010.

[104] J. a. Scholl, A. L. Koh, and J. a. Dionne, "Quantum plasmon resonances of individual metallic nanoparticles," *Nature*, vol. 483, no. 7390, pp. 421–

427, Mar. 2012.

[105] A. Wirgin and T. López-Ríos, "Can surface-enhanced Raman scattering be caused by waveguide resonances?," *Opt. Commun.*, vol. 48, no. 6, pp. 416–420, 1984.

[106] P. Genevet, J.-P. Tetienne, E. Gatzogiannis, R. Blanchard, M. A. Kats, M. O. Scully, and F. Capasso, "Large enhancement of nonlinear optical phenomena by plasmonic nanocavity gratings," *Nano Lett.*, vol. 10, no. 12, pp. 4880–4883, Dec. 2010.

[107] J. H. Vella and A. M. Urbas, "Nanoplasmonic array enhancement of two-photon absorption in a dye film," *J. Phys. Chem. C*, vol. 116, no. 32, pp. 17169–17173, Aug. 2012.

[108] a. M. Glass, A. Wokaun, J. P. Heritage, J. G. Bergman, P. F. Liao, and D. H. Olson, "Enhanced two-photon fluorescence of molecules adsorbed on silver particle films," *Phys. Rev. B*, vol. 24, no. 8, pp. 4906–4909, 1981.

[109] W. Wenseleers, F. Stellacci, T. Meyer-Friedrichsen, T. Mangel, C. A. Bauer, S. J. K. Pond, S. R. Marder, and J. W. Perry, "Five orders-of-magnitude enhancement of two-photon absorption for dyes on silver nanoparticle fractal clusters," *J. Phys. Chem. B*, vol. 106, no. 27, pp. 6853–6863, Jul. 2002.

[110] W. R. Zipfel, R. M. Williams, and W. W. Webb, "Nonlinear magic: multiphoton microscopy in the biosciences," *Nat. Biotechnol.*, vol. 21, no. 11, pp. 1369–1377, Nov. 2003.

[111] E. K. Bomati, G. Manning, and D. D. Deheyn, "Amphioxus encodes the largest known family of green fluorescent proteins, which have diversified into distinct functional classes," *BMC Evol. Biol.*, vol. 9, no. 1, p. 77, Apr. 2009.

[112] K. Kieu, S. Mehravar, R. Gowda, R. A. Norwood, and N. Peyghambarian, "Label-free multi-photon imaging using a compact femtosecond fiber laser mode-locked by carbon nanotube saturable absorber," *Biomed. Opt. Express*, vol. 4, no. 10, pp. 2187–95, Oct. 2013.

[113] A. Säynätjoki, L. Karvonen, J. Riikonen, W. Kim, S. Mehravar, R. A. Norwood, N. Peyghambarian, H. Lipsanen, and K. Kieu, "Rapid large-area multiphoton microscopy for characterization of graphene," *ACS Nano*, vol. 7, no. 10, pp. 8441–8446, Oct. 2013.

[114] R. Himmelhuber, K. Kieu, O. D. Herrera, R. A. Norwood, and N. Peyghambarian, "Characterization of coplanar poled electro optic polymer films for Si-photonic devices with multiphoton microscopy," *2013 Opt. Interconnects Conf. OI 2013*, vol. 161109, no. 16, pp. 90–91, Apr. 2013.

[115] T. Alasaarela, L. Karvonen, H. Jussila, A. Säynätjoki, S. Mehravar, R. A. Norwood, N. Peyghambarian, K. Kieu, I. Tittonen, and H. Lipsanen, "High-quality crystallinity controlled ALD TiO2 for waveguiding applications.," *Opt. Lett.*, vol. 38, no. 20, pp. 3980–3, Oct. 2013.

[116] A. Chakrabarty, F. Wang, F. Minkowski, K. Sun, and Q.-H. Wei, "Cavity modes and their excitations in elliptical plasmonic patch nanoantennas.," *Opt. Express*, vol. 20, no. 11, pp. 11615–24, May 2012.

[117] A. Dhawan, M. Canva, and T. Vo-Dinh, "Narrow groove plasmonic nano-gratings for surface plasmon resonance sensing.," *Opt. Express*, vol. 19, no. 2, pp. 787–813, Jan. 2011.

[118] I. Polyzos, G. Tsigaridas, M. Fakis, V. Giannetas, P. Persephonis, and J. Mikroyannidis, "Substituent effect on the photobleaching of pyrylium salts under ultrashort pulsed illumination.," *J. Phys. Chem. B*, vol. 110, no. 6, pp. 2593–7, Feb. 2006.

[119] R. Bakalova and Z. Zhelev, "Designing quantum-dot probes," *Group*, vol. 1, no. September, pp. 2006–2008, Sep. 2007.